Mon. Not. R. Astron. Soc. **000**, 000–000 (0000) Printed 20 February 2014 (MN LATEX style file v2.2)

PACS photometry of the *Herschel* Reference Survey – Far-infrared/sub-millimeter colours as tracers of dust properties in nearby galaxies⋆

arXiv:1402.4524v1 [astro-ph.GA] 18 Feb 2014

L. Cortese†[1,2], J. Fritz[3], S. Bianchi[4], A. Boselli[5], L. Ciesla[6], G. J. Bendo[7], M. Boquien[5,8], H. Roussel[9], M. Baes[3], V. Buat[5], M. Clemens[10], A. Cooray[11], D. Cormier[12], J. I. Davies[13], I. De Looze[3], S. A. Eales[13], C. Fuller[13], L. K. Hunt[4], S. Madden[14], J. Munoz-Mateos[15], C. Pappalardo[4], D. Pierini[16], A. Rémy-Ruyer[14], M. Sauvage[14], S. di Serego Alighieri[4], M. W. L. Smith[13], L. Spinoglio[17], M. Vaccari[18], C. Vlahakis[19]

[1] *Centre for Astrophysics & Supercomputing, Swinburne University of Technology, Mail H30 - PO Box 218, Hawthorn, VIC 3122, Australia*
[2] *European Southern Observatory, Karl-Schwarzschild Str. 2, 85748 Garching bei Muenchen, Germany*
[3] *Sterrenkundig Observatorium, Universiteit Gent, Krijgslaan 281 S9, 9000, Gent, Belgium*
[4] *INAF-Osservatorio Astrofisico di Arcetri, Largo Enrico Fermi 5, 50125 Firenze, Italy*
[5] *Laboratoire d'Astrophysique de Marseille - LAM, Université d'Aix-Marseille & CNRS, UMR7326, 38 rue F. Joliot-Curie, F-13388 Marseiulle Cedex 13, France*
[6] *University of Crete, Department of Physics, Heraklion, Crete, 71003, Greece*
[7] *UK ALMA Regional Centre Node, Jodrell Bank Centre for Astrophysics, School of Physics and Astronomy, University of Manchester, Oxford Road, Manchester M13 9PL, United Kingdom*
[8] *Institute of Astronomy, University of Cambridge, Madingley Road, Cambridge CB30HA, UK*
[9] *Institut d'Astrophysique de Paris, Université Pierre et Marie Curie (UPMC), CNRS (UMR7095), 75014 Paris, France*
[10] *Osservatorio Astronomico di Padova, Vicolo dell'Osservatorio 5, I-35122 Padova, Italy*
[11] *University of California, Irvine, Department of Physics & Astronomy, 4186 Frederick Reines Hall, Irvine, CA, USA*
[12] *Institut für Theoretische Astrophysik, Zentrum für Astronomie der Universität Heidelberg, Albert-Ueberle Str. 2, D-69120 Heidelberg, Germany*
[13] *School of Physics and Astronomy, Cardiff University, The Parade, Cardiff, CF24 3AA, UK*
[14] *Laboratoire AIM, CEA, Université Paris VII, IRFU/Service d'Astrophysique, Bat. 709, 91191 Gif-sur-Yvette, France*
[15] *European Southern Observatory, Alonso de Cordova 3107, Vitacura, Casilla 19001, Santiago de Chile*
[16] *Max-Planck-Institut für extraterrestrische Physik, Giessenbachstrasse, Postfach 1312, D-85741, Garching bei München, Germany*
[17] *Istituto di Fisica dello Spazio Interplanetario, INAF, Via Fosso del Cavaliere 100, I-00133 Roma, Italy*
[18] *Astrophysics Group, Physics Department, University of the Western Cape, Private Bag X17, Bellville 7535, Cape Town, South Africa*
[19] *Joint ALMA Observatory/European Southern Observatory, Alonso de Cordova 3107, Vitacura, Santiago, Chile*

Accepted 2014 January 21. Received 2014 January 20; in original form 2013 November 3

ABSTRACT

We present *Herschel*/PACS 100 and 160 μm integrated photometry for the 323 galaxies in the *Herschel* Reference Survey (HRS), a K-band-, volume-limited sample of galaxies in the local Universe. Once combined with the *Herschel*/SPIRE observations already available, these data make the HRS the largest representative sample of nearby galaxies with homogeneous coverage across the 100-500 μm wavelength range. In this paper, we take advantage of this unique dataset to investigate the properties and shape of the far-infrared/sub-millimeter spectral energy distribution in nearby galaxies. We show that, in the stellar mass range covered by the HRS ($8 \lesssim \log(M_*/M_\odot) \lesssim 12$), the far-infrared/sub-millimeter colours are inconsistent with a single modified black-body having the same dust emissivity index β for all galaxies. In particular, either β decreases, or multiple temperature components are needed, when moving from metal-rich/gas-poor to metal-poor/gas-rich galaxies. We thus investigate how the dust temperature and mass obtained from a single modified black-body depend on the assumptions made on β. We show that, while the correlations between dust temperature, galaxy structure and star formation rate are strongly model dependent, the dust mass scaling relations are much more reliable, and variations of β only change the strength of the observed trends.

© 0000 RAS

Key words: galaxies: fundamental parameters – galaxies: ISM – infrared: galaxies

1 INTRODUCTION

It is now well established that approximately half of the radiative energy produced by galaxies is absorbed by dust grains and re-emitted in the infrared regime (Hauser & Dwek 2001; Boselli et al. 2003; Dole et al. 2006; Dale et al. 2007; Burgarella et al. 2013). Thus, observations in the ∼10-1000 μm wavelength range provide us with a unique opportunity not only to quantify half of the bolometric luminosity of galaxies, but also to characterise the properties of cosmic dust. Moreover, since dust grains are crucial for the star formation cycle (Hollenbach & Salpeter 1971), such information can give us important insights into the physical processes regulating galaxy evolution (e.g., Dunne et al. 2011).

Unfortunately, despite its paramount importance, we are still missing a complete and coherent picture of dust properties in galaxies across the Hubble sequence, and of the exact role played by grains in regulating star formation (McKee & Krumholz 2010). Indeed, we know very little about the dust composition in galaxies outside our own Local Group (Draine & Li 2007; Compiègne et al. 2011) and if/how it is regulated by the physical conditions experienced by grains in the inter-stellar medium (ISM). Hence, our estimates of dust masses in galaxies are still highly uncertain (Finkbeiner et al. 1999; Dupac et al. 2003; Gordon et al. 2010; Paradis et al. 2010; Planck Collaboration et al. 2011b).

Luckily, the last decade has seen the start of a golden age for observational far-infrared (FIR) and sub-millimeter (submm) astronomy, providing a new boost to the refinement of theoretical dust models (Meny et al. 2007; Draine & Li 2007; Hoang et al. 2010; Compiègne et al. 2011; Steinacker et al. 2013). In particular, the *Spitzer* (Werner et al. 2004), and more recently *Herschel* (Pilbratt et al. 2010) and *Planck* (Planck Collaboration et al. 2011a) space telescopes are finally gathering a wealth of information on the dust emission from thousands of galaxies up to z ∼2. Particularly important for a proper characterisation of dust in galaxies is the radiation emitted at wavelengths ≳100-200 μm. In this regime, the integrated emission from galaxies originates predominantly from dust in thermal equilibrium, heated by the diffuse interstellar radiation field (ISRF), which represents the bulk of the dust mass in a galaxy (e.g., Sodroski et al. 1989; Sauvage & Thuan 1992; Calzetti et al. 1995; Walterbos & Greenawalt 1996; Bendo et al. 2010; Boquien et al. 2011; Bendo et al. 2012). Thus, by characterising the dust emission in the ≳100 μm wavelength domain, we have a unique opportunity to provide strong constraints to theoretical models, and to refine our census of the dust budget in galaxies.

The first natural step in this direction is to quantify how the shape of the dust spectral energy distribution (SED) varies with galaxy properties across a wide range of morphological type, star formation activity, cold gas mass and metal content. This is necessary to determine if the amount of radiation emitted at each wavelength is simply regulated by the intensity of the ISRF responsible for the dust heating, or whether it retains an imprint of the chemical composition of the grains. Indeed, only after a careful characterisation of the physical parameters regulating the dust SED, will it be possible to properly convert observables into physical quantities such as dust temperatures and dust masses.

Many recent works (Gordon et al. 2010; Skibba et al. 2011; Davies et al. 2012; Planck Collaboration et al. 2011b; Galametz et al. 2012; Auld et al. 2013) have shown that, above ∼100 μm, the dust SED is very well approximated by a simple modified black-body (but see also Bendo et al. 2012):

$$F_\nu = \frac{M_{dust}}{D^2}\kappa_{\nu_0}\left(\frac{\nu}{\nu_0}\right)^\beta B_\nu(T) \quad (1)$$

where F_ν is the flux density emitted at the frequency ν, κ_{ν_0} is the dust mass absorption coefficient at the frequency ν_0, β gives its variation as a function of frequency, D is the galaxy distance and $B_\nu(T)$ is the Planck function. Mounting evidence is emerging that β is not the same in all galaxies (e.g., Rémy-Ruyer et al. 2013), and may also vary within galaxies (e.g., Galametz et al. 2012; Smith et al. 2012).

Modified black-bodies are simple models and cannot properly reproduce real dust properties (e.g., Draine & Li 2007; Shetty et al. 2009; Bernard et al. 2010). Several dust components at various temperatures contribute to the total emission along the lines-of-sight. This implies the presence of temperature mixing that can cause variations of the infrared slope, and thus in the apparent emissivity index β. Nevertheless, parameterization of the dust SEDs through modified black-body fitting is a powerful tool to help understand variations of dust properties with other galaxy characteristics, especially in case of sparse sampling of the FIR/sub-mm wavelength range (e.g., high-redshift galaxies Magdis et al. 2011; Symeonidis et al. 2013). Therefore, it is extremely important to determine in which cases a single modified back-body can be used, and how temperature and dust mass estimates are affected by the assumptions made on β.

In order to ascertain the dust properties of galaxies in the local Universe, and to provide new constraints to theoretical models, we have carried out the *Herschel* Reference Survey (HRS, Boselli et al. 2010b), a *Herschel* guaranteed time project focused on the study of the interplay between dust, gas and star formation in a statistically significant sample of ∼300 galaxies spanning a wide range of morphologies, stellar masses (8≲log($M_*/M_\odot$)≲12), cold gas contents (-3≲log(M_{HI}/M_*)≲1), metallicities (8.2≲12+log(O/H) ≲8.9), and specific star formation rates (-12 ≲log(SFR/M_*)≲-9). The combination of *Herschel*/SPIRE (Griffin et al. 2010) observations with the multi-wavelength dataset we have been assembling (Ciesla et al. 2012; Cortese et al. 2012a;

⋆ *Herschel* is an ESA space observatory with science instruments provided by European-led Principal Investigator consortia and with important participation from NASA.

† lcortese@swin.edu.au

Boselli et al. 2013; Hughes et al. 2013), has already allowed us to have a first glimpse at how the dust content and shape of the dust SED vary with internal galaxy properties (Boselli et al. 2010a, 2012; Cortese et al. 2012b). In particular, Boselli et al. (2010a, 2012) have shown that the slope of the dust SED in the 200-500 μm interval decreases from $\beta \sim 2$ to $\beta \sim 1$ when moving from metal-rich to metal-poor galaxies. However, our analyses have so far been limited by the lack of data in the ∼100-200 μm wavelength range for the entire sample.

Thus, in this paper we present integrated *Herschel*/PACS (Poglitsch et al. 2010) 100 and 160 μm flux densities for all the HRS sample and take advantage of our multiwavelength dataset to perform a first analysis of the properties of the dust SED across our entire sample. Corresponding to the peak of the dust SED, the 100-200 μm wavelength interval is crucial not only to properly quantify the shape of the SED, but also to accurately determine the average dust temperature and total dust mass in galaxies. These data make the HRS the largest representative sample of nearby galaxies with homogeneous coverage across the ∼100-500 μm wavelength range. In addition to releasing our dataset to the community, our primary goals are 1) to investigate how the shape of the dust SED varies with internal galaxy properties, and 2) to determine whether the integrated dust SED of HRS galaxies can always be reduced to a single modified black-body with a constant value of β and, if not, what are the possible biases introduced by this assumption. The results of SED fitting with the dust models of Draine et al. (2007) will be presented in a forthcoming paper (Ciesla et al., submitted.).

This paper is organized as follows. In Sect. 2 we describe the *Herschel* observations, data reduction, flux density estimates and comparison with the literature. In Sect. 3 we use the PACS and SPIRE colours to investigate how the shape of the dust SED varies with internal galaxy properties. In Sec. 4, we show how the dust temperature and mass obtained from fitting a single modified black-body to the *Herschel* data depend on the assumptions made on β. Finally, the summary and implications of our results are presented in Sec. 5.

2 THE DATA

2.1 The *Herschel* Reference Survey

The HRS is a volume-limited sample (i.e., $15 \leq D \leq 25$ Mpc) including all late-type galaxies (261 Sa and later) with 2MASS (Skrutskie et al. 2006) K-band magnitude $K_{S,tot} \leq 12$ mag and all early-type galaxies (62 S0a and earlier) with $K_{S,tot} \leq 8.7$ mag[1]. Additional selection criteria are high galactic latitude ($b > +55°$) and low Galactic extinction ($A_B < 0.2$ mag, Schlegel et al. 1998), to minimize Galactic cirrus contamination. More details on the original selection can be found in Boselli et al. (2010b), while the most recent morphological classifications and distance estimates are presented in Cortese et al. (2012a).

[1] We note that one galaxy (HRS228) had a wrong redshift reported in NED, and is in reality a background galaxy. In this work, we have included it for completeness.

2.2 PACS observations and data reduction

The *Herschel*/PACS 100 and 160 μm observations of HRS galaxies presented in this work have been obtained as part of various open-time *Herschel* projects.

The vast majority of the data (228 out of 323 galaxies) comes from our own *Herschel* cycle 1 open time proposal (OT1_lcortese1). Each galaxy was observed in scan mode, along two perpendicular axes, at the medium scan speed of 20″/sec. Two repetitions were done in each scan direction. The size of each map was chosen to match the size of our SPIRE images (see Ciesla et al. 2012), making sure to have homogeneous coverage across the entire 100-500 μm range.

Maps for additional 83 HRS galaxies have been obtained as part of the *Herschel* Virgo Cluster Survey (HeViCS, Davies et al. 2010). HeViCS mapped the Virgo cluster with both PACS and SPIRE simultaneously at the fast scan speed of 60″/sec. The observing strategy consists of scanning each ∼4×4 deg^2 field in two orthogonal directions, and repeating each scan four times (Auld et al. 2013). The faster scan speed of the *Herschel* parallel mode with respect to the scan map mode, used for our observations, is compensated by the higher number of repetitions performed in the Virgo cluster, making the two datasets highly comparable (i.e., within ∼30%) in terms of their final noise.

PACS observations for the remaining 12 HRS galaxies have been retrieved from the *Herschel* public archive, and come from various projects (i.e., Kennicutt et al. 2011, KPGT_esturm_1, OT1_acrocker_1, OT2_emurph01_3, GT1_lspinogl_2, OT2_aalonsoh_2). All data have been obtained in scan mode at the medium scan speed of 20″/sec and they reach a noise level similar or lower than our own observations. For one galaxy (HRS3) only 160 μm observations are available as the object lies at the edge of the 100 μm map, making the data not suitable for accurate photometry. Thus, in summary, all 323 galaxies in the HRS have been observed at 160 μm, whereas 100 μm data are available for 322 objects.

All raw PACS data were processed from Level-0 to Level-1 within HIPE (v10.0.0, Ott 2010) using the calibration file v48. This pre-processing includes, among the other tasks, pixel flagging, flux density conversion and coordinate assignment. To remove the $1/f$ noise which, at this point, still dominates the timelines, the Level-1 data were fed into `Scanamorphos` (version 21, Roussel 2013), an IDL algorithm which performs an optimal correction by exploiting the redundancy in the observations of each sky pixel. No noise modelling is hence needed. The pixel size of the final maps was chosen to sample at the best the point-spread-function, at the respective wavelengths, typical of the data taken at medium scan speed: 1.7 and 2.85 arcsec pixel^{-1} at 100 and 160 μm, respectively (i.e., FWHM/4). The typical pixel-by-pixel noise in the map varies between ∼0.1 and ∼0.25 mJy pixel^{-1} at 160 μm and between ∼0.04 and ∼0.1 mJy pixel^{-1} at 100 μm.

In order to show the data quality of the new observations presented here, in Fig. 1 we compare the PACS images for three of our targets with the RGB Sloan Digital Sky Survey (Abazajian et al. 2009) optical and SPIRE 250 μm (Ciesla et al. 2012) images. We show an example of an early-type galaxy with dust lanes (HRS45, top row), late-

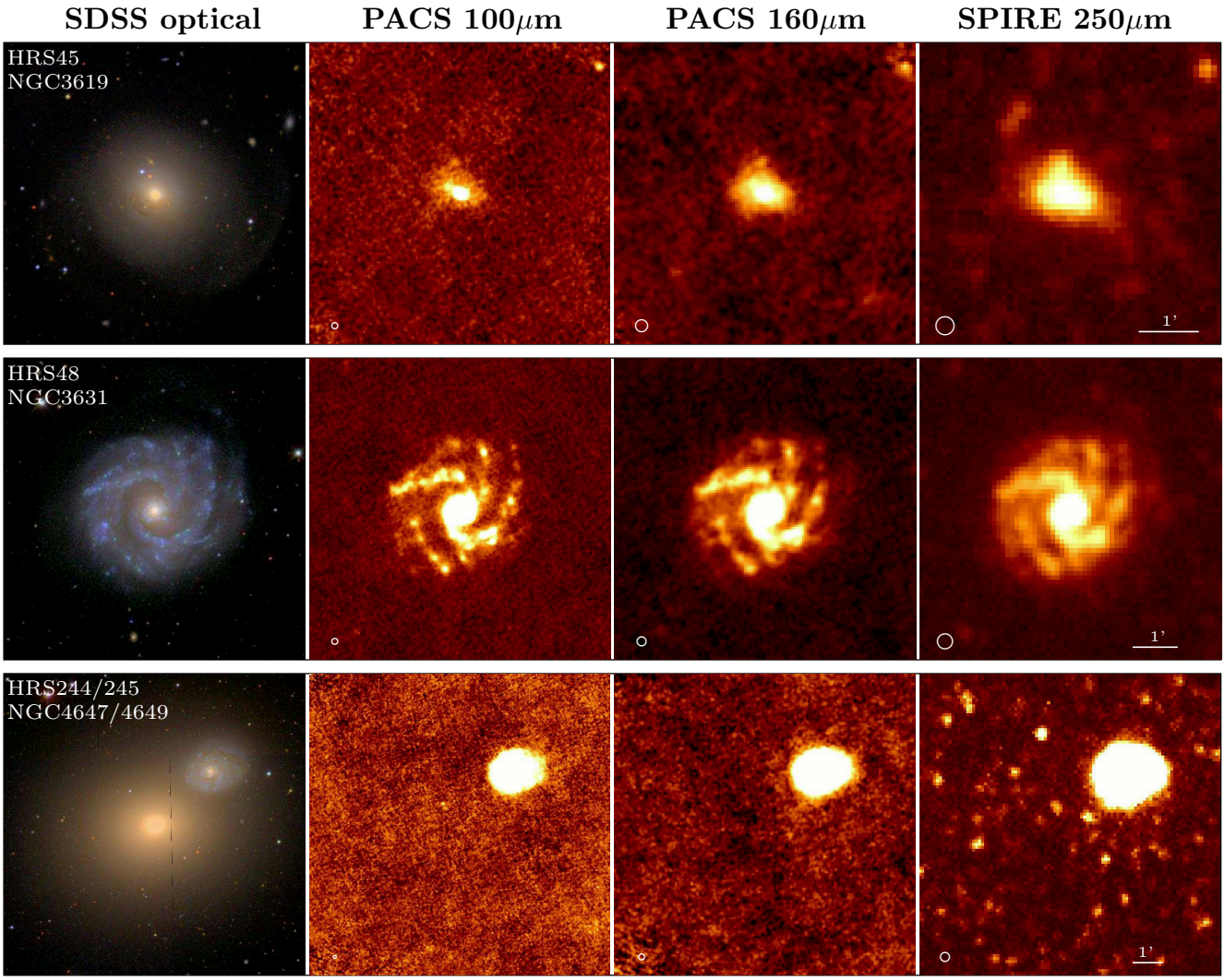

Figure 1. Comparison of the quality of our PACS images with the Sloan Digital Sky Survey optical and SPIRE 250 μm images. We show three types of objects: an early-type with dust lanes (top row), an unperturbed late-type spiral and an un-detected elliptical and its spiral companion. The size of the PACS and SPIRE beams is shown in the bottom left corner of each panel.

type galaxy (HRS48, middle row) and un-detected elliptical and its spiral companion (HRS244/245, bottom row).

2.3 PACS 100 and 160 μm integrated photometry

Integrated 100 and 160 μm photometry has been performed following very closely the technique used by Ciesla et al. (2012) for the SPIRE data of HRS galaxies. This is crucial to properly combine the two datasets, and to characterise the shape of the SED across the entire 100-500 μm wavelength range. Thus, whenever possible, we determined integrated flux densities within the same apertures adopted in Ciesla et al. (2012). The aperture sizes are adapted to include the entire extent of the FIR emission from the galaxies, and they correspond to $\sim$1.4, $\sim$0.7 and $\sim$0.3 times the optical diameter for late-type, lenticular and elliptical galaxies, respectively. Only for 36 galaxies ($\sim$11% of the sample) we choose different sizes than those used for SPIRE. There are three different reasons why we did so: a) For 23 galaxies (HRS6, 14, 22, 32, 67, 71, 75, 158, 209, 223, 225, 238, 243, 249, 255, 257, 261, 264, 286, 300, 315, 317, 322) the 100 and 160 μm emission is significantly less extended than the size of the aperture used by Ciesla et al. (2012). Although this does not affect the estimate of the integrated flux density, it artificially boosts the error associated with our measurements to values always above 50%, and sometimes even higher than 100%. Thus, for these objects, we reduced the size of the aperture (on average by $\sim$26%) to obtain more realistic error estimates. We note that the size chosen is still larger than the extent of the FIR emission (so that aperture corrections are not necessary), and that the flux density estimated within these new apertures is consistent with the value obtained using Ciesla et al. (2012) apertures. b) 10 galaxies (HRS7, 68, 129, 138, 161, 174, 210, 231, 258, 308) were not spatially resolved in the SPIRE bands, and SPIRE photometry was carried out directly on the time-line data. For these cases, which are generally resolved by PACS, we chose new apertures which include all the emission from the target. c) For 3 galaxies (HRS4, 122, 263), the PACS maps available from the archive were slightly smaller than our

SPIRE maps. While these maps are large enough to include the entire aperture used in Ciesla et al. (2012), no space is left to properly estimate the background. Thus, the aperture has been reduced in order to allow a more accurate background estimate, and still encompass all the emission from the galaxy.

Sky background was determined in fifteen to thirty regions, depending on the size of the target, around the chosen aperture. The use of various regions instead of just a circular annulus makes it easier to estimate the large scale variations in the background and to avoid background/foreground sources around the target. The mean sky value was then subtracted from each map before performing the flux density extraction. Since cirrus contamination is significantly less of an issue than in SPIRE images, we did not find necessary to perform a more complex modelling of the background. However, as discussed below, the effect of any residual large scale gradient is included in our error estimates.

Errors on integrated flux densities have been estimated following the guidelines described in Roussel (2013), which are consistent with what is done in Ciesla et al. (2012) for HRS SPIRE data. Briefly, there are three sources of errors that affect our measurements:

$$\sigma_{tot} = \sqrt{\sigma_{cal}^2 + \sigma_{instr}^2 + \sigma_{sky}^2} \quad (2)$$

where σ_{cal} is the flux calibration uncertainty (here assumed to be 5%; Balog et al. 2013), σ_{instr} is the instrumental noise which depends on the number of scans crossing a pixel, and is obtained by summing in quadrature the values on the error map within the chosen aperture, and σ_{sky} is the error on the sky measurement. As discussed in Roussel (2013), the sky uncertainty results from the combination of the uncorrelated error on the mean value of the sky (σ_{skypix} i.e., the pixel-to-pixel variation across the image), and the correlated noise due to long time-scale drift residuals responsible for the large scale structures present in the image background ($\sigma_{skymean}$ i.e., the standard deviation of the mean value of the sky measured in different apertures around the galaxy; see also Boselli et al. 2003; Gil de Paz & Madore 2005). In detail,

$$\sigma_{sky} = \sqrt{N_{ap}\sigma_{skypix}^2 + N_{ap}^2\sigma_{skymean}^2} \quad (3)$$

where N_{ap} is the number of pixels in the aperture used to integrate the galaxy flux density. As expected, for the vast majority of our objects the dominant source of error is the correlated uncertainty on the large-scale structure of the background. The average total uncertainties are $\sigma_{tot}\sim$16% and 12% at 100 and 160 μm, respectively.

Out of the 323 galaxies observed, 282 have been detected in both bands (284 at 160 μm only). This matches the HRS detection fraction in the SPIRE bands (i.e., 284 galaxies detected at 250 μm), allowing us to characterise the shape of the FIR/sub-mm SED across the entire 100-500 μm range for almost 300 galaxies. In case of non detections, upper limits have been estimated as $3\times\sigma_{tot}$, using the same apertures as in Ciesla et al. (2012).

The results of our photometry are presented in Table 1. The columns are as follows:

Columns 1-6: HRS (Boselli et al. 2010b), CGCG (Zwicky et al. 1961), VCC (Binggeli et al. 1985), UGC (Nilson 1973), NGC (Dreyer 1888) and IC (Dreyer 1895) names.

Columns 7-8: the J2000 right ascension and declination.

Column 9: Morphological type, taken from Cortese et al. (2012a): -2=dE/dS0, 0=E-E/S0, 1=S0, 2=S0a-S0/Sa, 3=Sa, 4=Sab, 5=Sb, 6=Sbc, 7=Sc, 8=Scd, 9=Sd, 10=Sdm-Sd/Sm, 11=Sm, 12=Im, 13=Pec, 14=S/BCD, 15=Sm/BCD, 16=Im/BCD, 17=BCD.

Column 10: 100 μm flux density measurement flag. Non detections=0, Detections=1, Confused (i.e., flux density estimate significantly contaminated by the presence of another object)=2. For confused galaxies, flux densities should be considered as an upper limit to the real value.

Column 11: Integrated 100 μm flux density, or upper limit in Jy.

Column 12: Total uncertainty on the 100 μm flux density measurement in Jy.

Column 13: 160 μm flux density measurement flag.

Column 14: Integrated 160 μm flux density, or upper limit in Jy.

Column 15: Total uncertainty on the 160 μm flux density measurement in Jy.

Columns 16-18: Major, minor semi-axis (in arcseconds) and position angle (in degrees) of the aperture used for the photometry.

Column 19: *Herschel* Proposal ID.

This table, as well as all the reduced PACS maps, are publicly available on the Herschel Database in Marseille (HeDaM, `http://hedam.oamp.fr/`).

2.4 Comparison with the literature

In order to check the reliability of the PACS flux density measurements presented here, we compare our far-infrared integrated flux densities with the values presented in the literature, which are based on PACS, *Spitzer*/MIPS or IRAS observations. The results of these comparisons are shown in Fig. 2.

The difference between our flux density estimates and those presented in Dale et al. (2012) is ∼+6% (standard deviation of ∼2-3%), with our flux densities being brighter, although the number statistics is very small (6 galaxies in total). This difference is within the quoted uncertainties, and is mainly due to the different technique used to estimate flux densities (i.e., different background apertures and the use of aperture corrections not adopted in this work).

Auld et al. (2013) recently published PACS flux density measurements for all the VCC galaxies in the HeViCS footprint. A comparison between the flux density estimates for the 65 detected galaxies in common reveals a nice correlation between the two estimates with a standard deviation of just ∼12% and ∼7% at 100 and 160 μm, respectively. However, Auld et al. (2013) measurements are systematically ∼12% and ∼15% lower than ours.

After various tests, we concluded that there are two main reasons for this discrepancy. First, a different flux density estimate technique. Auld et al. (2013) used apertures on average significantly smaller than ours (e.g., see their Fig. 3), and then applied aperture corrections. Indeed, by using our own apertures on the Auld et al. (2013) dataset, we find no systematic offset with our 100 μm data, whereas at 160 μm there is still a difference of ∼12%.

Second, a different data reduction technique. Auld et al. (2013) used the *naive* projection task `photProject` in HIPE

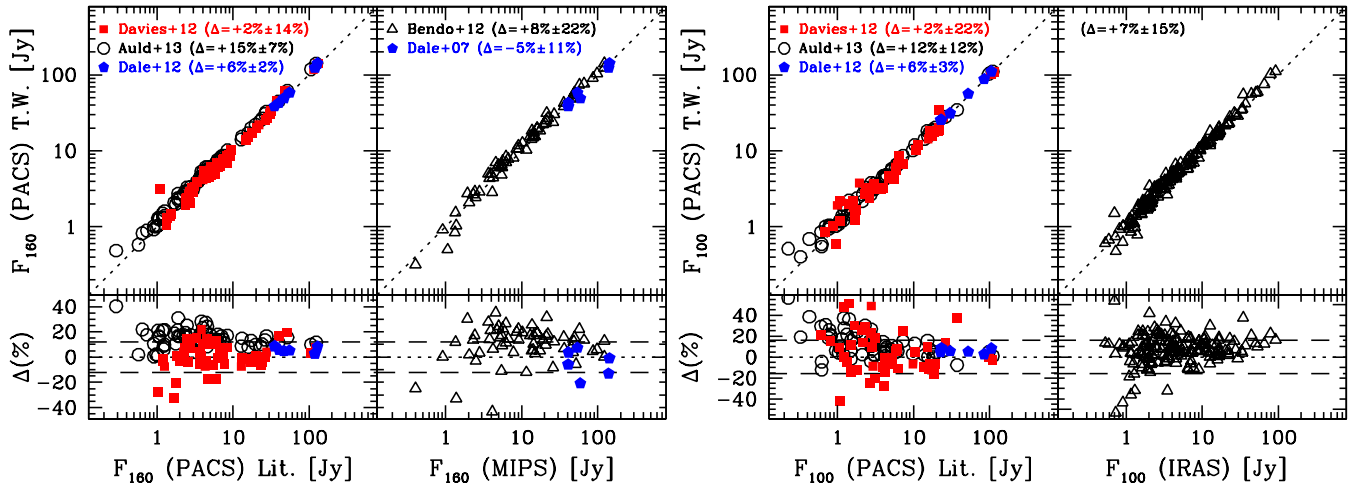

Figure 2. Comparison between our 160 μm (left) and 100 μm (right) flux density estimates and those presented in the literature. The bottom panels show the difference (this work (T.W.) -literature) in percentage for each dataset. For each PACS channel, the left panel shows the comparison with literature estimates based on PACS data, while in the right panel the comparison with *Spitzer*/MIPS and IRAS observations is presented. The dotted lines indicate the one-to-one relation, and the dashed lines the average uncertainty in our flux density estimates.

to reduce PACS images. This requires the use of a high-pass filter to correct for $1/f$ noise, and such procedure could remove diffuse emission associated to extended objects. By using the same apertures on the HeViCS maps reduced with both `photProject` and `Scanamorphos`, we find that `photProject` maps provide flux densities ∼10% lower than those obtained with `Scanamorphos`, while no difference is seen at 100 μm. Thus, the remaining difference at 160 μm is due to the use of `photProject` instead of `Scanamorphos`. Indeed, as mentioned above, this is likely due to the use of high-pass filtering which removes diffuse emission, much more commonly present at 160 μm than at 100 μm (see also Rémy-Ruyer et al. 2013).

We also compared our measurements to those presented by Davies et al. (2012) for the 49 galaxies in common. These are based on an early HeViCS data release and are measured on apertures much more similar to the ones we used. Our flux density measurements agree very well with these estimates (∼+2±22% and ∼+2±14% at 100 and 160 μm, respectively). The scatter is larger than in the case of Auld et al. (2013), but consistent with the typical uncertainty given in Davies et al. (2012). It is likely that, in this case, the different calibration between the two datasets compensates for the intrinsic differences between `photProject` and `Scanamorphos`, providing a set of measurements consistent with our own.

Spitzer/MIPS 160 μm flux densities for 103 galaxies in the HRS have been published by Bendo et al. (2012). In order to perform a proper comparison with our data, we removed those galaxies which were flagged as problematic due to incomplete coverage, or simply being confused with other nearby galaxies of similar surface brightness in Bendo et al. (2012). For the remaining 65 objects in common our flux densities are ∼8% brighter than those of MIPS one, with quite a large scatter (∼22%). This large scatter is mainly due to two galaxies (which fall outside the residual plot in Fig. 2): HRS129, 258. A comparison between the PACS, SPIRE and MIPS data for these galaxies shows that the MIPS data suffer from background confusion effects, making it difficult to separate emission from the target and background sources. Moreover, the MIPS observations for these galaxies were performed in photometry mode, which produces compact maps where it is difficult to measure the background. Once these are removed from the sample, the difference between MIPS and PACS measurements becomes ∼+10±14%. Conversely, the comparison with the *Spitzer*/MIPS 160 μm flux densities presented in Dale et al. (2007) for the 6 SINGS galaxies in our sample shows an average difference of ∼-5±11%. All these values are within the 12% flux calibration uncertainty in MIPS data (Stansberry et al. 2007). A PACS-to-MIPS 160 μm flux density ratio systematically higher than 1 has also been found by comparing pixel-by-pixel photometry of nearby galaxies (Aniano et al. 2012; Draine et al. 2013).

We can thus conclude that our 160 μm PACS flux density measurements are consistent with those of *Spitzer*/MIPS within ∼20%, in agreement with the results obtained by the PACS Team (Paladini et al. 2012).

Finally, we compared our PACS 100 μm flux density estimates with those presented in the IRAS Faint Source Catalogue (164 galaxies after exclusion of confused/contaminated objects), finding an average difference of ∼+7±15% (see also Ali 2011).

We remind the reader that, although the central wavelengths of MIPS and IRAS correspond to those of PACS, the bandpasses are not identical and part of the offsets shown above are certainly due to the different filter responses of the three instruments.

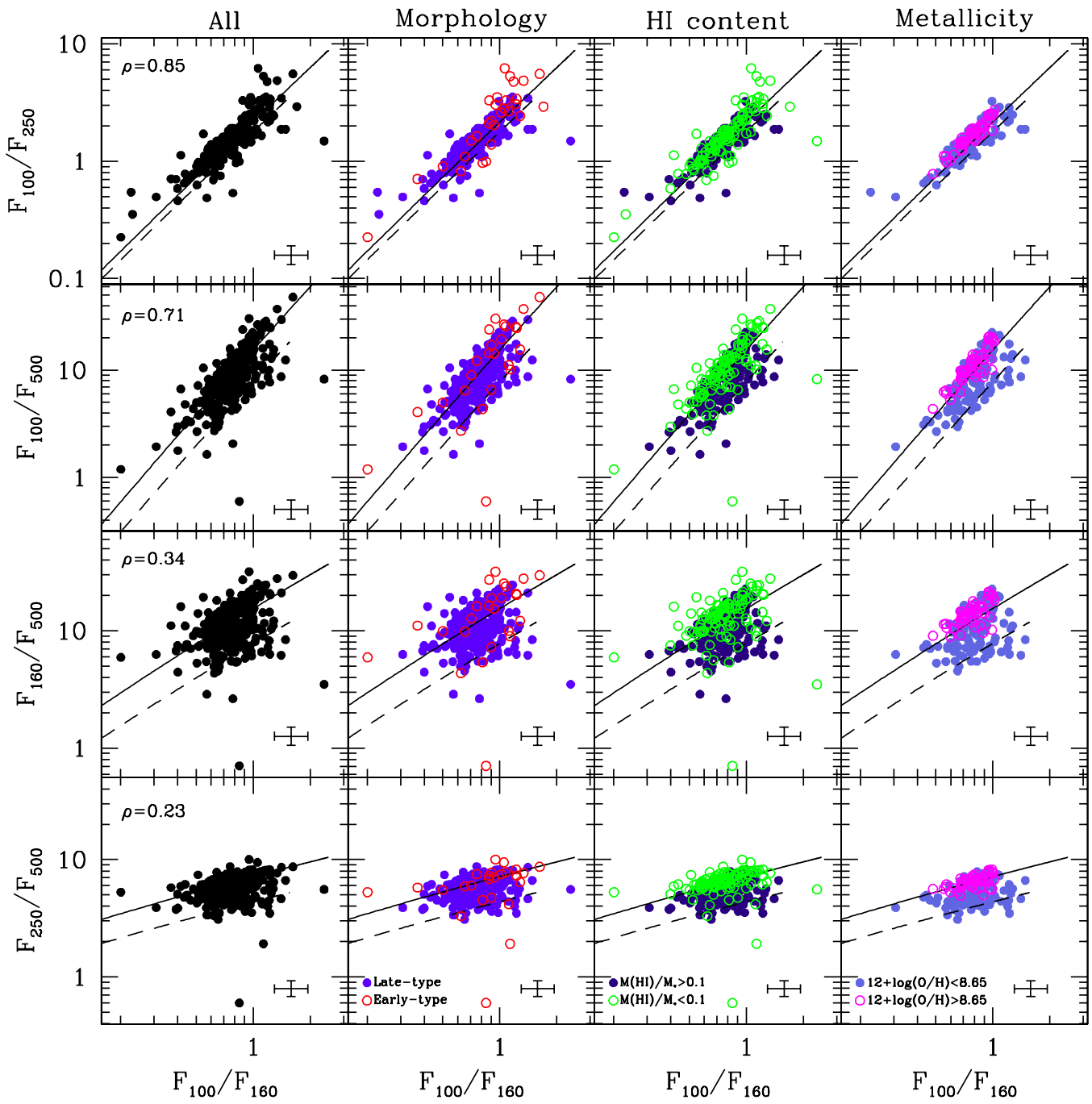

Figure 3. From top to bottom: 100-to-250 μm, 100-to-500 μm, 160-to-500 μm and 250-to-500 μm as a function of the 100-to-160 μm flux density ratio. The first column shows the entire HRS sample, while in the following three columns points are colour-coded according to morphological type (open circles=E+S0, filled circles=Sa and later), HI gas fraction (open circles=log($M(HI)/M_*$)<-1, filled circles=log($M(HI)/M_*$)>-1) and gas phase metallicity (open circles=12+log(O/H)>8.65, filled circles=12+log(O/H)<8.65). The Pearson correlation coefficients (ρ) for the whole sample are shown in the top left corner of each panel. The solid and dashed lines represent the expected colours for a modified black body with β=2 and 1, respectively. We consider a temperature range between 10 and 40 K. Typical errorbars are shown on the bottom right corner of each panel.

3 FAR-INFRARED/SUB-MILLIMETER COLOURS AS A PROXY FOR THE SHAPE OF THE DUST SED

In the last few years, several studies have shown how infrared colours can be used as a proxy of dust properties (e.g., Boselli et al. 2010a, 2012; Dale et al. 2012; Bendo et al. 2010, 2012; Galametz et al. 2010; Boquien et al. 2011; Rémy-Ruyer et al. 2013). The novelty of the present work is that, for the first time, we cover the 100-500 μm domain for a representative sample of galaxies spanning a large range in stellar mass, star formation activity, cold gas and metal content. For example, compared to the work pre-

Table 2. The Pearson correlation coefficients (ρ) and scatter (σ) of the best-fitting bisector linear fit for each sample shown in the colour-colour relations of Fig. 3.

Sample	$F_{100}/F_{160} - F_{100}/F_{250}$			$F_{100}/F_{160} - F_{100}/F_{500}$			$F_{100}/F_{160} - F_{160}/F_{500}$			$F_{100}/F_{160} - F_{250}/F_{500}$		
	N	ρ	σ	N	ρ	σ	N	ρ	σ	N	ρ	σ
All	282	0.84	0.05	274	0.70	0.10	274	0.30	0.14	274	0.23	0.12
$Early-type$	29	0.88	0.09	25	0.71	0.17	25	0.39	0.23	25	0.14	0.14
$Late-type$	253	0.83	0.05	249	0.69	0.10	249	0.27	0.14	249	0.28	0.12
$M(HI)/M_{\odot} < 0.1$	106	0.84	0.04	101	0.68	0.06	101	0.26	0.09	101	0.13	0.10
$M(HI)/M_{\odot} > 0.1$	169	0.84	0.06	167	0.71	0.11	167	0.34	0.15	167	0.34	0.11
$12 + log(O/H) > 8.65$	50	0.95	0.02	50	0.88	0.03	50	0.66	0.05	50	0.53	0.05
$12 + log(O/H) < 8.65$	112	0.86	0.06	110	0.73	0.11	110	0.32	0.15	110	0.33	0.10

sented in Boselli et al. (2012), which focused on HI-normal spiral galaxies only, this analysis takes advantage of a more complete coverage at wavelengths shorter than 250 μm, and includes the entire HRS sample detected by *Herschel* (282 versus 146 objects). Similarly, the number of HRS galaxies detected at all PACS and SPIRE wavelengths is significantly larger (i.e., 282 versus 195) than that of Auld et al. (2013), which focuses on Virgo cluster galaxies only.

Particularly interesting is to quantify how well the shapes of the dust SED at the short and long wavelength-ends correlate among each other. Indeed if, in the 100-500 μm wavelength range, the dust SED can be well approximated by a single modified black-body with fixed β (i.e., the variation of the dust emissivity with frequency described by $\kappa_{\nu} = \kappa_0 \times (\nu/\nu_0)^{\beta}$), all FIR/sub-mm colours should be strongly correlated.

The SPIRE flux densities are obtained from Ciesla et al. (2012), but we applied several corrections to these flux estimates. We multiplied their values by 1.0253, 1.0250 and 1.0125 at 250, 350 and 500 μm to take into account the new SPIRE calibration (v.11), and then by 0.9097, 0.9136 and 0.8976 at 250, 350 and 500 μm, to correct for the new beam areas (Bendo et al. 2013; Herschel Space Observatory 2013). We did not make any attempt to include variations of the beam size as a function of the shape of the SED (Herschel Space Observatory 2013), as these are generally within the measurement errors ($\lesssim$10%). Moreover, such correction would mainly result in a systematic offset in the flux densities, whereas the relative variation between the SPIRE bands would be $\lesssim$3% for the ranges of β investigated here. Thus, we are confident that this does not affect our conclusions.

In Fig. 3 we plot the 100-to-160 μm flux density ratio, which usually embraces the peak of the dust SED, as a function of various flux density ratios (i.e., from top to bottom: 100-to-250 μm, 100-to-500 μm, 160-to-500 μm and 250-to-500 μm) sensible to the shape of the SED at increasingly longer wavelengths[2]. Similar results are found if additional colours (e.g., including the 350μm flux density) are used.

It is clear that the farther away in wavelength two colours are, the weaker their correlation is, as already noted by Boselli et al. (2012). Indeed, the Pearson correlation coefficient (ρ) decreases from $\sim$0.8 to $\sim$0.2 when moving from the 100-to-250 μm to the 250-to-500 μm flux density ratios (see first column of Fig. 3). Intriguingly, the increase of a factor of $\sim$3 in scatter (σ)[3] observed when moving from the top to the third panel appears to be due to a population of galaxies that detaches from the main relation. To see if this is indeed the case, in Fig. 3 we highlight galaxies according to (from left to right) their morphological type, the ratio of their atomic cold gas (HI) to stellar mass content and gas-phase metallicity. HI measurements have mainly been obtained from Haynes et al. (2011) and Springob et al. (2005), and are presented in Boselli et al. (2014)[4]. Stellar masses are from Cortese et al. (2012a), and gas-phase metallicities (i.e., oxygen abundances) converted into the Pettini & Pagel (2004) O3N2 base metallicity are taken from Hughes et al. (2013). We use 12+log(O/H)=8.65 (above which the stellar vs. mass metallicity relation starts flattening, Kewley & Ellison 2008) and $M(HI)/M_{*}$ =0.1 (below which the stellar mass vs. HI fraction relation is no longer linear, Cortese et al. 2011; Bothwell et al. 2009) to divide gas-rich/metal-poor from gas-poor/metal-rich galaxies. The Pearson correlation coefficients and scatter around the best-fitting bisector linear fit are indicated in Table 2.

Gas-rich/metal-poor galaxies seem to be responsible for the significant increase in scatter when moving from the 100-to-250 μm to the 160-to-500 μm colour-colour plots. If we consider gas-poor/metal-rich galaxies only, the scatter in the three bottom panels of Fig. 3 decreases by at least a factor $\sim$2. Indeed, performing a Kolmogorov-Smirnov test, we found that there is only a $\sim$4% chance that the 160-to-500 μm colour distributions of metal-poor (12+log(O/H)<8.65) and metal-rich (12+log(O/H)>8.65) galaxies are drawn from the same population, as already demonstrated by Boselli et al. (2012). We note that some galaxies do not appear in the third and fourth column of Fig. 3. This is because for some objects HI and metallicity information is not available.

Our findings suggest that, in the 100-500 μm regime, the shape of the dust SED for galaxies with stellar mass

[2] In order to avoid the need to apply colour corrections when comparing with model predictions, here we plot the ratio of the responsivity function-weighted flux density measurements.

[3] In order to minimize the effect of outlier galaxies, the scatter is defined as the interquartile of the distribution of perpendicular distances from the best-fitting bisector linear fit for each sample.

[4] This is an updated version of the values presented in Cortese et al. (2011, 2012b), which takes advantage of the recently published ALFALFA flux densities (Haynes et al. 2011) for a considerable fraction of the HRS footprint.

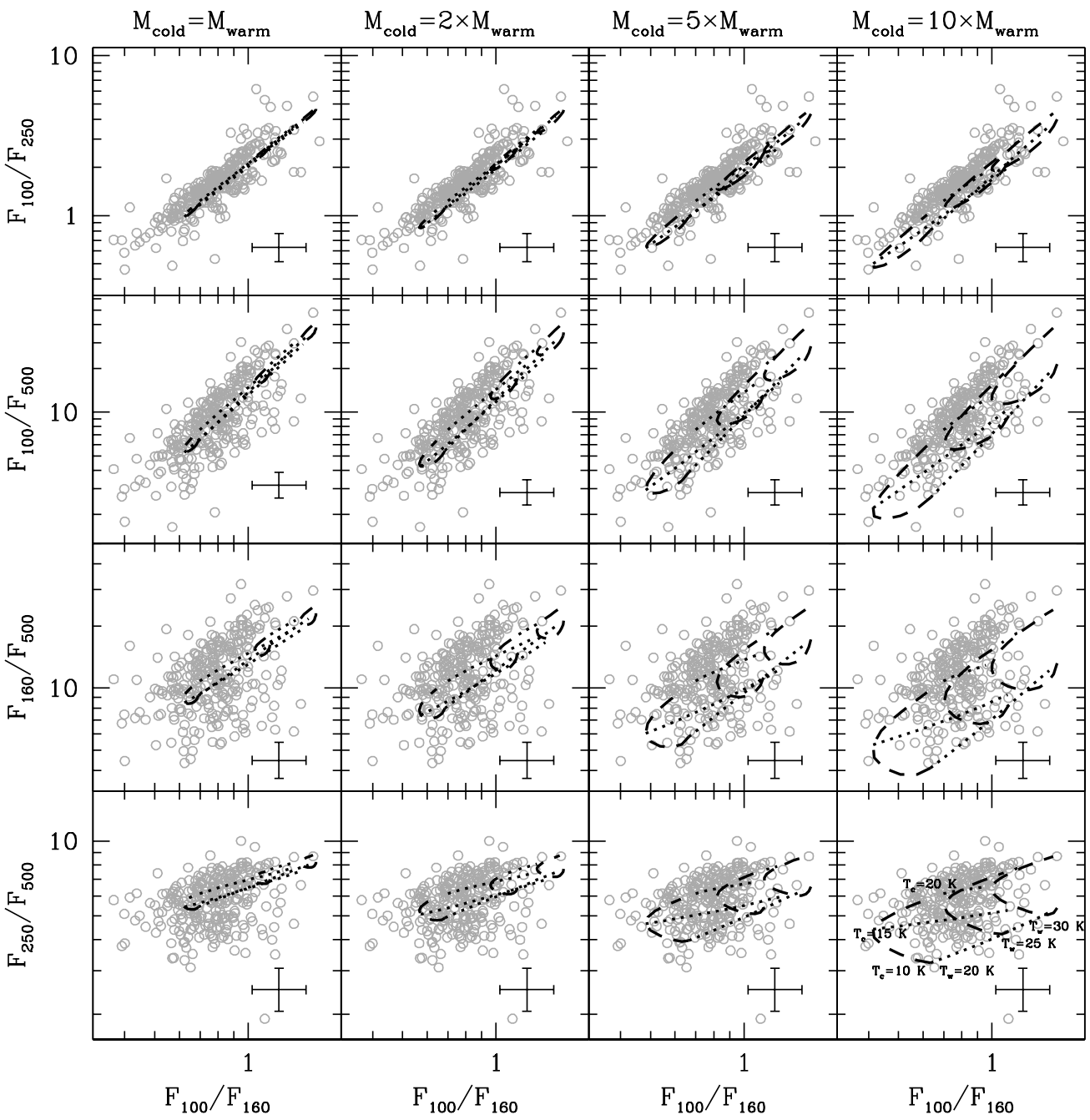

Figure 4. Same as Fig. 3, but with the predictions for two temperatures modified black-body SEDs with β=2 overplotted on the data points. In each plot, isotherms for the cold (T_c=10, 15 and 20 K) and warm (T_w=20, 25 and 30K) dust components are indicated by the dotted and dashed lines, respectively. Cold-to-warm dust mass ratios are 1, 2, 5 and 10 from left to right.

$10^8 \lesssim M_*/M_\odot \lesssim 10^{12}$ cannot be reproduced by simply varying the value of the average dust temperature. In other words, either β must also vary (Boselli et al. 2012; Smith et al. 2012; Rémy-Ruyer et al. 2013) or multiple temperatures components are required (Shetty et al. 2009; Dunne & Eales 2001; Boquien et al. 2011; Bendo et al. 2012; Clemens et al. 2013).

In order to visually illustrate this result, we plot in Fig. 3 and 4 the colours expected for these two different scenarios. In Fig. 3 we show the flux density ratios derived from single modified black-bodies with temperatures ranging from 10 and 40 K and β values fixed to 2 (solid line) and 1 (dashed line). In Fig. 4, we show a combination of two modified black-bodies with β=2. We vary the cold dust temperature (T_c) from 10 to 20 K, and the warm dust temperature (T_w) from 20 to 30 K. The four columns show different mass ratios M_{cold}/M_{warm} increasing from 1 (left) to 10 (right).

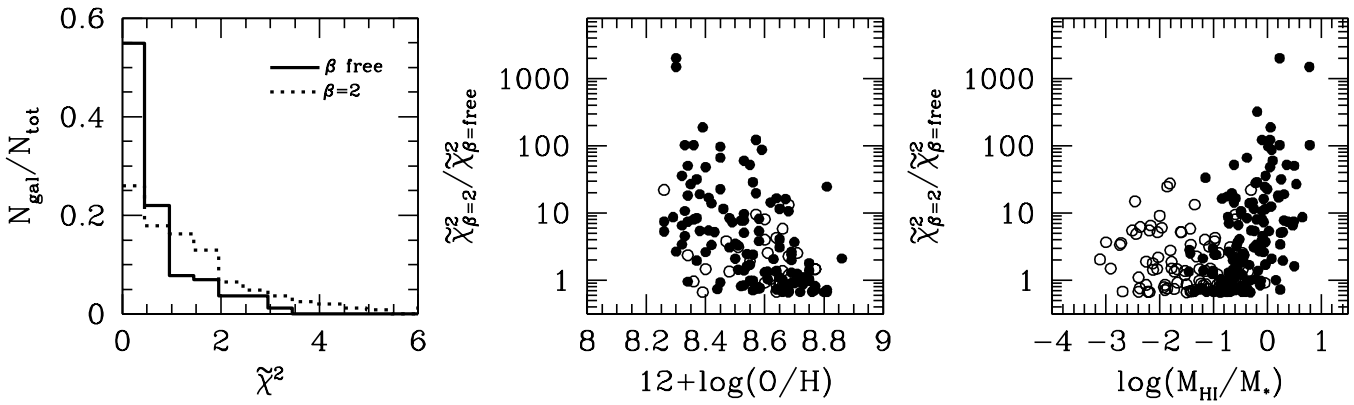

Figure 5. The left panel shows the distribution of reduced χ^2 ($\tilde{\chi^2}$) for the best-fitting single modified black-body with β=free (solid line) and β=2 (dashed). The ratio of $\tilde{\chi^2}$ obtained for the two cases as a function of gas-phase metallicity and HI gas fraction are presented in the central and right panel, respectively. Empty circles show galaxies with HI deficiency greater than 0.5. We show only those galaxies for which at least one of the two $\tilde{\chi^2}$ corresponds to a probability $P \geq$95%.

It is clear that, while the temperature is the main driver of the trends observed in each colour-colour plot, only a variation in β, or an additional temperature component, can explain the increasing scatter when moving from the 100-to-250 μm to 160-to-500 μm colours. Interestingly, the two temperature components scenario is able to reproduce the observed range of colours only if the warm component contributes negligibly to the total dust budget of the galaxy (i.e., $M_{cold}/M_{warm} \gtrsim 5$; Vlahakis et al. 2005). This is easy to understand if we consider the fact that, at fixed dust mass, the flux density emitted by a black-body in the FIR/submm wavelength range increases with temperature. Thus, if the warm and cold components have the same dust mass, the warm dust dominates the total emission, and the shape of the SED is very close to that of a single black-body. Only if the cold dust component dominates the mass budget, the shape of the combined SED deviates significantly from a single black-body.

Unfortunately, with our current data it is impossible to discriminate between a varying β and a multiple temperature component scenario. Our lack of coverage below 100 μm makes it meaningless to perform a two temperatures fit, as the warm component is not constrained. Thus, in the rest of this paper we will focus on the single modified black-body case only, and investigate how different assumptions on β can affect the interpretation of *Herschel* observations. A detailed comparison with the predictions of the Draine et al. (2007) dust models will be presented in a forthcoming paper (Ciesla et al., submitted.).

4 FITTING THE DUST SED WITH A SINGLE MODIFIED BLACK-BODY

4.1 How well do colours trace the average dust temperature?

The results presented in the previous section show that FIR/sub-mm colours may not always represent a proxy for the average underlying dust temperature. In order to investigate this issue in more detail, it is interesting to quantify how the FIR/sub-mm colours correlate with the parameters obtained from a single modified black-body fitting. We assume either a constant value of β=2, or keep this as a free parameter. The model functions were convolved with the PACS and SPIRE filter response functions and fitted to the relative spectral responsivity function-weighted flux density measurements. Best-fit parameters and their 1σ uncertainties are determined via a χ^2 minimisation using the Python version of the minimisation library `MINUIT` (James & Roos 1975). We choose β=2 simply because this seems to correctly reproduce the shape of the SED for massive, metal-rich spiral galaxies in the local Universe (Davies et al. 2012; Boselli et al. 2012; Draine et al. 2013). However, our results do not qualitatively change if a different (but fixed) value of β is used. In the rest of the paper, we consider only those objects detected in all 5 PACS/SPIRE bands, and for which the reduced χ^2 ($\tilde{\chi^2}$) corresponds to a probability $P \geq$95%: i.e., $\tilde{\chi^2}_{dof=3}$ <2.6 (203 galaxies) and $\tilde{\chi^2}_{dof=2}$ <3 (242 galaxies) for a fixed and variable β, respectively. The best-fit dust masses and temperatures for these galaxies, as well as their distance, are provided in Table 3. This guarantees that we are not contaminated by objects whose FIR/submm emission is dominated by synchrotron emission (Baes et al. 2010).

A comparison between the reduced χ^2 obtained for the β=free and β=2 cases is shown in Fig. 5. Not surprisingly, leaving β free provides on average better fits. Moreover, as shown in the central and right panel of Fig. 5, the difference between the two techniques increases when moving towards metal-poor/gas-rich systems. This is even more evident when HI-deficient galaxies (i.e., Def_{HI} >0.5, empty points in Fig. 5), for which the gas content is no longer a good indicator of enrichment history (Cortese & Hughes 2009; Hughes et al. 2013), are excluded (ρ =0.38 and 0.54 for all galaxies and HI-normal systems only, respectively).

In Fig. 6, we show how the FIR/sub-mm colours correlate with the best-fit parameters obtained from our SED fitting. Not surprisingly, all SPIRE and PACS colours strongly correlate with dust temperature if β is kept fixed (we note that these results do not qualitatively change if we fix β to a different value). It is also expected that the lowest scatter is observed for the colour spanning the largest wavelength range (i.e., the 100-to-500 μm flux density ratio), as the vari-

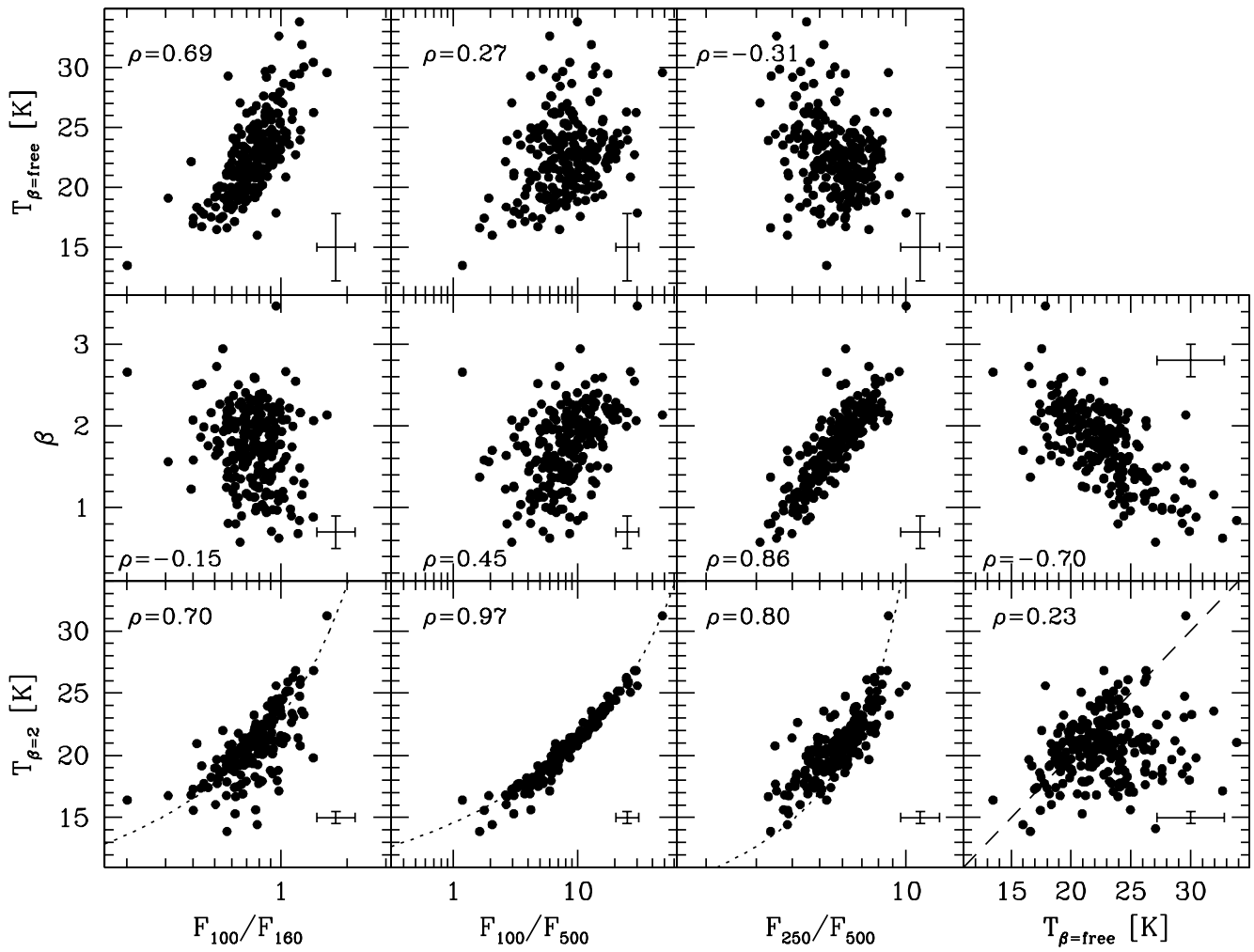

Figure 6. The modified black-body best-fitting parameters as a function of far-infrared/sub-millimeter colours (from left to right: 100-to-160 μm, 100-to-250 μm, 100-to-500 μm and 250-to-500 μm flux density ratio). The bottom row shows the dust temperature obtained by keeping β fixed to 2, while the middle and top rows show the best-fitting values for β and T obtained by varying both parameters freely. The Pearson correlation coefficients are indicated in each panel. In the bottom row, the dotted lines show the expected relations between temperature and colour for a single modified black-body with β=2, while the dashed line indicates the 1-to-1 relation.

ation in colour is larger, and less affected by measurement errors.

More interesting is the case when β is treated as a free parameter. In this case, there is a clear difference in the colours behaviour when crossing a λ of $\sim$200 μm. At shorter wavelengths, there is still a strong correlation of colour with temperature (ρ $\sim$0.7), while only a very weak trend is seen with β (ρ $\sim$-0.15). Moving to longer wavelengths, the trends with temperature become weaker, and reverse for the 250-to-500 μm colour (ρ $\sim$-0.3), whereas the correlation with β becomes gradually stronger. The best relation is found with the 250-to-500 μm flux density ratio (ρ $\sim$0.9), which appears to be mainly tracing variations of β and not dust temperature, as also shown in Fig. 3. These results are likely a direct consequence of the fact that the FIR/submm SED for our sample peaks at λ <200 μm, and while the PACS colours trace the peak of the dust SED, any variations in the emissivity of the grains will predominantly affect the SPIRE colours. The average value of β for HRS galaxies is $\sim$1.8$\pm$0.5, a value consistent with what is found in the Milky Way and in other nearby galaxies (Planck Collaboration et al. 2013; Galametz et al. 2012; Boselli et al. 2012; Smith et al. 2012, 2013).

An important issue affecting any modified black-body χ^2 fitting with β and T as free parameters is the known anti-correlation between them, which is clearly shown in the right column of Fig. 6. While it is still debated whether part of this anti-correlation has a physical origin (Shetty et al. 2009; Galametz et al. 2012; Smith et al. 2012; Juvela & Ysard 2012; Juvela et al. 2013; Rémy-Ruyer et al. 2013; Tabatabaei et al. 2013), there is no doubt that it is mainly due to the χ^2 fitting technique (Shetty et al. 2009). Indeed, in the 2D β vs. T plane, the region corresponding to the absolute minimum of χ^2 depends on both quantities, giving rise to an anti-correlation between β and T. This is clearly visible by just looking at the 2D confidence levels for any χ^2 modified black-body fit. Since in the first and third columns of Fig. 6 temperature and β show opposite trends with colour, it is very likely that they are affected by this degeneracy. However, the significant difference in scatter be-

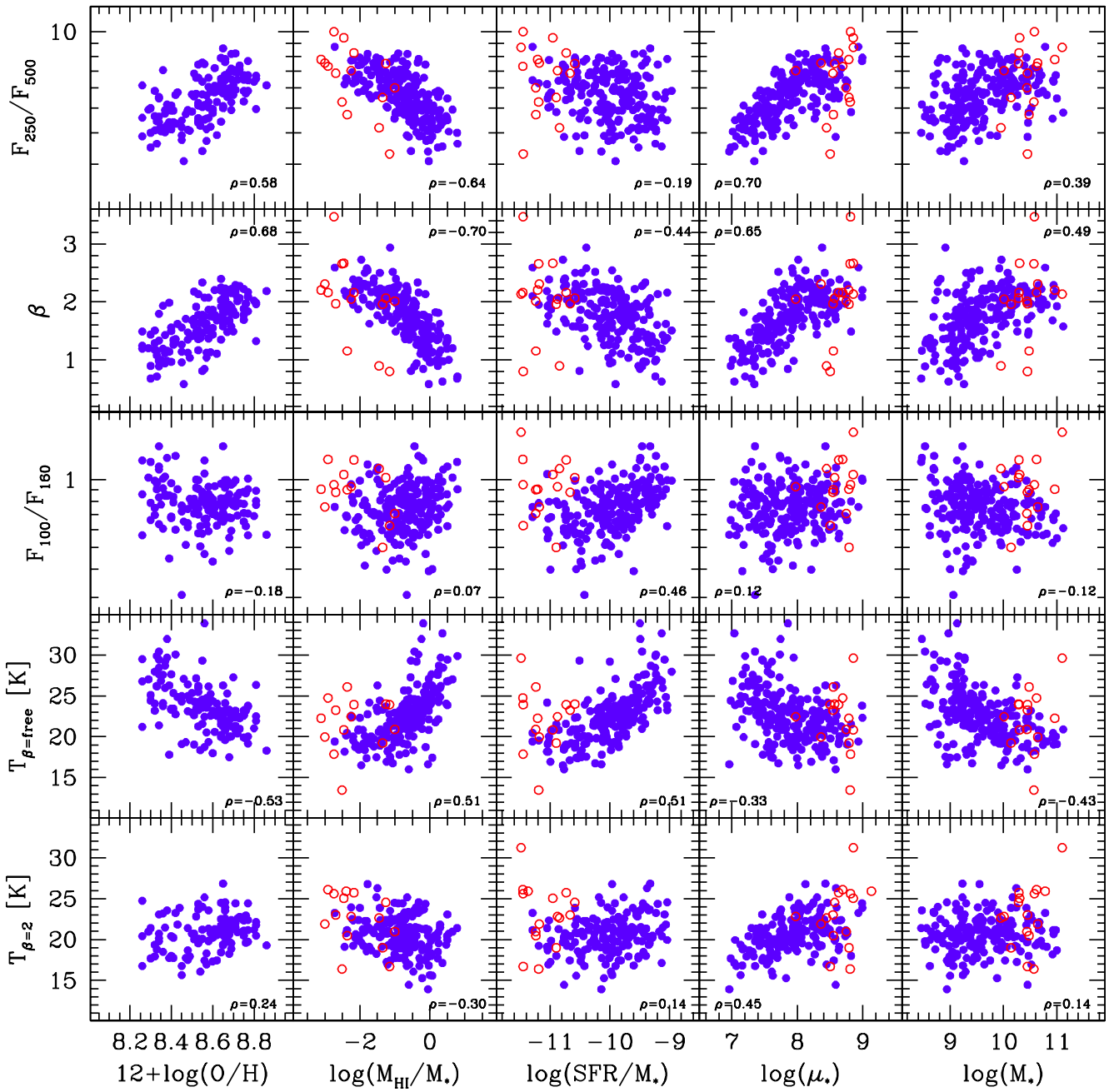

Figure 7. From top to bottom: the 250-to-500 μm flux density ratio, the best-fitting value of β, the 100-to-160 μm flux density ratio, the best fitting temperature assuming β=free and β =2 as a function of stellar mass, stellar mass surface density (μ_*), specific star formation rate (SFR/M_*), HI gas fraction (M_{HI}/M_*) and gas phase metallicity (12+log(O/H). Filled and open circles show late- and early-type galaxies, respectively. The Pearson correlation coefficients for the whole sample are shown in each panel.

tween the various relations suggests that the 100-to-160 μm colour vs. T and 250-to-500 μm colour vs. β are less contaminated than the other correlations. As mentioned above, this is because the PACS colours mainly trace the peak of the dust SED, whereas the SPIRE ones are mostly sensitive to variations in the dust emissivity.

4.2 The relation between dust temperature, β and integrated galaxy properties

In this section we investigate further how the variation of β, necessary to reproduce the observed colours of HRS galaxies in a single modified black-body scenario, is mirrored by a variation in galaxy properties. For comparison, we will also show the results obtained by keeping β fixed, since we consider this an instructive exercise to illustrate how the model assumptions influence the parameters we derive. In Fig. 7, we show how the best-fitting dust parameters, as well as the

100-to-160 μm and 250-to-500 μm flux density ratios, are related to gas-phase metallicities, HI gas fractions, specific star formation rate (SFR/M_*), stellar mass surface density [μ_*=$M_*/(2\pi R^2_{50,i})$ where $R_{50,i}$ is the radius containing 50% of the total i-band light] and stellar mass. Star formation rates are determined by combining WISE 22μm (Ciesla et al., submitted.) and NUV photometry (Cortese et al. 2012a) using the recipes presented in Hao et al. (2011) as described in Cortese (2012).

By comparing the two bottom rows of Fig. 7, it is clear that the assumptions made on β significantly influence the correlations between temperature and integrated galaxy properties. For β fixed to 2, the strongest correlation is found with stellar mass surface density (ρ ∼0.45). A weak anti-correlation is visible with gas-fraction (ρ ∼-0.3), while no correlation is found with specific star formation rate, stellar mass or metallicity (ρ ≲0.2). Quite different results are obtained if β is left free. In this case, the temperature anti-correlates very weakly with μ_* (ρ ∼-0.3), while it is strongly correlated with SFR/M_* (see also Clemens et al. 2013), HI gas fraction, metallicity and stellar mass (ρ ∼0.5). Even more importantly, some of the correlations show opposite trends. For a fixed value of β, the temperature increases with metallicity and stellar mass surface densities, whereas it decreases for β=free. The 'reversal' of these correlations is driven exclusively by metal-poor/gas-rich galaxies, and it is simply a consequence of the fact that, for these objects, the best-fitting value of β is significantly lower than 2. Thus, many of the correlations shown in Fig. 7 depend on the assumptions made about the dust SED, and may not be physical (Magnelli et al. 2012; Roseboom et al. 2013).

In particular, we have shown (see Fig. 6) that the 100-to-160 μm and 250-to-500 μm flux density ratios are the best proxies for T and β, respectively. If all the trends observed in Fig. 7 are physical, we should find similar correlations when T and β are replaced by the flux density ratios. However, this is not always the case. The 100-to-160 μm flux density ratio correlates only with SFR/M_* (ρ ∼0.5), while the 250-to-500 μm ratio correlates weakly with SFR/M_* (ρ ∼-0.2), but varies strongly with stellar mass, stellar mass surface density, HI gas fraction and gas-phase metallicity (ρ ∼0.6-0.7). Thus, the T vs. HI gas fraction and β vs. SFR/M_* trends might be spurious.

In summary, our analysis confirms that the typical dust temperature of a galaxies as measured from a single modified black-body is mainly related to specific star formation rate, while β varies more with the degree of metal enrichment of the ISM. As discussed in the previous section, at this stage it is impossible to determine whether the variation of β across the HRS indicates a variation in the dust properties/composition, or it simply highlights the need of multiple temperature components for gas-rich/metal-poor/low-mass galaxies.

4.3 Dust mass estimates

It is interesting to investigate how the variation of β across the HRS for a single modified black-body affects the estimate of the dust mass reservoir. Thus, in the left panel of Fig. 8, we compare the dust masses obtained for β=free and β=2. Dust masses have been calculated from Eq. 1 assuming ν_0 =856.5 GHz (i.e., 350 μm) and κ_0 =0.192 m^2 kg^{-1} (Draine 2003). It is evident that dust masses are significantly less affected than dust temperatures by the assumptions made on β. The average difference between the two measurements is ∼0.08 dex, with a standard deviation of 0.15 dex, which is consistent with the typical statistical error obtained from the SED fitting: ∼0.05 and 0.1 dex for β=2 and β=free. Not surprisingly, the largest difference is observed in gas-rich galaxies (filled circles, Δ=0.14±0.14 dex), while the two techniques give consistent results for gas-poor systems (empty circles, Δ=-0.02±0.11 dex).

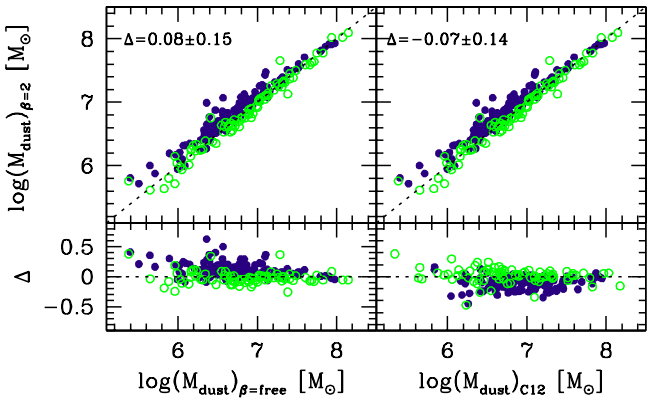

Figure 8. *Left panel*: Comparison between the dust masses obtained from a black-body SED fitting with β =2 and β =free. *Right panel*: Dust masses obtained from a black-body SED fitting with β =2 as a function of those obtained using the empirical recipes of Cortese et al. (2012b), which are based on SPIRE colours only. Filled and empty circles indicate gas-rich and gas-poor galaxies, respectively (see also Fig. 3).

This result implies that correlations involving dust masses are quite robust against the assumptions made on the shape of the SED. Different assumptions can certainly affect the exact slope of the dust scaling relations, but they are not able to produce the same dramatic inversion of some correlations observed for the dust temperature (see Fig. 7).

This conclusion is reinforced by the fact that the differences, already quite small, between the two cases might be overestimated, as we varied β, by keeping fixed the value of dust opacity κ_0 used to determine the dust mass. As recently shown by Bianchi (2013), this is not entirely correct because the value of κ_0 is calibrated on a dust model with a well defined value of β. Thus, if β changes, κ_0 should change as well. Unfortunately, varying κ along with β is far from trivial, and it is only possible by either having a consistent dust model for each value of β, or by comparing dust mass estimates obtained from SED fitting with the ones obtained from other independent methods: e.g., using the amount of cold gas and metals, as proposed by James et al. (2002).

Finally, it is interesting to compare the dust masses estimated by fitting a single modified black-body with β=2, to those obtained by using the empirical recipes developed by Cortese et al. (2012b), which assume β=2 but are based on SPIRE data only. In this way we can quantify the benefit provided by inclusion of the PACS data in the dust mass estimates. As shown in the right panel of Fig. 8, the two estimates show a good agreement with a mean difference of -0.07 dex and a standard deviation of 0.14 dex, lower than the typical uncertainty of 0.2 dex in the recipes by Cortese et al. (2012b). Even in this case, the largest offset

(-0.12±0.11 dex) is found for gas-rich galaxies. This is a natural consequence of the fact that, for these objects, the shape of the dust SED is no longer perfectly consistent with β=2.

Thus, while dust mass estimates based on SPIRE colours are a reliable tool for estimating dust masses within 0.2 dex, only a complete coverage of the 100-500 μm wavelength range can provide us with accurate (within 0.1dex) dust mass estimates necessary to quantify in great detail the correlation between dust mass and other galaxy properties.

5 SUMMARY & CONCLUSIONS

In this paper we presented PACS 100 and 160 μm integrated photometry for the *Herschel* Reference Survey. We have combined these data with SPIRE observations to investigate how the shape of dust SED varies across the Hubble sequence. Being the largest representative sample of nearby galaxies with homogeneous coverage in the 100-500 μm wavelength domain, the HRS is ideal to quantify if and how dust emission varies across the local galaxy population. Our main results are as follows.

- The shape of the dust SED is not well described by a single modified black-body having just the dust temperature as a free parameter. Instead, there is a clear need to vary the dependence of the dust emissivity (β) on wavelength, or to invoke multiple temperature components in order to reproduce the colours observed in our sample. This is particularly important as the HRS does not include very metal-poor dwarf galaxies, for which we already knew that the dust SED is significantly different from the one of metal-rich, massive galaxies (Galliano et al. 2005, 2011; Engelbracht et al. 2008; Galametz et al. 2009; Rémy-Ruyer et al. 2013). Our results suggest that the difference in FIR/sub-mm colours between giant and dwarf galaxies (Draine & Li 2007) may not be the result of a dramatic transition in dust properties, but just the consequence of the gradual variation that we observe as a function of metal and gas content.
- The variation in the slope of the dust SED strongly affects dust temperature estimates from single modified blackbodies fits. In particular, the correlations between galaxy properties and dust temperatures strongly depend on the assumptions made on β: i.e., trends can disappear or even reverse. Conversely, dust mass estimates are more robust, and variations in β do not produce the same dramatic inversion of some correlations observed for the dust temperature.
- We confirm that the temperature of a single modified black-body is mainly related to specific star formation rate, while β varies more with the degree of metal enrichment of the ISM.

The results presented in this paper may appear in contradiction with several recent works showing that the dust SED is very well reproduced by a simple modified blackbody with β =2 (Davies et al. 2012; Auld et al. 2013). However, all these works were focused on massive, metal-rich and relative gas-poor galaxies, for which we also find that a constant value of β provides a good fit to our data. It is when we move to the gas-rich/metal-poor regime that the shape of the SED starts to change (Boselli et al. 2010a, 2012; Rémy-Ruyer et al. 2013).

Our findings overall reinforce the results already presented in Boselli et al. (2010a, 2012). However, it is important to note that the discovery of a clear variation in the shape of the SED across the HRS has only been possible thanks to the large wavelength coverage obtained by combining both PACS and SPIRE data. Indeed, with SPIRE or PACS data only, it would be not only much more difficult to show under which conditions a simple modified black-body approach does not work, but it would also be nearly impossible to quantify how model assumptions can affect the correlation of dust temperature with star formation, galaxy structure and chemical enrichment.

ACKNOWLEDGMENTS

We thank an anonymous referee for his/her very useful comments and suggestions which have significantly improved this manuscript. LC thanks B. Draine for useful discussions, and B. Catinella for comments on this manuscript. We thank all the people involved in the construction and the launch of *Herschel*.

The research leading to these results has received funding from the European Communitys Seventh Framework Programme (/FP7/2007-2013/) under grant agreement No 229517, and was supported under Australian Research Council's Discovery Projects funding scheme (project number 130100664). IDL is a postdoctoral researcher of the FWO-Vlaanderen (Belgium).

PACS has been developed by a consortium of institutes led by MPE (Germany) and including UVIE (Austria); KU Leuven, CSL, IMEC (Belgium); CEA, LAM (France); MPIA (Germany); INAF-IFSI/OAA/OAP/OAT, LENS, SISSA (Italy); IAC (Spain). This development has been supported by the funding agencies BMVIT (Austria), ESA-PRODEX (Belgium), CEA/CNES (France), DLR (Germany), ASI/INAF (Italy), and CICYT/MCYT (Spain). SPIRE has been developed by a consortium of institutes led by Cardiff University (UK) and including Univ. Lethbridge (Canada); NAOC (China); CEA, LAM (France); IFSI, Univ. Padua (Italy); IAC (Spain); Stockholm Observatory (Sweden); Imperial College London, RAL, UCL-MSSL, UKATC, Univ. Sussex (UK); and Caltech, JPL, NHSC, Univ. Colorado (USA). This development has been supported by national funding agencies: CSA (Canada); NAOC (China); CEA, CNES, CNRS (France); ASI (Italy); MCINN (Spain); SNSB (Sweden); STFC (UK); and NASA (USA).

Part of the HRS data was accessed through the Herschel Database in Marseille (HeDaM - `http://hedam.lam.fr`) operated by CeSAM and hosted by the Laboratoire d'Astrophysique de Marseille.

We acknowledge the use of the NASA/IPAC Extragalactic Database (NED) which is operated by the Jet Propulsion Laboratory, California Institute of Technology, under contract with the National Aeronautics and Space Administration.

REFERENCES

Abazajian K. N. et al., 2009, ApJS, 182, 543

Ali B., 2011, PACS Herschel, https://nhscdmz2.ipac.caltech.edu/pacs/docs/Photometer/PICC-NHSC-TN-022.pdf
Aniano G. et al., 2012, ApJ, 756, 138
Auld R. et al., 2013, MNRAS, 428, 1880
Baes M. et al., 2010, A&A, 518, L53+
Balog Z. et al., 2013, Experimental Astronomy, in press (arXiv1309.6099)
Bendo G. J. et al., 2012, MNRAS, 419, 1833
Bendo G. J., Galliano F., Madden S. C., 2012, MNRAS, 423, 197
Bendo G. J. et al., 2013, MNRAS, 433, 3062
Bendo G. J. et al., 2010, A&A, 518, L65+
Bernard J.-P. et al., 2010, A&A, 518, L88
Bianchi S., 2013, A&A, 552, A89
Binggeli B., Sandage A., Tammann G. A., 1985, AJ, 90, 1681
Boquien M. et al., 2011, AJ, 142, 111
Boselli A. et al., 2010a, A&A, 518, L61+
Boselli A. et al., 2012, A&A, 540, A54
Boselli A., Cortese L., Boquien M., 2014, A&A in press
Boselli A. et al., 2010b, PASP, 122, 261
Boselli A., Gavazzi G., Sanvito G., 2003, A&A, 402, 37
Boselli A., Hughes T. M., Cortese L., Gavazzi G., Buat V., 2013, A&A, 550, A114
Boselli A., Sauvage M., Lequeux J., Donati A., Gavazzi G., 2003, A&A, 406, 867
Bothwell M. S., Kennicutt R. C., Lee J. C., 2009, MNRAS, 400, 154
Burgarella D. et al., 2013, A&A, 554, A70
Calzetti D., Bohlin R. C., Kinney A. L., Storchi-Bergmann T., Heckman T. M., 1995, ApJ, 443, 136
Ciesla L. et al., 2012, A&A, 543, A161
Clemens M. S. et al., 2013, MNRAS, 433, 695
Compiègne M. et al., 2011, A&A, 525, A103+
Cortese L., 2012, A&A, 543, A132
Cortese L. et al., 2012a, A&A, 544, A101
Cortese L., Catinella B., Boissier S., Boselli A., Heinis S., 2011, MNRAS, 415, 1797
Cortese L. et al., 2012b, A&A, 540, A52
Cortese L., Hughes T. M., 2009, MNRAS, 400, 1225
Dale D. A. et al., 2012, ApJ, 745, 95
Dale D. A. et al., 2007, ApJ, 655, 863
Davies J. I. et al., 2010, A&A, 518, L48+
Davies J. I. et al., 2012, MNRAS, 419, 3505
Dole H. et al., 2006, A&A, 451, 417
Draine B. T., 2003, ARA&A, 41, 241
Draine B. T. et al., 2013, ApJ submitted (arXiv:1306.2304)
Draine B. T. et al., 2007, ApJ, 663, 866
Draine B. T., Li A., 2007, ApJ, 657, 810
Dreyer J. L. E., 1888, MmRAS, 49, 1
Dreyer J. L. E., 1895, MmRAS, 51, 185
Dunne L., Eales S. A., 2001, MNRAS, 327, 697
Dunne L. et al., 2011, MNRAS, 417, 1510
Dupac X. et al., 2003, A&A, 404, L11
Engelbracht C. W., Rieke G. H., Gordon K. D., Smith J.-D. T., Werner M. W., Moustakas J., Willmer C. N. A., Vanzi L., 2008, ApJ, 678, 804
Finkbeiner D. P., Davis M., Schlegel D. J., 1999, ApJ, 524, 867
Galametz M. et al., 2012, MNRAS, 425, 763
Galametz M. et al., 2009, A&A, 508, 645
Galametz M. et al., 2010, A&A, 518, L55
Galliano F. et al., 2011, A&A, 536, A88
Galliano F., Madden S. C., Jones A. P., Wilson C. D., Bernard J.-P., 2005, A&A, 434, 867
Gil de Paz A., Madore B. F., 2005, ApJS, 156, 345
Gordon K. D. et al., 2010, A&A, 518, L89+
Griffin M. J. et al., 2010, A&A, 518, L3+
Hao C.-N., Kennicutt R. C., Johnson B. D., Calzetti D., Dale D. A., Moustakas J., 2011, ApJ, 741, 124
Hauser M. G., Dwek E., 2001, ARA&A, 39, 249
Haynes M. P. et al., 2011, AJ, 142, 170
Herschel Space Observatory 2013, SPIRE Data Reduction Guide, http://herschel.esac.esa.int/hcss-doc-11.0/print/spire_drg/spir
Hoang T., Draine B. T., Lazarian A., 2010, ApJ, 715, 1462
Hollenbach D., Salpeter E. E., 1971, ApJ, 163, 155
Hughes T. M., Cortese L., Boselli A., Gavazzi G., Davies J. I., 2013, A&A, 550, A115
James A., Dunne L., Eales S., Edmunds M. G., 2002, MNRAS, 335, 753
James F., Roos M., 1975, Computer Physics Communications, 10, 343
Juvela M., Montillaud J., Ysard N., Lunttila T., 2013, A&A, 556, A63
Juvela M., Ysard N., 2012, A&A, 541, A33
Kennicutt R. C. et al., 2011, PASP, 123, 1347
Kewley L. J., Ellison S. L., 2008, ApJ, 681, 1183
Magdis G. E. et al., 2011, ApJL, 740, L15
Magnelli B. et al., 2012, A&A, 548, A22
McKee C. F., Krumholz M. R., 2010, ApJ, 709, 308
Meny C., Gromov V., Boudet N., Bernard J.-P., Paradis D., Nayral C., 2007, A&A, 468, 171
Nilson P., 1973, Nova Acta Regiae Soc. Sci. Upsaliensis Ser. V, p. 0
Ott S., 2010, in Mizumoto Y., Morita K.-I., Ohishi M., eds, Astronomical Society of the Pacific Conference Series Vol. 434, Astronomical Data Analysis Software and Systems XIX. p. 139
Paladini R., Hendrik L., Altieri B., Ali B., 2012, PACS Herschel, https://nhscsci.ipac.caltech.edu/pacs/docs/Photometer/PICC-NHSC
Paradis D. et al., 2010, A&A, 520, L8+
Pettini M., Pagel B. E. J., 2004, MNRAS, 348, L59
Pilbratt G. L. et al., 2010, A&A, 518, L1+
Planck Collaboration et al., 2013, A&A submitted (arXiv:1307.6815)
Planck Collaboration et al., 2011a, A&A, 536, A1
Planck Collaboration et al., 2011b, A&A, 536, A17
Poglitsch A. et al., 2010, A&A, 518, L2+
Rémy-Ruyer A. et al., 2013, A&A, 557, A95
Roseboom I. G. et al., 2013, MNRAS
Roussel H., 2013, PASP, 125, 1126
Sauvage M., Thuan T. X., 1992, ApJL, 396, L69
Schlegel D. J., Finkbeiner D. P., Davis M., 1998, ApJ, 500, 525
Shetty R., Kauffmann J., Schnee S., Goodman A. A., 2009, ApJ, 696, 676
Shetty R., Kauffmann J., Schnee S., Goodman A. A., Ercolano B., 2009, ApJ, 696, 2234
Skibba R. A. et al., 2011, ApJ, 738, 89
Skrutskie M. F. et al., 2006, AJ, 131, 1163
Smith D. J. B. et al., 2013, MNRAS in press (arXiv:1309.4102)

Smith M. W. L. et al., 2012, ApJ, 756, 40
Sodroski T. J., Dwek E., Hauser M. G., Kerr F. J., 1989, ApJ, 336, 762
Springob C. M., Haynes M. P., Giovanelli R., Kent B. R., 2005, ApJS, 160, 149
Stansberry J. A. et al., 2007, PASP, 119, 1038
Steinacker J., Baes M., Gordon K., 2013, ARA&A, 51, 63
Symeonidis M. et al., 2013, MNRAS, 431, 2317
Tabatabaei F. S. et al., 2013, A&A in press (arXiv:1310.4155)
Vlahakis C., Dunne L., Eales S., 2005, MNRAS, 364, 1253
Walterbos R. A. M., Greenawalt B., 1996, ApJ, 460, 696
Werner M. W. et al., 2004, ApJS, 154, 1
Zwicky F., Herzog E., Wild P., 1961, Catalogue of galaxies and of clusters of galaxies. Pasadena: California Institute of Technology (CIT)

Table 1: The PACS 100 and 160μm flux densities of the HRS.

HRS	CGCG	VCC	UGC	NGC	IC	R.A. (J.2000) hh:mm:ss.ss	Dec (J.2000) dd:mm:ss.s	Type	Flag$_{100}$	F$_{100}$ Jy	σ_{100} Jy	Flag$_{160}$	F$_{160}$ Jy	σ_{160} Jy	a arcsec	b arcsec	P.A. degree	Proposal ID
1	123-035	0	0	0	0	10:17:39.66	+22:48:35.9	13	1	0.748	0.169	1	0.932	0.079	48.	40.	-10.	OT1_lcortese_1
2	124-004	0	5588	0	0	10:20:57.13	+25:21:53.4	5	1	2.439	0.227	1	2.808	0.179	47.	45.	40.	OT1_lcortese_1
3	94-026	0	5617	3226	0	10:23:27.01	+19:53:54.7	0	0	0.0	0.0	2	0.846	0.087	39.	39.	15.	GT1_lspinogl_2
4	94-028	0	5620	3227	0	10:23:30.58	+19:51:54.2	3	2	17.589	1.104	2	22.675	1.165	100.	84.	-25.	GT1_lspinogl_2/OT2_aalonsoh_2
5	94-052	0	0	0	610	10:26:28.37	+20:13:41.5	7	1	4.502	0.331	1	5.563	0.528	81.	48.	28.	OT1_lcortese_1
6	154-016	0	5662	0	0	10:27:01.16	+28:38:21.9	5	1	0.275	0.14	1	0.483	0.085	62.	22.	-30.	OT1_lcortese_1
7	154-017	0	5663	3245	0	10:27:18.39	+28:30:26.6	1	1	3.472	0.206	1	2.843	0.151	48.	30.	-3.	OT1_lcortese_1
8	154-020	0	5685	3254	0	10:29:19.92	+29:29:29.2	6	1	2.878	1.092	1	4.641	1.041	210.	66.	46.	OT1_lcortese_1
9	154-026	0	5731	3277	0	10:32:55.45	+28:30:42.2	4	1	1.948	0.397	1	3.037	0.523	82.	73.	25.	OT1_lcortese_1
10	183-028	0	5738	0	0	10:34:29.82	+35:15:24.4	5	1	1.168	0.238	1	0.788	0.094	56.	43.	30.	OT1_lcortese_1
11	124-038	0	5742	3287	0	10:34:47.31	+21:38:54.0	9	1	5.192	0.3	1	6.148	0.409	88.	41.	20.	OT1_lcortese_1
12	124-041	0	0	0	0	10:35:42.07	+26:07:33.7	17	1	0.613	0.054	1	0.492	0.05	29.	22.	20.	OT1_lcortese_1
13	183-030	0	5753	3294	0	10:36:16.25	+37:19:28.9	7	1	19.809	1.322	1	25.224	1.717	149.	76.	-65.	OT1_lcortese_1
14	124-045	0	5767	3301	0	10:36:56.04	+21:52:55.7	2	1	0.477	0.078	1	0.372	0.106	35.	35.	55.	OT1_lcortese_1
15	65-087	0	5826	3338	0	10:42:07.54	+13:44:49.2	7	1	13.12	2.907	1	20.386	2.277	247.	152.	-80.	OT1_lcortese_1
16	94-116	0	5842	3346	0	10:43:38.91	+14:52:18.7	8	1	5.688	0.695	1	10.294	0.785	113.	98.	-72.	OT1_lcortese_1
17	95-019	0	5887	3370	0	10:47:04.05	+17:16:25.3	7	1	10.209	0.872	1	12.793	0.832	133.	75.	-30.	OT1_lcortese_1
18	155-015	0	5906	3380	0	10:48:12.17	+28:36:06.5	3	1	1.465	0.248	1	2.015	0.241	71.	57.	20.	OT1_lcortese_1
19	184-016	0	5909	3381	0	10:48:24.82	+34:42:41.1	13	1	4.335	0.525	1	4.371	0.375	86.	78.	55.	OT1_lcortese_1
20	184-018	0	5931	3395	2613	10:49:50.11	+32:58:58.3	8	2	16.137	1.402	2	16.068	0.871	84.	63.	50.	KPGT_esturm_1
21	155-028	0	5958	0	0	10:51:15.81	+27:50:54.9	6	1	0.625	0.255	1	1.084	0.148	78.	45.	0.	OT1_lcortese_1
22	155-029	0	5959	3414	0	10:51:16.23	+27:58:30.0	1	1	0.618	0.072	1	0.685	0.118	40.	36.	10.	OT1_lcortese_1
23	184-028	0	5972	3424	0	10:51:46.33	+32:54:02.7	5	1	18.098	0.981	1	19.636	1.076	109.	59.	-70.	OT1_lcortese_1
24	184-029	0	5982	3430	0	10:52:11.41	+32:57:01.5	7	1	10.909	1.182	1	16.037	1.577	167.	94.	35.	OT1_lcortese_1
25	125-013	0	5995	3437	0	10:52:35.75	+22:56:02.9	7	1	21.647	1.187	1	21.174	1.142	101.	67.	-63.	OT1_lcortese_1
26	184-031	0	5990	0	0	10:52:38.34	+34:28:59.3	4	1	0.744	0.098	1	0.864	0.106	58.	35.	15.	OT1_lcortese_1
27	184-034	0	6001	3442	0	10:53:08.11	+33:54:37.3	3	1	3.148	0.286	1	3.173	0.253	56.	48.	-2.	OT1_lcortese_1
28	155-035	0	6023	3451	0	10:54:20.86	+27:14:22.9	9	1	3.569	0.232	1	5.184	0.321	80.	48.	50.	OT1_lcortese_1
29	95-060	0	6026	3454	0	10:54:29.45	+17:20:38.3	7	1	2.403	0.292	1	3.422	0.326	90.	51.	-65.	OT1_lcortese_1
30	95-062	0	6028	3455	0	10:54:31.07	+17:17:04.7	5	1	2.87	0.545	1	3.859	0.37	100.	62.	70.	OT1_lcortese_1
31	267-027	0	6024	3448	0	10:54:39.24	+54:18:18.8	13	1	12.17	1.183	1	10.63	1.579	236.	75.	65.	OT1_lcortese_1
32	95-065	0	6030	3457	0	10:54:48.63	+17:37:16.3	5	1	0.042	0.024	1	0.182	0.034	20.	20.	90.	OT1_lcortese_1
33	95-085	0	6077	3485	0	11:00:02.38	+14:50:29.7	5	1	5.138	0.368	1	6.83	0.532	88.	77.	60.	OT1_lcortese_1
34	95-097	0	6116	3501	0	11:02:47.32	+17:59:22.2	8	1	5.002	0.64	1	8.619	0.832	167.	52.	30.	OT1_lcortese_1
35	267-037	0	6115	3499	0	11:03:11.03	+56:13:18.2	13	1	0.24	0.057	1	0.273	0.081	34.	30.	20.	OT1_lcortese_1
36	155-049	0	6118	3504	0	11:03:11.21	+27:58:21.0	4	1	35.557	1.977	1	31.358	1.651	113.	88.	-30.	OT1_lcortese_1
37	155-051	0	6128	3512	0	11:04:02.98	+28:02:12.5	7	1	4.532	0.346	1	5.328	0.513	68.	63.	-42.	OT1_lcortese_1
38	38-129	0	6167	3526	0	11:06:56.63	+07:10:26.1	7	1	1.818	0.291	1	1.886	0.286	83.	45.	55.	OT1_lcortese_1
39	66-115	0	6169	0	0	11:07:03.35	+12:03:36.2	5	1	0.915	0.21	1	1.199	0.333	81.	39.	0.	OT1_lcortese_1
40	67-019	0	6209	3547	0	11:09:55.94	+10:43:15.0	5	1	4.478	0.305	1	4.51	0.363	80.	39.	7.	OT1_lcortese_1
41	96-011	0	6267	3592	0	11:14:27.25	+17:15:36.5	7	1	1.418	0.278	1	1.584	0.144	74.	41.	-63.	OT1_lcortese_1
42	96-013	0	6277	3596	0	11:15:06.21	+14:47:13.5	7	1	12.111	2.072	1	18.583	1.787	171.	163.	0.	OT1_lcortese_1
43	96-022	0	6299	3608	0	11:16:58.96	+18:08:54.9	0	0	0.119	0.0	0	0.187	0.0	28.	28.	0.	OT1_lcortese_1
44	96-026	0	6320	0	0	11:18:17.24	+18:50:49.0	5	1	2.521	0.197	1	1.982	0.208	54.	51.	-73.	OT1_lcortese_1
45	291-054	0	6330	3619	0	11:19:21.60	+57:45:27.8	1	1	1.782	0.393	1	2.72	0.439	78.	75.	-65.	OT1_lcortese_1
46	96-029	0	6343	3626	0	11:20:03.80	+18:21:24.5	1	1	4.995	0.272	1	4.9	0.284	59.	54.	-20.	OT1_acrocker_1
47	156-064	0	6352	3629	0	11:20:31.82	+26:57:48.2	8	1	2.652	0.465	1	3.163	0.509	96.	68.	65.	OT1_lcortese_1
48	268-021	0	6360	3631	0	11:21:02.85	+53:10:11.0	7	1	29.87	3.057	1	38.272	3.115	210.	201.	-62.	OT1_lcortese_1
49	39-130	0	6368	3640	0	11:21:06.85	+03:14:05.4	0	0	0.261	0.0	0	0.231	0.0	35.	35.	90.	OT1_lcortese_1
50	96-037	0	6396	3655	0	11:22:54.62	+16:35:24.5	7	1	20.97	1.076	1	22.078	1.141	76.	53.	30.	OT1_lcortese_1
51	96-038	0	6405	3659	0	11:23:45.49	+17:49:06.8	11	1	4.542	0.423	1	4.996	0.582	87.	62.	55.	OT1_lcortese_1
52	268-030	0	6406	3657	0	11:23:55.57	+52:55:15.5	7	1	0.783	0.274	1	1.305	0.237	61.	54.	-20.	OT1_lcortese_1
53	67-071	0	6420	3666	0	11:24:26.07	+11:20:32.0	7	1	8.762	0.75	1	10.815	0.829	184.	50.	-85.	OT1_lcortese_1
54	96-045	0	6445	3681	0	11:26:29.80	+16:51:47.5	6	1	2.819	0.577	1	3.076	0.537	94.	75.	-15.	OT1_lcortese_1
55	96-047	0	6453	3684	0	11:27:11.18	+17:01:49.0	6	1	7.742	0.768	1	11.416	0.769	121.	84.	-55.	OT1_lcortese_1
56	291-072	0	6458	3683	0	11:27:31.85	+56:52:37.4	7	1	28.93	1.498	1	30.107	1.604	82.	65.	-52.	OT1_lcortese_1
57	96-049	0	6460	3686	0	11:27:43.95	+17:13:26.8	6	1	12.431	1.106	1	17.983	1.255	134.	104.	25.	OT1_lcortese_1
58	96-050	0	6464	3691	0	11:28:09.41	+16:55:13.7	5	1	2.098	0.194	1	2.449	0.155	53.	42.	30.	OT1_lcortese_1
59	67-084	0	6474	3692	0	11:28:24.01	+09:24:27.5	5	1	3.801	0.395	1	5.622	0.431	132.	48.	-85.	OT1_lcortese_1
60	268-051	0	6547	3729	0	11:33:49.34	+53:07:31.8	3	1	7.738	0.915	1	10.477	0.772	118.	80.	15.	OT1_lcortese_1
61	292-009	0	6575	0	0	11:36:26.47	+58:11:29.0	8	1	0.7	0.121	1	0.937	0.15	83.	25.	-9.	OT1_lcortese_1
62	186-012	0	6577	3755	0	11:36:33.37	+36:24:37.2	7	1	2.73	0.498	1	3.527	0.528	133.	58.	-65.	OT1_lcortese_1
63	268-063	0	6579	3756	0	11:36:48.02	+54:17:36.8	6	1	6.471	1.15	1	12.252	1.339	175.	88.	-1.	OT1_lcortese_1
64	292-017	0	6629	3795	0	11:40:06.84	+58:36:47.2	7	1	1.333	0.326	1	1.682	0.29	92.	48.	53.	OT1_lcortese_1
65	292-019	0	6640	3794	0	11:40:53.42	+56:12:07.3	9	1	1.909	0.476	1	2.082	0.426	94.	61.	-60.	OT1_lcortese_1
66	186-024	0	6651	3813	0	11:41:18.65	+36:32:48.3	5	1	21.54	1.151	1	23.821	1.255	94.	46.	85.	OT1_lcortese_1
67	268-076	0	6706	0	0	11:44:14.83	+55:02:05.9	11	1	0.841	0.181	1	1.209	0.279	67.	45.	60.	OT1_lcortese_1
68	186-045	0	0	0	0	11:46:25.96	+34:51:09.2	5	1	1.518	0.1	1	1.531	0.092	40.	40.	0.	OT1_lcortese_1
69	268-088	0	6787	3898	0	11:49:15.37	+56:05:03.7	4	1	3.46	1.115	1	4.318	1.203	184.	108.	-72.	OT1_lcortese_1
70	0	0	0	0	2969	11:52:31.27	-03:52:20.1	6	1	1.605	0.2	1	2.018	0.161	61.	51.	-75.	OT1_lcortese_1
71	292-042	0	6860	3945	0	11:53:13.73	+60:40:32.0	1	1	1.567	0.957	1	4.253	0.685	170.	112.	-15.	OT1_acrocker_1
72	0	0	0	3952	2972	11:53:40.63	-03:59:47.5	12	1	2.403	0.261	1	1.972	0.308	81.	48.	79.	OT1_lcortese_1
73	269-013	0	6870	3953	0	11:53:48.92	+52:19:36.4	6	1	28.168	2.638	1	49.52	4.004	243.	129.	13.	OT1_lcortese_1
74	269-019	0	6918	3982	0	11:56:28.10	+55:07:30.6	5	1	16.493	1.023	1	17.392	0.978	98.	86.	38.	OT1_lcortese_1
75	269-020	0	6919	0	0	11:56:37.51	+55:37:59.5	10	1	0.148	0.071	1	0.37	0.062	30.	24.	90.	OT1_lcortese_1
76	269-022	0	6923	0	0	11:56:49.43	+53:09:37.3	12	1	0.886	0.176	1	0.909	0.172	84.	35.	-10.	OT1_lcortese_1
77	13-033	0	6993	4030	0	12:00:23.64	-01:06:00.0	6	1	58.47	3.251	1	73.761	4.064	175.	127.	31.	OT1_lcortese_1

Continued on the next page...

Table 1 – Continued.

HRS	CGCG	VCC	UGC	NGC	IC	R.A. (J.2000) hh:mm:ss.ss	Dec (J.2000) dd:mm:ss.s	Type	$Flag_{100}$	F_{100} Jy	σ_{100} Jy	$Flag_{160}$	F_{160} Jy	σ_{160} Jy	a arcsec	b arcsec	P.A. degree	Proposal ID
78	98-019	0	6995	4032	0	12:00:32.82	+20:04:26.0	12	1	2.04	0.223	1	2.802	0.442	78.	76.	-4.	OT1_lcortese_1
79	69-024	0	7001	4019	755	12:01:10.39	+14:06:16.2	5	1	0.986	0.192	1	1.583	0.428	108.	52.	-35.	OT1_lcortese_1
80	69-027	0	7002	4037	0	12:01:23.67	+13:24:03.7	5	1	1.479	0.57	1	2.875	0.68	105.	86.	15.	OT1_lcortese_1
81	13-046	0	7021	4045	0	12:02:42.26	+01:58:36.4	3	1	15.308	0.97	1	17.08	1.267	126.	93.	5.	OT1_lcortese_1
82	98-037	0	0	0	0	12:03:35.94	+16:03:20.0	4	1	1.89	0.293	1	1.683	0.158	58.	54.	-75.	OT1_lcortese_1
83	41-031	0	7035	0	0	12:03:40.14	+02:38:28.4	3	1	0.674	0.137	1	0.48	0.109	47.	45.	-30.	OT1_lcortese_1
84	69-036	0	7048	4067	0	12:04:11.55	+10:51:15.8	5	1	1.791	0.191	1	2.595	0.179	50.	37.	45.	OT1_lcortese_1
85	243-044	0	7095	4100	0	12:06:08.60	+49:34:56.3	6	1	23.375	2.26	1	30.458	1.966	226.	75.	-17.	OT1_lcortese_1
86	41-041	0	7111	4116	0	12:07:36.82	+02:41:32.0	10	1	6.575	1.5	1	9.4	1.357	160.	101.	-17.	OT1_lcortese_1
87	69-058	0	7117	4124	0	12:08:09.64	+10:22:43.4	1	1	1.703	0.293	1	1.831	0.266	68.	51.	-30.	OT1_lcortese_1
88	41-042	0	7116	4123	0	12:08:11.11	+02:52:41.8	7	1	12.906	2.2	1	14.472	2.443	210.	163.	-75.	OT1_lcortese_1
89	69-088	66	7215	4178	0	12:12:46.45	+10:51:57.5	10	1	10.83	1.126	1	15.005	1.774	225.	79.	30.	OT1_lcortese_1
90	13-104	0	7214	4179	0	12:12:52.11	+01:17:58.9	1	0	1.653	0.0	0	2.248	0.0	91.	91.	0.	OT1_lcortese_1
91	98-108	92	7231	4192	0	12:13:48.29	+14:54:01.2	4	1	28.035	2.497	1	45.141	2.893	411.	109.	-25.	KPOT_jdavie01
92	69-101	131	7255	0	3061	12:15:04.44	+14:01:44.3	7	1	1.686	0.23	1	2.382	0.199	102.	51.	-60.	KPOT_jdavie01
93	187-029	0	7256	4203	0	12:15:05.06	+33:11:50.4	1	1	2.028	0.348	1	2.87	0.42	104.	85.	0.	OT1_acrocker_1
94	69-104	145	7260	4206	0	12:15:16.81	+13:01:26.3	6	1	3.312	0.404	1	5.238	0.536	206.	51.	0.	KPOT_jdavie01
95	69-107	152	7268	4207	0	12:15:30.50	+09:35:05.6	8	1	7.801	0.45	1	8.137	0.444	82.	37.	-60.	OT1_lcortese_1
96	69-110	157	7275	4212	0	12:15:39.36	+13:54:05.4	7	1	20.43	1.226	1	25.125	1.338	151.	84.	75.	KPOT_jdavie01
97	69-112	167	7284	4216	0	12:15:54.44	+13:08:57.8	5	1	18.247	1.559	1	33.198	2.559	383.	91.	19.	KPOT_jdavie01
98	69-119	187	7291	4222	0	12:16:22.52	+13:18:25.5	7	1	3.222	0.323	1	5.373	0.362	144.	47.	55.	KPOT_jdavie01
99	69-123	213	7305	0	3094	12:16:56.00	+13:37:31.0	5	1	1.077	0.067	1	1.304	0.079	39.	30.	-88.	KPOT_jdavie01
100	98-130	226	7315	4237	0	12:17:11.42	+15:19:26.3	6	1	10.131	0.529	1	14.106	0.736	84.	49.	-75.	KPOT_jdavie01
101	158-060	0	7338	4251	0	12:18:08.31	+28:10:31.1	1	0	1.447	0.0	0	1.831	0.0	87.	87.	0.	OT1_lcortese_1
102	98-144	307	7345	4254	0	12:18:49.63	+14:24:59.4	7	1	111.145	6.099	1	141.58	7.52	258.	235.	60.	KPOT_jdavie01
103	42-015	341	7361	4260	0	12:19:22.24	+06:05:55.2	3	1	0.859	0.125	1	1.039	0.113	68.	36.	45.	KPOT_jdavie01
104	99-015	0	7366	0	0	12:19:28.66	+17:13:49.4	5	0	0.544	0.0	0	0.385	0.0	50.	50.	0.	OT1_lcortese_1
105	99-014	355	7365	4262	0	12:19:30.58	+14:52:39.8	1	0	0.283	0.0	0	0.256	0.0	44.	44.	0.	KPOT_jdavie01
106	42-032	393	7385	4276	0	12:20:07.50	+07:41:31.2	7	1	2.069	0.504	1	2.238	0.466	88.	88.	3.	OT1_lcortese_1
107	42-033	404	7387	0	0	12:20:17.35	+04:12:05.1	9	1	1.021	0.143	1	1.499	0.115	81.	39.	15.	KPOT_jdavie01
108	42-037	434	0	4287	0	12:20:48.49	+05:38:23.5	7	1	1.011	0.167	1	1.313	0.132	77.	34.	70.	KPOT_jdavie01
109	42-038	449	7403	4289	0	12:21:02.25	+03:43:19.7	8	1	2.676	0.347	1	3.376	0.391	181.	37.	1.	KPOT_jdavie01
110	70-024	465	7407	4294	0	12:21:17.79	+11:30:40.0	8	1	6.137	0.495	1	7.821	0.501	166.	52.	-20.	KPOT_jdavie01
111	99-024	483	7412	4298	0	12:21:32.76	+14:36:22.2	7	1	14.297	0.758	1	22.151	1.142	101.	75.	-40.	KPOT_jdavie01
112	42-044	492	7413	4300	0	12:21:41.47	+05:23:05.4	3	1	1.059	0.149	1	1.002	0.139	91.	30.	40.	KPOT_jdavie01
113	99-027	497	7418	4302	0	12:21:42.48	+14:35:53.9	7	1	17.551	1.098	1	30.598	1.62	271.	59.	-3.	KPOT_jdavie01
114	42-045	508	7420	4303	0	12:21:54.90	+04:28:25.1	6	1	102.907	5.799	1	118.6	6.85	277.	225.	-18.	KPOT_jdavie01
115	42-047	517	7422	0	0	12:22:01.30	+05:06:00.2	4	1	1.012	0.095	1	1.014	0.086	57.	36.	-10.	KPOT_jdavie01
116	70-031	522	7432	4305	0	12:22:03.60	+12:44:27.3	3	0	1.045	0.0	0	1.366	0.0	109.	109.	0.	KPOT_jdavie01
117	70-029	524	7431	4307	0	12:22:05.63	+09:02:36.8	5	1	4.524	0.534	1	7.711	0.477	161.	47.	25.	KPOT_jdavie01
118	42-053	552	7439	0	0	12:22:27.25	+04:33:58.7	8	1	1.385	0.287	1	1.611	0.269	79.	60.	-10.	KPOT_jdavie01
119	99-029	559	7442	4312	0	12:22:31.36	+15:32:16.5	4	1	6.626	0.487	1	8.675	0.606	214.	52.	-10.	KPOT_jdavie01
120	70-034	570	7445	4313	0	12:22:38.55	+11:48:03.4	4	1	4.293	0.454	1	7.038	0.533	214.	49.	-37.	KPOT_jdavie01
121	70-035	576	7447	4316	0	12:22:42.24	+09:19:56.9	6	1	5.544	0.322	1	8.633	0.506	107.	46.	-70.	KPOT_jdavie01
122	99-030	596	7450	4321	0	12:22:54.90	+15:49:20.6	6	1	87.905	6.335	1	123.549	7.21	330.	293.	30.	KPOT_rkennicu_1
123	42-063	613	7451	4324	0	12:23:06.18	+05:15:01.5	1	1	1.473	0.397	1	2.938	0.336	148.	42.	53.	KPOT_jdavie01
124	70-039	630	7456	4330	0	12:23:17.25	+11:22:04.7	8	1	3.122	0.66	1	6.081	0.82	246.	61.	64.	KPOT_jdavie01
125	42-068	648	7461	4339	0	12:23:34.94	+06:04:54.2	0	0	0.111	0.0	0	0.109	0.0	22.	22.	0.	KPOT_jdavie01
126	99-036	654	7467	4340	0	12:23:35.31	+16:43:19.9	1	0	0.957	0.0	0	1.896	0.0	86.	86.	0.	OT1_lcortese_1
127	42-070	656	7465	4343	0	12:23:38.70	+06:57:14.7	5	1	4.339	0.267	1	6.305	0.35	109.	44.	-50.	KPOT_jdavie01
128	42-072	667	7469	0	3259	12:23:48.52	+07:11:12.6	10	1	0.595	0.115	1	1.331	0.109	79.	39.	15.	KPOT_jdavie01
129	99-038	685	7473	4350	0	12:23:57.81	+16:41:36.1	1	1	0.853	0.114	1	0.502	0.123	40.	40.	-0.	OT1_lcortese_1
130	70-045	692	7476	4351	0	12:24:01.56	+12:12:18.1	4	1	2.01	0.309	1	2.918	0.29	84.	62.	70.	KPOT_jdavie01
131	42-079	697	7474	0	3267	12:24:05.53	+07:02:28.6	8	1	0.552	0.19	1	1.263	0.136	65.	65.	30.	KPOT_jdavie01
132	42-080	699	7477	0	3268	12:24:07.44	+06:36:26.9	13	1	1.695	0.259	1	1.396	0.158	82.	58.	22.	KPOT_jdavie01
133	158-099	0	7483	4359	0	12:24:11.06	+31:31:17.8	7	1	1.661	0.504	1	2.545	0.371	150.	49.	-75.	OT1_lcortese_1
134	70-048	713	7482	4356	0	12:24:14.53	+08:32:08.9	7	1	1.602	0.289	1	2.763	0.274	136.	36.	40.	KPOT_jdavie01
135	42-083	731	7488	4365	0	12:24:28.23	+07:19:03.1	0	0	0.703	0.0	0	0.434	0.0	78.	78.	0.	KPOT_jdavie01
136	42-089	758	7492	4370	0	12:24:54.93	+07:26:40.4	3	1	3.107	0.198	1	3.891	0.22	74.	37.	80.	KPOT_jdavie01
137	70-057	759	7493	4371	0	12:24:55.43	+11:42:15.4	1	0	2.143	0.0	0	2.027	0.0	122.	122.	0.	KPOT_jdavie01
138	70-058	763	7494	4374	0	12:25:03.78	+12:53:13.1	0	1	1.014	0.074	1	0.896	0.067	40.	39.	90.	KPOT_jdavie01
139	42-093	787	7498	4376	0	12:25:18.06	+05:44:28.3	12	1	1.801	0.195	1	2.078	0.25	77.	45.	-45.	KPOT_jdavie01
140	42-092	785	7497	4378	0	12:25:18.09	+04:55:30.2	3	1	1.92	0.534	1	3.115	0.833	129.	104.	-20.	KPOT_jdavie01
141	70-061	792	7503	4380	0	12:25:22.17	+10:01:00.5	5	1	3.723	0.391	1	7.037	0.498	148.	74.	-25.	KPOT_jdavie01
142	99-044	801	7507	4383	0	12:25:25.50	+16:28:12.0	3	1	12.722	0.736	1	11.722	0.674	109.	54.	20.	OT1_lcortese_1
143	42-095	827	7513	0	0	12:25:42.63	+07:13:00.1	8	1	5.804	0.429	1	8.478	0.449	157.	44.	-25.	KPOT_jdavie01
144	70-068	836	7520	4388	0	12:25:46.82	+12:39:43.5	5	1	18.998	1.033	1	19.916	1.193	214.	52.	90.	KPOT_jdavie01
145	70-067	849	7519	4390	0	12:25:50.67	+10:27:32.6	6	1	2.168	0.348	1	3.319	0.346	92.	76.	-55.	KPOT_jdavie01
146	42-098	851	7518	0	3322	12:25:54.12	+07:33:17.4	8	1	2.383	0.221	1	2.886	0.191	91.	39.	-20.	KPOT_jdavie01
147	42-099	859	7522	0	0	12:25:58.30	+03:25:47.3	9	1	2.257	0.363	1	3.973	0.552	121.	41.	-50.	OT1_lcortese_1
148	99-049	865	7526	4396	0	12:25:58.80	+15:40:17.3	9	1	3.96	0.53	1	6.539	0.826	142.	58.	-55.	OT1_lcortese_1
149	70-071	873	7528	4402	0	12:26:07.56	+13:06:46.0	5	1	18.263	0.974	1	26.98	1.385	166.	49.	90.	KPOT_jdavie01
150	70-072	881	7532	4406	0	12:26:11.74	+12:56:46.4	0	0	2.154	0.0	1	0.579	0.356	130.	114.	-50.	KPOT_jdavie01
151	70-076	912	7538	4413	0	12:26:32.25	+12:36:39.5	4	1	3.781	0.552	1	4.395	0.543	123.	74.	15.	KPOT_jdavie01
152	42-104	921	7536	4412	0	12:26:36.10	+03:57:52.7	5	1	6.307	0.405	1	6.358	0.416	79.	66.	76.	OT1_lcortese_1
153	42-105	938	7541	4416	0	12:26:46.72	+07:55:08.4	8	1	3.24	0.376	1	4.547	0.465	91.	85.	-35.	KPOT_jdavie01
154	70-082	939	7546	0	0	12:26:47.23	+08:53:04.6	8	1	2.224	0.417	1	2.702	0.448	103.	98.	-15.	KPOT_jdavie01
155	70-080	944	7542	4417	0	12:26:50.62	+09:35:03.0	1	0	0.704	0.0	0	0.545	0.0	86.	86.	0.	KPOT_jdavie01

Continued on the next page...

Table 1 – Continued.

HRS	CGCG	VCC	UGC	NGC	IC	R.A. (J.2000) hh:mm:ss.ss	Dec (J.2000) dd:mm:ss.s	Type	$Flag_{100}$	F_{100} Jy	σ_{100} Jy	$Flag_{160}$	F_{160} Jy	σ_{160} Jy	a arcsec	b arcsec	P.A. degree	Proposal ID
156	99-054	958	7551	4419	0	12:26:56.43	+15:02:50.7	3	1	17.548	1.121	1	18.421	0.992	148.	58.	-47.	OT1_lcortese_1
157	42-106	957	7549	4420	0	12:26:58.48	+02:29:39.7	6	1	7.145	0.436	1	9.352	0.608	86.	51.	8.	OT1_lcortese_1
158	42-107	971	7556	4423	0	12:27:08.97	+05:52:48.6	10	1	0.928	0.178	1	1.4	0.347	107.	42.	20.	OT1_lcortese_1
159	70-090	979	7561	4424	0	12:27:11.59	+09:25:14.0	3	1	6.7	0.438	1	6.132	0.381	85.	80.	-80.	KPOT_jdavie01
160	42-111	1002	7566	4430	0	12:27:26.41	+06:15:46.0	5	1	4.205	0.583	1	7.142	0.79	94.	90.	-60.	OT1_lcortese_1
161	70-093	1003	7568	4429	0	12:27:26.56	+11:06:27.1	1	1	4.848	1.025	1	5.509	0.593	169.	78.	-81.	KPOT_jdavie01
162	70-098	1030	7575	4435	0	12:27:40.49	+13:04:44.2	1	1	4.72	0.304	1	4.484	0.302	83.	77.	10.	KPOT_jdavie01
163	70-097	1043	7574	4438	0	12:27:45.59	+13:00:31.8	5	1	11.949	0.863	1	15.454	1.09	134.	118.	27.	KPOT_jdavie01
164	70-099	1047	7581	4440	0	12:27:53.57	+12:17:35.6	3	0	0.992	0.0	0	0.972	0.0	84.	84.	0.	KPOT_jdavie01
165	42-117	1048	7579	0	0	12:27:55.39	+05:43:16.4	10	1	0.905	0.208	1	1.342	0.223	78.	36.	-50.	OT1_lcortese_1
166	70-100	1062	7583	4442	0	12:28:03.89	+09:48:13.0	1	0	1.685	0.0	0	1.393	0.0	121.	121.	0.	KPOT_jdavie01
167	70-104	1086	7587	4445	0	12:28:15.94	+09:26:10.7	4	1	1.215	0.139	1	2.378	0.181	93.	33.	-75.	KPOT_jdavie01
168	70-108	1091	7590	0	0	12:28:18.77	+08:43:46.1	6	1	0.935	0.088	1	0.916	0.12	58.	37.	-5.	KPOT_jdavie01
169	99-063	0	7595	0	3391	12:28:27.28	+18:24:55.1	8	1	1.39	0.212	1	2.187	0.32	64.	50.	-85.	OT1_lcortese_1
170	99-062	1110	7594	4450	0	12:28:29.63	+17:05:05.8	4	1	9.713	3.046	1	14.263	3.336	258.	170.	-9.	OT1_lcortese_1
171	70-111	1118	7600	4451	0	12:28:40.55	+09:15:32.2	6	1	4.509	0.257	1	4.894	0.269	82.	41.	-10.	KPOT_jdavie01
172	99-065	1126	7602	0	3392	12:28:43.26	+14:59:58.2	5	1	4.083	0.632	1	5.039	0.426	123.	49.	40.	OT1_lcortese_1
173	42-124	1145	7609	4457	0	12:28:59.01	+03:34:14.2	5	1	10.527	0.664	1	10.627	0.834	95.	95.	-15.	OT1_lcortese_1
174	70-116	1154	7614	4459	0	12:29:00.03	+13:58:42.9	1	1	4.355	0.25	1	4.049	0.226	40.	40.	0.	OT1_lcortese_1
175	70-115	1158	7613	4461	0	12:29:03.01	+13:11:01.5	1	0	1.165	0.0	0	0.869	0.0	84.	84.	0.	KPOT_jdavie01
176	70-121	1190	7622	4469	0	12:29:28.03	+08:44:59.7	2	1	3.158	0.282	1	4.171	0.323	85.	48.	85.	KPOT_jdavie01
177	42-132	1205	7627	4470	0	12:29:37.78	+07:49:27.1	3	1	4.592	0.246	1	4.981	0.308	77.	48.	0.	KPOT_jdavie01
178	42-134	1226	7629	4472	0	12:29:46.76	+08:00:01.7	0	0	1.317	0.0	0	1.438	0.0	92.	92.	0.	KPOT_jdavie01
179	70-125	1231	7631	4473	0	12:29:48.87	+13:25:45.7	0	0	0.214	0.0	0	0.179	0.0	36.	36.	0.	KPOT_jdavie01
180	70-129	1253	7638	4477	0	12:30:02.17	+13:38:11.2	1	1	1.221	0.101	1	1.285	0.127	56.	44.	35.	KPOT_jdavie01
181	70-133	1279	7645	4478	0	12:30:17.42	+12:19:42.8	0	0	0.127	0.0	0	0.115	0.0	22.	22.	0.	KPOT_jdavie01
182	42-139	1290	7647	4480	0	12:30:26.78	+04:14:47.3	7	1	4.369	0.319	1	5.391	0.353	84.	60.	-10.	OT1_lcortese_1
183	70-139	1316	7654	4486	0	12:30:49.42	+12:23:28.0	0	1	0.693	0.182	1	0.82	0.156	58.	57.	-21.	KPOT_jdavie01
184	70-140	1326	7657	4491	0	12:30:57.13	+11:29:00.8	3	1	2.644	0.217	1	2.265	0.196	79.	39.	-32.	KPOT_jdavie01
185	42-141	1330	7656	4492	0	12:30:59.74	+08:04:40.6	3	1	1.181	0.276	1	1.979	0.283	82.	82.	75.	KPOT_jdavie01
186	129-005	0	7662	4494	0	12:31:24.03	+25:46:29.9	0	1	0.37	0.037	1	0.313	0.046	26.	26.	0.	OT1_lcortese_1
187	42-144	1375	7668	4505	0	12:31:39.21	+03:56:22.1	11	2	12.509	2.008	2	15.141	3.227	200.	158.	70.	OT1_lcortese_1
188	99-075	1379	7669	4498	0	12:31:39.57	+16:51:10.1	9	1	4.308	0.549	1	6.629	0.617	120.	64.	-55.	OT1_lcortese_1
189	99-077	1393	7676	0	797	12:31:54.76	+15:07:26.2	7	1	2.238	0.304	1	2.67	0.262	71.	47.	-72.	OT1_lcortese_1
190	99-076	1401	7675	4501	0	12:31:59.22	+14:25:13.5	5	1	74.118	5.57	1	104.85	5.821	304.	162.	-40.	OT1_lcortese_1
191	99-078	1410	7677	4502	0	12:32:03.35	+16:41:15.8	8	1	0.633	0.163	1	0.854	0.212	62.	33.	40.	OT1_lcortese_1
192	70-152	1419	7682	4506	0	12:32:10.53	+13:25:10.6	3	1	0.403	0.049	1	0.583	0.062	36.	29.	-75.	KPOT_jdavie01
193	70-157	1450	7695	0	3476	12:32:41.88	+14:03:01.8	12	1	3.138	0.314	1	3.928	0.363	95.	73.	30.	KPOT_jdavie01
194	14-063	0	7694	4517	0	12:32:45.59	+00:06:54.1	8	1	28.254	1.875	1	48.955	2.661	462.	86.	80.	OT2_emurph01
195	99-087	1479	7703	4516	0	12:33:07.56	+14:34:29.8	4	0	1.184	0.0	0	1.282	0.0	90.	90.	0.	OT1_lcortese_1
196	70-167	1508	7709	4519	0	12:33:30.25	+08:39:17.1	9	1	8.617	0.893	1	10.184	0.763	151.	109.	-28.	KPOT_jdavie01
197	70-168	1516	7711	4522	0	12:33:39.66	+09:10:29.5	8	1	4.664	0.381	1	6.095	0.44	170.	42.	33.	KPOT_jdavie01
198	159-016	0	7714	4525	0	12:33:51.19	+30:16:39.1	8	1	1.015	0.487	1	2.011	0.377	126.	67.	65.	OT1_lcortese_1
199	99-090	1532	7716	0	800	12:33:56.66	+15:21:17.4	7	1	1.256	0.546	1	1.533	0.226	82.	60.	-30.	OT1_lcortese_1
200	42-155	1535	7718	4526	0	12:34:03.03	+07:41:56.9	1	1	15.632	0.827	1	17.282	0.88	71.	68.	-17.	KPOT_jdavie01
201	42-156	1540	7721	4527	0	12:34:08.50	+02:39:13.7	6	1	75.281	3.999	1	93.527	4.864	246.	79.	67.	OT1_lcortese_1
202	70-173	1549	7728	0	3510	12:34:14.79	+11:04:17.7	-2	0	0.116	0.0	0	0.114	0.0	22.	22.	0.	KPOT_jdavie01
203	42-158	1554	7726	4532	0	12:34:19.33	+06:28:03.7	12	1	15.489	0.835	1	15.638	0.953	112.	51.	-14.	OT1_lcortese_1
204	42-159	1555	7727	4535	0	12:34:20.31	+08:11:51.9	7	1	34.851	3.113	1	61.656	3.907	270.	232.	0.	KPOT_jdavie01
205	14-068	1562	7732	4536	0	12:34:27.13	+02:11:16.4	6	1	56.393	3.262	1	58.539	3.082	304.	138.	-40.	KPOT_rkennicu_1
206	42-162	1575	7736	0	3521	12:34:39.42	+07:09:36.0	15	1	2.733	0.481	1	3.017	0.367	84.	59.	18.	OT1_lcortese_1
207	99-093	1588	7742	4540	0	12:34:50.87	+15:33:05.2	8	1	5.468	0.398	1	6.779	0.528	79.	67.	-35.	OT1_lcortese_1
208	99-096	1615	7753	4548	0	12:35:26.43	+14:29:46.8	5	1	13.601	5.576	1	24.022	3.148	252.	210.	-30.	OT1_lcortese_1
209	0	0	0	4546	0	12:35:29.51	-03:47:35.5	1	1	0.513	0.132	1	0.632	0.121	57.	37.	80.	OT1_lcortese_1
210	70-182	1619	7757	4550	0	12:35:30.61	+12:13:15.4	1	1	0.516	0.096	1	0.486	0.125	83.	23.	-2.	KPOT_jdavie01
211	70-184	1632	7760	4552	0	12:35:39.88	+12:33:21.7	0	0	0.724	0.0	0	0.498	0.0	65.	65.	0.	KPOT_jdavie01
212	99-098	0	7768	4561	0	12:36:08.14	+19:19:21.4	10	1	2.505	0.299	1	2.426	0.293	77.	63.	-70.	OT1_lcortese_1
213	129-010	0	7772	4565	0	12:36:20.78	+25:59:15.6	5	1	55.365	4.659	1	90.833	5.143	596.	80.	-45.	OT1_lcortese_1
214	70-186	1664	7773	4564	0	12:36:26.99	+11:26:21.5	0	0	0.291	0.0	0	0.268	0.0	38.	38.	0.	KPOT_jdavie01
215	70-189	1673	7777	4567	0	12:36:32.71	+11:15:28.8	6	2	14.15	0.743	2	19.184	0.976	87.	41.	75.	KPOT_jdavie01
216	70-188	1676	7776	4568	0	12:36:34.26	+11:14:20.0	6	2	47.991	2.419	2	59.217	2.974	93.	53.	33.	KPOT_jdavie01
217	70-192	1690	7786	4569	0	12:36:49.80	+13:09:46.3	4	1	31.332	2.268	1	42.761	2.608	259.	157.	23.	KPOT_rkennicu_1
218	42-178	1692	7785	4570	0	12:36:53.40	+07:14:48.0	1	0	1.339	0.0	0	2.675	0.0	84.	84.	0.	OT1_lcortese_1
219	70-195	1720	7793	4578	0	12:37:30.55	+09:33:18.4	1	0	1.607	0.0	0	0.94	0.0	90.	90.	0.	OT1_lcortese_1
220	70-197	1727	7796	4579	0	12:37:43.52	+11:49:05.5	5	1	25.583	3.355	1	38.766	2.589	264.	205.	-80.	KPOT_rkennicu_1
221	42-183	1730	7794	4580	0	12:37:48.40	+05:22:06.4	3	1	5.049	0.335	1	7.3	0.501	83.	73.	-20.	OT1_lcortese_1
222	70-199	1757	7803	4584	0	12:38:17.89	+13:06:35.5	3	1	0.523	0.228	1	1.259	0.201	82.	44.	20.	OT1_lcortese_1
223	42-186	1758	7802	0	0	12:38:20.82	+07:53:28.7	10	1	0.346	0.139	1	0.612	0.145	64.	33.	55.	OT1_lcortese_1
224	42-187	1760	7804	4586	0	12:38:28.44	+04:19:08.8	3	1	2.206	0.53	1	2.806	0.514	182.	49.	-65.	OT1_lcortese_1
225	70-202	1778	7817	0	3611	12:39:04.14	+13:21:48.7	5	1	0.044	0.025	1	0.194	0.038	25.	20.	-65.	OT1_lcortese_1
226	42-191	1780	7821	4591	0	12:39:12.44	+06:00:44.3	5	1	1.717	0.217	1	2.468	0.226	82.	37.	40.	OT1_lcortese_1
227	14-091	0	7819	4592	0	12:39:18.74	-00:31:55.2	10	1	5.65	0.713	1	6.237	0.875	242.	63.	-85.	OT1_lcortese_1
228	0	0	0	0	0	12:39:22.26	-05:39:53.3	13	0	0.111	0.0	0	0.113	0.0	22.	22.	0.	OT1_lcortese_1
229	70-204	1809	7825	0	3631	12:39:48.02	+12:58:26.1	5	0	0.368	0.0	0	0.357	0.0	46.	46.	0.	OT1_lcortese_1
230	99-106	1811	7826	4595	0	12:39:51.91	+15:17:52.1	5	1	3.515	0.327	1	3.768	0.323	91.	60.	-70.	OT1_lcortese_1
231	70-206	1813	7828	4596	0	12:39:55.94	+10:10:33.9	1	1	1.102	0.113	1	0.897	0.125	40.	40.	0.	OT1_lcortese_1
232	70-213	1859	7839	4606	0	12:40:57.56	+11:54:43.6	3	1	2.524	0.289	1	2.9	0.28	66.	57.	33.	OT1_lcortese_1
233	70-216	1868	7843	4607	0	12:41:12.41	+11:53:11.9	5	1	8.108	0.768	1	10.674	0.752	164.	57.	4.	OT1_lcortese_1

Continued on the next page...

Table 1 – Continued.

HRS	CGCG	VCC	UGC	NGC	IC	R.A. (J.2000) hh:mm:ss.ss	Dec (J.2000) dd:mm:ss.s	Type	$Flag_{100}$	F_{100} Jy	σ_{100} Jy	$Flag_{160}$	F_{160} Jy	σ_{160} Jy	a arcsec	b arcsec	P.A. degree	Proposal ID
234	70-214	1869	7842	4608	0	12:41:13.29	+10:09:20.9	1	0	2.29	0.0	0	1.576	0.0	103.	103.	0.	OT1_lcortese_1
235	42-205	1883	7850	4612	0	12:41:32.76	+07:18:53.2	1	0	0.343	0.0	0	0.579	0.0	51.	51.	0.	OT1_lcortese_1
236	70-223	1903	7858	4621	0	12:42:02.32	+11:38:48.9	0	0	0.877	0.0	0	0.512	0.0	69.	69.	0.	OT1_lcortese_1
237	42-208	1923	7871	4630	0	12:42:31.15	+03:57:37.3	12	1	5.408	0.703	1	6.54	0.611	97.	67.	10.	OT1_lcortese_1
238	14-109	0	7869	4629	0	12:42:32.67	-01:21:02.4	11	1	0.695	0.179	1	0.581	0.234	50.	45.	80.	OT1_lcortese_1
239	99-112	1932	7875	4634	0	12:42:40.96	+14:17:45.0	8	1	11.903	0.702	1	13.602	0.771	119.	51.	-24.	OT1_lcortese_1
240	70-229	1938	7880	4638	0	12:42:47.43	+11:26:32.9	1	0	0.642	0.0	0	0.369	0.0	48.	48.	0.	OT1_lcortese_1
241	43-002	1939	7878	4636	0	12:42:49.87	+02:41:16.0	0	1	0.31	0.07	1	0.32	0.066	37.	35.	0.	OT1_lcortese_1
242	70-230	1943	7884	4639	0	12:42:52.37	+13:15:26.9	6	1	6.587	0.759	1	7.273	0.849	134.	84.	-57.	OT1_lcortese_1
243	15-008	0	7895	4643	0	12:43:20.14	+01:58:42.1	2	1	0.673	1.005	1	3.354	0.916	107.	104.	-45.	OT1_lcortese_1
244	71-015	1972	7896	4647	0	12:43:32.45	+11:34:57.4	7	1	17.159	1.265	1	24.35	1.408	109.	91.	-75.	OT1_lcortese_1
245	71-016	1978	7898	4649	0	12:43:40.01	+11:33:09.4	0	0	0.243	0.0	0	0.605	0.0	45.	45.	0.	OT1_lcortese_1
246	100-004	0	7901	4651	0	12:43:42.63	+16:23:36.2	7	1	17.873	1.553	1	22.95	1.833	164.	116.	80.	OT1_lcortese_1
247	71-019	1987	7902	4654	0	12:43:56.58	+13:07:36.0	8	1	41.7	2.59	1	55.404	3.425	210.	109.	-52.	OT1_lcortese_1
248	71-023	2000	7914	4660	0	12:44:31.97	+11:11:25.9	0	0	0.142	0.0	0	0.142	0.0	22.	22.	0.	OT1_lcortese_1
249	71-026	2006	7920	0	3718	12:44:45.99	+12:21:05.2	5	1	0.208	0.045	1	0.088	0.025	29.	24.	72.	OT1_lcortese_1
250	43-018	0	7924	4665	0	12:45:05.96	+03:03:20.5	2	0	2.45	0.0	0	2.556	0.0	108.	108.	0.	OT1_lcortese_1
251	15-015	0	7926	4666	0	12:45:08.59	-00:27:42.8	7	1	99.531	5.076	1	113.011	5.791	198.	81.	44.	OT1_lcortese_1
252	15-016	0	7931	4668	0	12:45:32.14	-00:32:05.0	9	1	1.662	0.424	1	1.726	0.4	100.	52.	5.	OT1_lcortese_1
253	15-019	0	7951	4684	0	12:47:17.52	-02:43:38.6	1	1	2.112	0.176	1	1.58	0.125	50.	47.	20.	OT1_lcortese_1
254	71-043	2058	7965	4689	0	12:47:45.56	+13:45:46.1	6	1	12.633	3.503	1	18.399	3.807	246.	186.	-16.	OT1_lcortese_1
255	43-028	0	7961	4688	0	12:47:46.46	+04:20:09.9	8	1	3.409	1.426	1	3.476	0.613	107.	98.	35.	OT1_lcortese_1
256	15-023	0	0	4691	0	12:48:13.63	-03:19:57.8	3	1	23.132	1.206	1	20.28	1.095	83.	74.	-75.	OT1_lcortese_1
257	71-045	2070	7970	4698	0	12:48:22.92	+08:29:14.3	4	1	3.278	0.908	1	4.883	0.894	149.	74.	-15.	OT1_lcortese_1
258	0	0	0	4697	0	12:48:35.91	-05:48:03.1	0	1	1.376	0.131	1	0.849	0.132	40.	40.	0.	OT1_lcortese_1
259	43-034	0	7975	4701	0	12:49:11.56	+03:23:19.4	8	1	6.584	1.499	1	7.759	1.956	151.	126.	40.	OT1_lcortese_1
260	100-011	0	7980	4710	0	12:49:38.96	+15:09:55.8	1	1	13.653	0.771	1	15.533	0.92	104.	61.	27.	OT1_lcortese_1
261	43-040	0	7982	0	0	12:49:50.19	+02:51:10.4	9	1	1.179	0.335	1	2.729	0.355	98.	35.	0.	OT1_lcortese_1
262	43-041	0	7985	4713	0	12:49:57.87	+05:18:41.1	9	1	11.675	1.373	1	12.858	1.079	134.	91.	-70.	OT1_lcortese_1
263	129-027	0	7989	4725	0	12:50:26.61	+25:30:02.7	4	1	25.625	5.416	1	49.023	5.139	420.	385.	35.	KPOT_rkennicu_1
264	15-027	0	7991	0	0	12:50:38.96	+01:27:52.3	9	1	0.326	0.136	1	1.059	0.099	72.	26.	-10.	OT1_lcortese_1
265	0	0	0	4720	0	12:50:42.78	-04:09:21.0	13	1	2.061	0.243	1	2.044	0.148	58.	44.	-65.	OT1_lcortese_1
266	0	0	0	4731	0	12:51:01.09	-06:23:35.0	8	1	8.201	2.776	1	12.794	2.873	278.	136.	90.	OT1_lcortese_1
267	129-028	0	8005	4747	0	12:51:45.96	+25:46:38.3	8	1	3.826	1.103	1	6.215	0.992	166.	76.	30.	OT1_lcortese_1
268	71-060	0	8007	4746	0	12:51:55.37	+12:04:58.9	5	1	11.969	0.675	1	13.585	0.765	93.	52.	-60.	OT1_lcortese_1
269	71-062	2092	8010	4754	0	12:52:17.56	+11:18:49.2	1	0	3.468	0.0	0	2.459	0.0	120.	120.	0.	OT1_lcortese_1
270	15-029	0	8009	4753	0	12:52:22.11	-01:11:58.9	13	1	8.061	1.914	1	11.83	1.406	203.	121.	-75.	OT1_lcortese_1
271	100-015	0	8014	4758	0	12:52:44.04	+15:50:55.9	12	1	3.233	0.449	1	4.223	0.449	129.	58.	-20.	OT1_lcortese_1
272	71-065	2095	8016	4762	0	12:52:56.05	+11:13:50.9	1	0	12.944	0.0	0	10.721	0.0	208.	208.	0.	OT1_lcortese_1
273	15-031	0	8020	4771	0	12:53:21.27	+01:16:09.0	9	1	4.318	0.802	1	7.264	0.829	171.	66.	-45.	OT1_lcortese_1
274	15-032	0	8021	4772	0	12:53:29.17	+02:10:06.0	3	1	1.197	0.235	1	3.001	0.295	118.	44.	-35.	OT1_lcortese_1
275	0	0	0	4775	0	12:53:45.70	-06:37:19.8	9	1	10.521	0.813	1	10.513	0.865	90.	84.	50.	OT1_lcortese_1
276	71-068	0	8022	4779	0	12:53:50.86	+09:42:35.7	6	1	4.501	0.433	1	4.355	0.403	88.	77.	10.	OT1_lcortese_1
277	43-060	0	0	4791	0	12:54:43.97	+08:03:10.7	17	1	0.376	0.095	1	0.69	0.134	50.	34.	65.	OT1_lcortese_1
278	71-071	0	8032	0	0	12:54:44.19	+13:14:14.2	5	1	1.098	0.472	1	1.506	0.275	116.	39.	-15.	OT1_lcortese_1
279	15-037	0	8041	0	0	12:55:12.68	+00:07:00.0	9	1	1.769	0.755	1	4.518	0.564	130.	80.	-23.	OT1_lcortese_1
280	43-066	0	8043	4799	0	12:55:15.53	+02:53:47.9	5	1	3.51	0.251	1	3.967	0.239	73.	39.	90.	OT1_lcortese_1
281	43-068	0	8045	0	0	12:55:23.62	+07:54:34.0	12	1	0.446	0.094	1	0.632	0.093	38.	30.	-75.	OT1_lcortese_1
282	43-069	0	0	4803	0	12:55:33.67	+08:14:25.8	17	0	0.118	0.0	0	0.133	0.0	22.	22.	0.	OT1_lcortese_1
283	43-071	0	8054	4808	0	12:55:48.94	+04:18:14.7	8	1	15.894	0.959	1	19.757	1.077	111.	70.	-53.	OT1_lcortese_1
284	0	0	0	0	3908	12:56:40.62	-07:33:46.1	9	1	16.823	0.883	1	17.731	0.908	91.	44.	-10.	OT1_lcortese_1
285	15-049	0	8078	4845	0	12:58:01.19	+01:34:33.0	4	1	22.761	1.473	1	27.136	1.842	218.	69.	80.	OT1_lcortese_1
286	71-092	0	8102	4866	0	12:59:27.14	+14:10:15.8	1	1	0.961	0.31	1	1.54	0.27	197.	28.	87.	OT1_lcortese_1
287	15-055	0	8121	4904	0	13:00:58.67	-00:01:38.8	8	1	6.998	0.774	1	9.004	0.949	115.	104.	-35.	OT1_lcortese_1
288	0	0	0	4941	0	13:04:13.14	-05:33:05.8	4	1	5.335	0.983	1	9.141	0.965	152.	82.	15.	OT1_lcortese_1
289	0	0	0	4981	0	13:08:48.74	-06:46:39.1	6	1	12.715	0.947	1	16.561	1.065	116.	86.	-31.	OT1_lcortese_1
290	189-037	0	8271	5014	0	13:11:31.16	+36:16:54.9	3	1	4.237	0.276	1	3.989	0.321	64.	52.	-78.	OT1_lcortese_1
291	217-031	0	8388	5103	0	13:20:30.08	+43:05:02.3	4	0	0.93	0.0	0	0.46	0.0	60.	60.	0.	OT1_lcortese_1
292	218-010	0	8439	5145	0	13:25:13.92	+43:16:02.2	5	1	12.76	0.763	1	12.629	0.731	84.	75.	85.	OT1_lcortese_1
293	16-069	0	8443	5147	0	13:26:19.71	+02:06:02.7	10	1	6.929	0.585	1	8.435	0.571	93.	77.	-55.	OT1_lcortese_1
294	246-017	0	8593	0	902	13:36:01.22	+49:57:39.0	5	1	2.84	0.302	1	3.614	0.288	94.	47.	-20.	OT1_lcortese_1
295	73-054	0	8616	5248	0	13:37:32.07	+08:53:06.2	6	1	59.271	6.469	1	76.825	5.363	260.	188.	-40.	OT1_lcortese_1
296	190-041	0	8675	5273	0	13:42:08.34	+35:39:15.2	1	1	1.02	0.342	1	0.913	0.103	57.	56.	-85.	OT1_lcortese_1
297	246-023	0	8711	5301	0	13:46:24.61	+46:06:26.7	6	1	9.13	0.952	1	13.649	0.834	182.	72.	-30.	OT1_lcortese_1
298	218-047	0	8725	5303	0	13:47:44.97	+38:18:16.4	13	1	5.863	0.378	1	6.448	0.385	65	53	85.	OT1_lcortese_1
299	45-108	0	8727	5300	0	13:48:16.04	+03:57:03.1	7	1	5.027	1.139	1	7.654	1.211	163.	108.	-40.	OT1_lcortese_1
300	218-058	0	8756	0	0	13:50:35.89	+42:32:29.5	4	1	0.628	0.104	1	0.853	0.169	58.	32.	85.	OT1_lcortese_1
301	17-088	0	8790	5334	4338	13:52:54.46	-01:06:52.7	7	1	5.009	1.236	1	8.024	1.589	175.	127.	40.	OT1_lcortese_1
302	45-137	0	8821	5348	0	13:54:11.27	+05:13:38.8	6	1	1.507	0.52	1	1.961	0.535	154.	40.	-3.	OT1_lcortese_1
303	295-024	0	8843	5372	0	13:54:46.01	+58:39:59.4	5	1	4.719	0.292	1	3.354	0.374	62.	58.	40.	OT1_lcortese_1
304	46-001	0	8831	5356	0	13:54:58.46	+05:20:01.4	6	1	3.403	0.489	1	5.721	0.553	133.	51.	12.	OT1_lcortese_1
305	46-003	0	8838	5360	958	13:55:38.75	+04:59:06.2	13	1	0.236	0.105	1	0.489	0.114	83.	29.	70.	OT1_lcortese_1
306	46-007	0	8847	5363	0	13:56:07.21	+05:15:17.2	13	1	5.3	1.69	1	7.018	1.311	171.	110.	-50.	OT1_lcortese_1
307	46-009	0	8853	5364	0	13:56:12.00	+05:00:52.1	6	1	18.365	3.444	1	30.263	4.249	284.	184.	30.	OT1_lcortese_1
308	46-011	0	8857	0	0	13:56:26.61	+04:23:48.0	5	1	0.087	0.019	1	0.158	0.026	20.	20.	-0.	OT1_lcortese_1
309	272-031	0	9036	5486	0	14:07:24.97	+55:06:11.1	11	1	1.185	0.135	1	1.071	0.135	45.	44.	-55.	OT1_lcortese_1
310	47-010	0	9172	5560	0	14:20:05.42	+03:59:28.4	5	1	4.257	0.395	1	6.346	0.518	149.	51.	-65.	OT1_lcortese_1
311	47-012	0	9175	5566	0	14:20:19.95	+03:56:00.9	4	1	7.067	1.771	1	12.277	1.435	197.	103.	35.	OT1_lcortese_1

Continued on the next page...

Table 1 – Continued.

HRS	CGCG	VCC	UGC	NGC	IC	R.A. (J.2000) hh:mm:ss.ss	Dec (J.2000) dd:mm:ss.s	Type	$Flag_{100}$	F_{100} Jy	σ_{100} Jy	$Flag_{160}$	F_{160} Jy	σ_{160} Jy	a arcsec	b arcsec	P.A. degree	Proposal ID
312	47-020	0	9183	5576	0	14:21:03.68	+03:16:15.6	0	0	0.236	0.0	0	0.187	0.0	31.	31.	0.	OT1_lcortese_1
313	47-022	0	9187	5577	0	14:21:13.11	+03:26:08.8	6	1	2.55	0.802	1	3.803	0.819	154.	65.	55.	OT1_lcortese_1
314	19-012	0	9215	0	0	14:23:27.12	+01:43:34.7	9	1	2.772	0.417	1	3.316	0.23	95.	63.	-15.	OT1_lcortese_1
315	220-015	0	9242	0	0	14:25:21.02	+39:32:22.5	7	1	1.056	0.409	1	0.863	0.327	176.	29.	71.	OT1_lcortese_1
316	47-063	0	9308	5638	0	14:29:40.39	+03:14:00.2	0	0	0.15	0.0	0	0.169	0.0	24.	24.	0.	OT1_lcortese_1
317	47-066	0	9311	0	1022	14:30:01.85	+03:46:22.3	5	1	0.222	0.1	1	0.475	0.062	34.	28.	-15.	OT1_lcortese_1
318	47-070	0	9328	5645	0	14:30:39.35	+07:16:30.3	9	1	4.998	0.406	1	6.331	0.483	101.	63.	-75.	OT1_lcortese_1
319	75-064	0	9353	5669	0	14:32:43.88	+09:53:30.5	8	1	6.923	0.996	1	8.145	1.192	167.	118.	61.	OT1_lcortese_1
320	47-090	0	9363	5668	0	14:33:24.34	+04:27:01.6	9	1	7.735	2.205	1	10.256	1.478	152.	145.	17.	OT1_lcortese_1
321	47-123	0	9427	5692	0	14:38:18.12	+03:24:37.2	5	1	2.942	0.17	1	3.164	0.179	50.	33.	40.	OT1_lcortese_1
322	47-127	0	9436	5701	0	14:39:11.06	+05:21:48.8	3	1	1.453	1.035	1	1.859	1.201	124.	120.	-90.	OT1_lcortese_1
323	48-004	0	9483	0	1048	14:42:57.88	+04:53:24.5	5	1	5.689	0.391	1	7.547	0.575	101.	47.	-17.	OT1_lcortese_1

Table 3: Best-fitting dust temperatures and masses for a single modified black-body with β=2 and β=free.Only galaxies for which the reduced χ^2 corresponds to a probability $P \geq$95% are shown.

HRS	D	β=2		β=free		
		T	log(M$_{dust}$)	β	T	log(M$_{dust}$)
	Mpc	K	M$_\odot$		K	M$_\odot$
1	16.79	$21.7^{+1.0}_{-1.0}$	$5.93^{+0.07}_{-0.07}$	$2.0^{+0.5}_{-0.5}$	$21.5^{+3.8}_{-3.1}$	$5.94^{+0.15}_{-0.14}$
2	18.44	$24.0^{+0.6}_{-0.6}$	$6.27^{+0.04}_{-0.04}$	$2.3^{+0.3}_{-0.3}$	$21.6^{+1.9}_{-1.6}$	$6.36^{+0.07}_{-0.07}$
5	16.71	$22.4^{+0.4}_{-0.4}$	$6.62^{+0.02}_{-0.02}$	$2.2^{+0.2}_{-0.2}$	$20.9^{+1.0}_{-1.0}$	$6.68^{+0.05}_{-0.04}$
6	18.89	$13.9^{+0.8}_{-0.8}$	$6.80^{+0.11}_{-0.11}$	$1.4^{+1.0}_{-0.8}$	$16.6^{+5.8}_{-4.0}$	$6.57^{+0.37}_{-0.33}$
7	18.77	$25.7^{+0.3}_{-0.3}$	$6.26^{+0.01}_{-0.01}$	$2.2^{+0.1}_{-0.1}$	$23.9^{+0.8}_{-0.8}$	$6.31^{+0.03}_{-0.03}$
8	19.37	$15.3^{+0.8}_{-0.7}$	$7.48^{+0.06}_{-0.06}$	$1.3^{+0.4}_{-0.3}$	$20.9^{+3.6}_{-3.2}$	$7.11^{+0.18}_{-0.16}$
9	20.21	$21.8^{+0.9}_{-0.9}$	$6.53^{+0.06}_{-0.05}$	$2.5^{+0.4}_{-0.4}$	$18.9^{+2.4}_{-2.0}$	$6.66^{+0.12}_{-0.12}$
11	18.93	-	-	$1.6^{+0.1}_{-0.1}$	$23.7^{+1.0}_{-1.0}$	$6.82^{+0.04}_{-0.04}$
12	19.89	$23.6^{+0.7}_{-0.7}$	$5.72^{+0.05}_{-0.05}$	$1.2^{+0.4}_{-0.3}$	$31.9^{+6.0}_{-4.3}$	$5.51^{+0.11}_{-0.12}$
13	22.47	$21.8^{+0.3}_{-0.3}$	$7.57^{+0.02}_{-0.02}$	$1.9^{+0.1}_{-0.1}$	$22.5^{+0.7}_{-0.7}$	$7.54^{+0.03}_{-0.03}$
15	18.57	$19.2^{+0.7}_{-0.7}$	$7.60^{+0.06}_{-0.05}$	$1.7^{+0.3}_{-0.3}$	$20.8^{+2.7}_{-2.3}$	$7.52^{+0.12}_{-0.12}$
16	18.00	$19.7^{+0.4}_{-0.4}$	$7.17^{+0.03}_{-0.03}$	$1.9^{+0.2}_{-0.2}$	$20.0^{+1.3}_{-1.2}$	$7.16^{+0.06}_{-0.06}$
17	18.30	$21.2^{+0.4}_{-0.4}$	$7.17^{+0.03}_{-0.03}$	$1.7^{+0.1}_{-0.1}$	$23.6^{+1.4}_{-1.3}$	$7.08^{+0.05}_{-0.05}$
18	22.91	$20.7^{+0.7}_{-0.7}$	$6.61^{+0.05}_{-0.05}$	$1.9^{+0.3}_{-0.3}$	$21.3^{+2.3}_{-2.0}$	$6.59^{+0.10}_{-0.09}$
19	23.29	$21.0^{+0.6}_{-0.6}$	$6.99^{+0.04}_{-0.04}$	$1.5^{+0.2}_{-0.2}$	$25.3^{+2.7}_{-2.3}$	$6.83^{+0.09}_{-0.09}$
21	16.89	-	-	$0.8^{+0.5}_{-0.4}$	$29.3^{+8.8}_{-5.7}$	$5.85^{+0.19}_{-0.20}$
22	20.20	$20.4^{+0.9}_{-0.8}$	$6.15^{+0.10}_{-0.10}$	$1.2^{+0.6}_{-0.6}$	$26.1^{+7.4}_{-4.6}$	$5.96^{+0.18}_{-0.21}$
23	21.44	$23.3^{+0.3}_{-0.3}$	$7.31^{+0.02}_{-0.02}$	$1.9^{+0.1}_{-0.1}$	$24.1^{+0.8}_{-0.8}$	$7.28^{+0.03}_{-0.03}$
24	22.64	$20.5^{+0.5}_{-0.5}$	$7.50^{+0.03}_{-0.03}$	$1.8^{+0.2}_{-0.2}$	$21.8^{+1.4}_{-1.3}$	$7.44^{+0.06}_{-0.06}$
26	22.41	-	-	$0.9^{+0.3}_{-0.3}$	$29.2^{+4.9}_{-3.7}$	$6.01^{+0.11}_{-0.12}$
27	24.77	$24.5^{+0.6}_{-0.6}$	$6.56^{+0.03}_{-0.03}$	$2.2^{+0.2}_{-0.2}$	$23.3^{+1.9}_{-1.7}$	$6.60^{+0.07}_{-0.07}$
28	19.03	$21.4^{+0.3}_{-0.3}$	$6.76^{+0.02}_{-0.02}$	-	-	-
29	15.73	$20.2^{+0.6}_{-0.6}$	$6.56^{+0.05}_{-0.05}$	$1.6^{+0.3}_{-0.3}$	$23.2^{+2.7}_{-2.3}$	$6.44^{+0.10}_{-0.10}$
30	15.79	$19.5^{+0.7}_{-0.7}$	$6.71^{+0.06}_{-0.06}$	$1.4^{+0.3}_{-0.3}$	$24.2^{+3.6}_{-2.9}$	$6.51^{+0.12}_{-0.12}$
31	19.63	$23.1^{+0.7}_{-0.7}$	$7.06^{+0.04}_{-0.04}$	$1.3^{+0.3}_{-0.3}$	$29.4^{+4.1}_{-3.2}$	$6.87^{+0.10}_{-0.10}$
33	20.46	$21.3^{+0.4}_{-0.4}$	$6.98^{+0.03}_{-0.03}$	$1.8^{+0.2}_{-0.2}$	$22.7^{+1.4}_{-1.3}$	$6.93^{+0.05}_{-0.05}$
34	16.14	$19.1^{+0.5}_{-0.5}$	$7.07^{+0.04}_{-0.04}$	$1.6^{+0.2}_{-0.2}$	$21.8^{+1.6}_{-1.5}$	$6.95^{+0.07}_{-0.07}$
36	21.94	$26.3^{+0.4}_{-0.4}$	$7.33^{+0.02}_{-0.02}$	$2.0^{+0.1}_{-0.1}$	$26.3^{+1.2}_{-1.1}$	$7.33^{+0.04}_{-0.04}$
37	19.61	$22.6^{+0.4}_{-0.4}$	$6.73^{+0.03}_{-0.03}$	$2.0^{+0.2}_{-0.2}$	$22.5^{+1.5}_{-1.3}$	$6.73^{+0.06}_{-0.06}$
38	20.27	-	-	$1.2^{+0.2}_{-0.2}$	$26.2^{+3.2}_{-2.7}$	$6.41^{+0.10}_{-0.10}$
39	22.24	$18.3^{+1.0}_{-1.1}$	$6.65^{+0.08}_{-0.07}$	$1.1^{+0.4}_{-0.4}$	$24.7^{+4.4}_{-3.5}$	$6.37^{+0.14}_{-0.14}$
40	22.63	$23.7^{+0.4}_{-0.4}$	$6.71^{+0.02}_{-0.02}$	$1.8^{+0.2}_{-0.2}$	$25.5^{+1.7}_{-1.5}$	$6.65^{+0.05}_{-0.05}$
41	18.61	$18.8^{+0.7}_{-0.7}$	$6.56^{+0.05}_{-0.05}$	$1.4^{+0.3}_{-0.3}$	$23.9^{+3.2}_{-2.7}$	$6.33^{+0.12}_{-0.11}$
42	17.04	$20.5^{+0.7}_{-0.7}$	$7.32^{+0.05}_{-0.05}$	$1.7^{+0.3}_{-0.3}$	$22.7^{+2.4}_{-2.1}$	$7.22^{+0.10}_{-0.10}$
44	16.01	$23.3^{+0.6}_{-0.6}$	$6.17^{+0.04}_{-0.04}$	$1.3^{+0.3}_{-0.2}$	$30.1^{+3.8}_{-3.0}$	$5.97^{+0.08}_{-0.09}$
46	21.34	$24.5^{+0.4}_{-0.4}$	$6.62^{+0.02}_{-0.02}$	$2.1^{+0.2}_{-0.2}$	$24.0^{+1.4}_{-1.2}$	$6.64^{+0.05}_{-0.05}$
47	21.53	$20.2^{+0.9}_{-0.9}$	$6.83^{+0.06}_{-0.06}$	$1.3^{+0.3}_{-0.3}$	$25.3^{+4.0}_{-3.1}$	$6.63^{+0.12}_{-0.13}$
48	16.50	$21.5^{+0.5}_{-0.5}$	$7.53^{+0.04}_{-0.04}$	$1.9^{+0.3}_{-0.3}$	$22.0^{+1.9}_{-1.7}$	$7.51^{+0.07}_{-0.07}$
50	21.43	-	-	$2.2^{+0.1}_{-0.1}$	$22.9^{+0.7}_{-0.7}$	$7.31^{+0.03}_{-0.03}$
51	18.56	-	-	$1.4^{+0.2}_{-0.2}$	$26.0^{+2.1}_{-1.8}$	$6.65^{+0.07}_{-0.07}$
52	17.20	$20.9^{+1.3}_{-1.4}$	$6.11^{+0.09}_{-0.09}$	$1.8^{+0.5}_{-0.5}$	$22.1^{+4.6}_{-3.6}$	$6.05^{+0.17}_{-0.17}$
53	15.14	-	-	$1.5^{+0.1}_{-0.1}$	$24.3^{+1.5}_{-1.4}$	$6.86^{+0.06}_{-0.06}$
54	17.77	$20.1^{+0.9}_{-0.9}$	$6.71^{+0.06}_{-0.05}$	$1.8^{+0.3}_{-0.3}$	$21.9^{+3.0}_{-2.6}$	$6.63^{+0.13}_{-0.12}$
55	16.54	$20.9^{+0.4}_{-0.4}$	$7.05^{+0.03}_{-0.03}$	$1.9^{+0.2}_{-0.2}$	$21.4^{+1.3}_{-1.2}$	$7.02^{+0.06}_{-0.06}$
57	16.51	$20.9^{+0.3}_{-0.3}$	$7.25^{+0.02}_{-0.02}$	$2.1^{+0.1}_{-0.1}$	$20.4^{+1.0}_{-0.9}$	$7.28^{+0.05}_{-0.05}$
59	24.53	$19.6^{+0.4}_{-0.4}$	$7.24^{+0.04}_{-0.04}$	$1.6^{+0.2}_{-0.2}$	$22.2^{+1.8}_{-1.6}$	$7.12^{+0.07}_{-0.07}$
60	15.14	$21.3^{+0.4}_{-0.4}$	$6.92^{+0.03}_{-0.03}$	$2.0^{+0.1}_{-0.1}$	$21.1^{+1.2}_{-1.1}$	$6.92^{+0.06}_{-0.05}$
61	17.39	$19.3^{+0.8}_{-0.8}$	$6.21^{+0.06}_{-0.06}$	$1.3^{+0.4}_{-0.3}$	$24.0^{+3.6}_{-2.9}$	$6.02^{+0.12}_{-0.12}$
62	22.44	-	-	$1.0^{+0.3}_{-0.3}$	$26.8^{+3.9}_{-3.1}$	$6.73^{+0.11}_{-0.11}$
63	18.41	$18.7^{+0.5}_{-0.5}$	$7.39^{+0.04}_{-0.04}$	$1.8^{+0.2}_{-0.2}$	$20.1^{+1.6}_{-1.5}$	$7.31^{+0.08}_{-0.08}$
64	17.33	$17.7^{+0.9}_{-0.9}$	$6.65^{+0.08}_{-0.07}$	$1.3^{+0.4}_{-0.3}$	$23.4^{+4.0}_{-3.3}$	$6.36^{+0.15}_{-0.15}$
65	19.76	$18.5^{+1.2}_{-1.2}$	$6.77^{+0.09}_{-0.08}$	$1.0^{+0.4}_{-0.4}$	$27.6^{+6.4}_{-4.6}$	$6.40^{+0.17}_{-0.17}$
66	20.97	$23.9^{+0.2}_{-0.2}$	$7.33^{+0.01}_{-0.01}$	-	-	-
67	20.51	$17.9^{+0.9}_{-0.9}$	$6.65^{+0.08}_{-0.08}$	$1.2^{+0.4}_{-0.4}$	$23.2^{+4.1}_{-3.2}$	$6.40^{+0.15}_{-0.15}$
69	16.73	$18.0^{+1.2}_{-1.2}$	$7.04^{+0.10}_{-0.09}$	$1.5^{+0.5}_{-0.5}$	$21.5^{+5.1}_{-3.8}$	$6.85^{+0.22}_{-0.21}$

Continued on the next page...

Table 3 – Continued.

HRS	D	β=2		β=free		
		T	log(M$_{dust}$)	β	T	log(M$_{dust}$)
	Mpc	K	M$_\odot$		K	M$_\odot$
70	23.10	$20.7^{+0.6}_{-0.6}$	$6.64^{+0.04}_{-0.04}$	$1.7^{+0.2}_{-0.2}$	$23.0^{+2.0}_{-1.8}$	$6.55^{+0.08}_{-0.08}$
72	22.53	$24.7^{+1.0}_{-0.9}$	$6.31^{+0.06}_{-0.06}$	$1.5^{+0.5}_{-0.5}$	$29.5^{+7.5}_{-5.0}$	$6.19^{+0.14}_{-0.16}$
73	15.00	$19.3^{+0.3}_{-0.3}$	$7.77^{+0.03}_{-0.03}$	$2.2^{+0.2}_{-0.2}$	$18.3^{+1.1}_{-1.0}$	$7.83^{+0.07}_{-0.07}$
74	15.83	$23.9^{+0.4}_{-0.4}$	$6.95^{+0.03}_{-0.03}$	$2.0^{+0.2}_{-0.2}$	$24.1^{+1.6}_{-1.4}$	$6.94^{+0.05}_{-0.05}$
75	18.33	$15.6^{+0.9}_{-0.9}$	$6.34^{+0.11}_{-0.10}$	$1.6^{+0.7}_{-0.6}$	$17.4^{+4.0}_{-3.2}$	$6.21^{+0.25}_{-0.22}$
76	15.27	$18.8^{+1.0}_{-1.0}$	$6.19^{+0.08}_{-0.08}$	$1.1^{+0.4}_{-0.4}$	$26.2^{+5.0}_{-3.8}$	$5.89^{+0.14}_{-0.15}$
77	20.83	$22.4^{+0.3}_{-0.3}$	$7.93^{+0.01}_{-0.01}$	$2.2^{+0.1}_{-0.1}$	$21.3^{+0.7}_{-0.7}$	$7.98^{+0.03}_{-0.03}$
78	18.13	$19.8^{+0.5}_{-0.5}$	$6.67^{+0.05}_{-0.05}$	$1.4^{+0.4}_{-0.4}$	$24.0^{+3.5}_{-2.7}$	$6.49^{+0.12}_{-0.13}$
79	21.54	$19.9^{+1.0}_{-1.0}$	$6.49^{+0.08}_{-0.08}$	$1.4^{+0.6}_{-0.6}$	$23.9^{+6.2}_{-4.1}$	$6.33^{+0.18}_{-0.20}$
80	17.00	$17.7^{+1.1}_{-1.1}$	$6.84^{+0.09}_{-0.09}$	$1.7^{+0.6}_{-0.6}$	$19.3^{+4.2}_{-3.3}$	$6.75^{+0.21}_{-0.20}$
81	17.00	$22.4^{+0.3}_{-0.3}$	$7.14^{+0.02}_{-0.02}$	$2.0^{+0.1}_{-0.1}$	$22.8^{+1.0}_{-0.9}$	$7.12^{+0.04}_{-0.04}$
82	17.00	$23.4^{+1.0}_{-1.0}$	$6.09^{+0.06}_{-0.06}$	$1.7^{+0.4}_{-0.4}$	$25.7^{+4.3}_{-3.4}$	$6.02^{+0.12}_{-0.13}$
83	17.60	$19.8^{+1.3}_{-1.4}$	$6.00^{+0.10}_{-0.10}$	$0.9^{+0.4}_{-0.4}$	$30.4^{+8.6}_{-5.7}$	$5.65^{+0.18}_{-0.18}$
84	17.00	$21.2^{+0.4}_{-0.4}$	$6.40^{+0.03}_{-0.03}$	$2.0^{+0.2}_{-0.2}$	$21.0^{+1.3}_{-1.2}$	$6.40^{+0.06}_{-0.06}$
85	15.31	$21.4^{+0.4}_{-0.4}$	$7.36^{+0.03}_{-0.03}$	$1.8^{+0.1}_{-0.1}$	$23.2^{+1.3}_{-1.2}$	$7.29^{+0.05}_{-0.05}$
86	17.00	-	-	$1.2^{+0.2}_{-0.2}$	$26.2^{+3.4}_{-2.9}$	$6.86^{+0.11}_{-0.11}$
87	17.00	$22.8^{+1.1}_{-1.0}$	$6.15^{+0.07}_{-0.07}$	$2.0^{+0.5}_{-0.5}$	$22.5^{+4.3}_{-3.2}$	$6.16^{+0.15}_{-0.15}$
88	17.00	$20.5^{+0.9}_{-0.9}$	$7.26^{+0.06}_{-0.05}$	$1.3^{+0.3}_{-0.3}$	$26.3^{+3.8}_{-3.0}$	$7.03^{+0.11}_{-0.11}$
89	17.00	-	-	$1.1^{+0.1}_{-0.1}$	$24.9^{+1.5}_{-1.4}$	$7.19^{+0.06}_{-0.05}$
91	17.00	$19.6^{+0.3}_{-0.3}$	$7.81^{+0.03}_{-0.03}$	$2.0^{+0.2}_{-0.2}$	$19.8^{+1.2}_{-1.1}$	$7.80^{+0.06}_{-0.06}$
92	17.00	$19.4^{+0.6}_{-0.6}$	$6.59^{+0.05}_{-0.05}$	$1.6^{+0.3}_{-0.3}$	$22.1^{+2.4}_{-2.0}$	$6.46^{+0.10}_{-0.10}$
93	15.59	$21.0^{+0.8}_{-0.8}$	$6.40^{+0.07}_{-0.07}$	$2.0^{+0.5}_{-0.5}$	$20.9^{+3.6}_{-2.8}$	$6.40^{+0.14}_{-0.15}$
94	17.00	-	-	$1.0^{+0.2}_{-0.2}$	$23.5^{+1.9}_{-1.7}$	$6.87^{+0.07}_{-0.07}$
95	17.00	$24.5^{+0.3}_{-0.3}$	$6.64^{+0.02}_{-0.02}$	$2.2^{+0.1}_{-0.1}$	$22.9^{+0.9}_{-0.9}$	$6.69^{+0.04}_{-0.04}$
96	17.00	$22.3^{+0.3}_{-0.3}$	$7.31^{+0.02}_{-0.02}$	$2.1^{+0.1}_{-0.1}$	$21.3^{+0.8}_{-0.8}$	$7.35^{+0.04}_{-0.04}$
97	17.00	$18.7^{+0.3}_{-0.3}$	$7.77^{+0.02}_{-0.02}$	$1.9^{+0.1}_{-0.1}$	$19.1^{+0.8}_{-0.8}$	$7.75^{+0.04}_{-0.04}$
98	17.00	-	-	$1.4^{+0.2}_{-0.2}$	$22.7^{+1.5}_{-1.3}$	$6.80^{+0.06}_{-0.06}$
99	17.00	$22.5^{+0.4}_{-0.4}$	$6.00^{+0.03}_{-0.03}$	$2.4^{+0.2}_{-0.2}$	$20.2^{+1.3}_{-1.2}$	$6.09^{+0.06}_{-0.06}$
100	17.00	-	-	$2.3^{+0.1}_{-0.1}$	$19.8^{+0.5}_{-0.5}$	$7.17^{+0.03}_{-0.03}$
102	17.00	-	-	$2.3^{+0.1}_{-0.1}$	$21.0^{+1.0}_{-0.9}$	$8.06^{+0.04}_{-0.05}$
106	23.00	$20.5^{+1.2}_{-1.2}$	$6.74^{+0.08}_{-0.08}$	$1.7^{+0.5}_{-0.5}$	$22.8^{+4.7}_{-3.6}$	$6.65^{+0.17}_{-0.17}$
107	17.00	$19.2^{+0.6}_{-0.6}$	$6.40^{+0.05}_{-0.05}$	$1.6^{+0.3}_{-0.3}$	$21.8^{+2.6}_{-2.2}$	$6.29^{+0.10}_{-0.10}$
108	23.00	$22.6^{+0.9}_{-0.9}$	$6.24^{+0.06}_{-0.06}$	$2.2^{+0.5}_{-0.4}$	$21.4^{+3.1}_{-2.5}$	$6.29^{+0.12}_{-0.11}$
109	17.00	-	-	$1.2^{+0.2}_{-0.2}$	$24.5^{+2.2}_{-1.9}$	$6.56^{+0.08}_{-0.08}$
110	17.00	-	-	$1.4^{+0.2}_{-0.2}$	$25.4^{+1.9}_{-1.7}$	$6.76^{+0.06}_{-0.06}$
111	17.00	-	-	$2.3^{+0.1}_{-0.1}$	$19.3^{+0.5}_{-0.4}$	$7.43^{+0.02}_{-0.02}$
112	23.00	$21.4^{+0.8}_{-0.8}$	$6.34^{+0.06}_{-0.06}$	$1.6^{+0.4}_{-0.4}$	$24.2^{+3.7}_{-2.9}$	$6.23^{+0.12}_{-0.12}$
113	17.00	$19.7^{+0.2}_{-0.2}$	$7.63^{+0.01}_{-0.01}$	$2.2^{+0.1}_{-0.1}$	$18.7^{+0.5}_{-0.5}$	$7.69^{+0.03}_{-0.03}$
114	17.00	$22.9^{+0.3}_{-0.3}$	$7.91^{+0.02}_{-0.02}$	$2.0^{+0.1}_{-0.1}$	$23.2^{+1.0}_{-0.9}$	$7.91^{+0.04}_{-0.04}$
115	17.00	$21.6^{+0.6}_{-0.6}$	$6.04^{+0.04}_{-0.05}$	$1.8^{+0.3}_{-0.3}$	$23.1^{+2.5}_{-2.1}$	$5.99^{+0.09}_{-0.09}$
117	23.00	$20.2^{+0.4}_{-0.4}$	$7.24^{+0.03}_{-0.03}$	$2.3^{+0.2}_{-0.2}$	$18.7^{+1.1}_{-1.0}$	$7.31^{+0.06}_{-0.06}$
118	17.00	$20.4^{+1.1}_{-1.1}$	$6.32^{+0.08}_{-0.08}$	$1.2^{+0.5}_{-0.4}$	$26.7^{+6.2}_{-4.3}$	$6.09^{+0.16}_{-0.17}$
119	17.00	$22.3^{+0.5}_{-0.5}$	$6.82^{+0.04}_{-0.04}$	$2.6^{+0.3}_{-0.3}$	$19.2^{+1.6}_{-1.4}$	$6.95^{+0.08}_{-0.08}$
120	17.00	$20.3^{+0.4}_{-0.4}$	$6.92^{+0.04}_{-0.04}$	$2.4^{+0.3}_{-0.3}$	$18.4^{+1.4}_{-1.3}$	$7.01^{+0.07}_{-0.07}$
121	23.00	$20.4^{+0.2}_{-0.2}$	$7.25^{+0.02}_{-0.02}$	$2.1^{+0.1}_{-0.1}$	$20.1^{+0.7}_{-0.6}$	$7.27^{+0.03}_{-0.03}$
122	17.00	$21.1^{+0.3}_{-0.3}$	$8.09^{+0.03}_{-0.03}$	$2.2^{+0.2}_{-0.2}$	$19.9^{+1.1}_{-1.1}$	$8.15^{+0.05}_{-0.05}$
123	17.00	$19.0^{+0.7}_{-0.7}$	$6.67^{+0.05}_{-0.05}$	$2.0^{+0.3}_{-0.3}$	$19.2^{+2.1}_{-1.9}$	$6.66^{+0.12}_{-0.11}$
124	17.00	$18.9^{+0.7}_{-0.7}$	$6.98^{+0.05}_{-0.05}$	$1.8^{+0.4}_{-0.3}$	$19.9^{+2.4}_{-2.0}$	$6.93^{+0.12}_{-0.11}$
127	23.00	$20.4^{+0.3}_{-0.3}$	$7.14^{+0.02}_{-0.02}$	$2.0^{+0.1}_{-0.1}$	$20.6^{+0.9}_{-0.8}$	$7.13^{+0.04}_{-0.04}$
128	23.00	$17.7^{+0.5}_{-0.5}$	$6.76^{+0.04}_{-0.04}$	$2.0^{+0.3}_{-0.3}$	$17.8^{+1.7}_{-1.5}$	$6.76^{+0.10}_{-0.10}$
130	17.00	$20.5^{+0.7}_{-0.7}$	$6.52^{+0.05}_{-0.05}$	$1.7^{+0.3}_{-0.3}$	$22.6^{+2.7}_{-2.3}$	$6.44^{+0.10}_{-0.10}$
131	23.00	$19.1^{+0.8}_{-0.8}$	$6.55^{+0.07}_{-0.07}$	$2.5^{+0.6}_{-0.5}$	$16.7^{+2.7}_{-2.3}$	$6.69^{+0.17}_{-0.16}$
132	23.00	-	-	$0.8^{+0.4}_{-0.4}$	$33.8^{+8.9}_{-5.8}$	$6.12^{+0.15}_{-0.17}$
133	17.90	-	-	$0.6^{+0.3}_{-0.3}$	$27.1^{+4.9}_{-4.0}$	$6.53^{+0.15}_{-0.14}$
134	23.00	$20.8^{+0.7}_{-0.7}$	$6.70^{+0.05}_{-0.05}$	$2.3^{+0.4}_{-0.4}$	$19.1^{+2.2}_{-1.9}$	$6.77^{+0.11}_{-0.11}$
136	23.00	$22.4^{+0.3}_{-0.3}$	$6.75^{+0.02}_{-0.02}$	$2.4^{+0.2}_{-0.2}$	$20.0^{+1.0}_{-0.9}$	$6.84^{+0.05}_{-0.05}$
139	23.00	$21.3^{+0.6}_{-0.6}$	$6.59^{+0.04}_{-0.04}$	$1.4^{+0.3}_{-0.3}$	$26.1^{+3.4}_{-2.7}$	$6.42^{+0.10}_{-0.10}$

Continued on the next page...

Table 3 – Continued.

HRS	D	β=2		β=free		
		T	log(M$_{dust}$)	β	T	log(M$_{dust}$)
	Mpc	K	M$_\odot$		K	M$_\odot$
140	17.00	$17.4^{+0.8}_{-0.8}$	$7.01^{+0.08}_{-0.07}$	$2.1^{+0.5}_{-0.4}$	$17.1^{+2.5}_{-2.2}$	$7.03^{+0.17}_{-0.15}$
141	23.00	$18.6^{+0.3}_{-0.3}$	$7.39^{+0.03}_{-0.03}$	$2.3^{+0.3}_{-0.2}$	$17.4^{+1.1}_{-1.0}$	$7.45^{+0.07}_{-0.06}$
143	23.00	-	-	$1.5^{+0.1}_{-0.1}$	$23.3^{+1.2}_{-1.1}$	$7.17^{+0.05}_{-0.05}$
144	17.00	$23.9^{+0.3}_{-0.3}$	$7.07^{+0.02}_{-0.02}$	$1.9^{+0.2}_{-0.2}$	$24.4^{+1.5}_{-1.3}$	$7.05^{+0.05}_{-0.05}$
146	23.00	$20.1^{+0.4}_{-0.4}$	$6.87^{+0.03}_{-0.03}$	$1.5^{+0.2}_{-0.2}$	$24.1^{+1.9}_{-1.7}$	$6.71^{+0.07}_{-0.07}$
147	17.00	$17.9^{+0.5}_{-0.5}$	$6.92^{+0.04}_{-0.04}$	$1.6^{+0.2}_{-0.2}$	$21.0^{+1.6}_{-1.5}$	$6.76^{+0.08}_{-0.07}$
148	17.00	-	-	$1.2^{+0.2}_{-0.2}$	$24.1^{+1.9}_{-1.7}$	$6.82^{+0.07}_{-0.07}$
149	17.00	-	-	$2.2^{+0.1}_{-0.1}$	$19.9^{+0.5}_{-0.5}$	$7.47^{+0.03}_{-0.02}$
151	17.00	$21.1^{+0.7}_{-0.7}$	$6.68^{+0.05}_{-0.05}$	$1.7^{+0.3}_{-0.3}$	$23.3^{+3.1}_{-2.5}$	$6.60^{+0.11}_{-0.11}$
152	17.00	$24.4^{+0.4}_{-0.4}$	$6.54^{+0.02}_{-0.02}$	$2.3^{+0.2}_{-0.2}$	$22.4^{+1.4}_{-1.3}$	$6.61^{+0.05}_{-0.05}$
153	17.00	$20.6^{+0.5}_{-0.5}$	$6.72^{+0.04}_{-0.04}$	$1.9^{+0.3}_{-0.2}$	$21.2^{+1.8}_{-1.6}$	$6.69^{+0.08}_{-0.08}$
154	23.00	$17.9^{+0.8}_{-0.9}$	$7.13^{+0.08}_{-0.07}$	$1.0^{+0.4}_{-0.4}$	$24.5^{+4.4}_{-3.4}$	$6.84^{+0.14}_{-0.15}$
156	17.00	$23.9^{+0.4}_{-0.4}$	$7.05^{+0.02}_{-0.02}$	$2.2^{+0.1}_{-0.1}$	$22.6^{+1.0}_{-0.9}$	$7.10^{+0.04}_{-0.04}$
158	23.00	$17.7^{+0.8}_{-0.9}$	$6.86^{+0.08}_{-0.08}$	$0.9^{+0.5}_{-0.4}$	$24.4^{+4.9}_{-3.6}$	$6.56^{+0.15}_{-0.16}$
159	23.00	$25.2^{+0.5}_{-0.5}$	$6.75^{+0.03}_{-0.03}$	$2.2^{+0.3}_{-0.3}$	$23.6^{+2.0}_{-1.8}$	$6.80^{+0.06}_{-0.06}$
160	23.00	$19.8^{+0.5}_{-0.5}$	$7.24^{+0.03}_{-0.03}$	$2.1^{+0.2}_{-0.2}$	$19.4^{+1.4}_{-1.3}$	$7.26^{+0.07}_{-0.07}$
162	17.00	$25.1^{+0.8}_{-0.7}$	$6.35^{+0.06}_{-0.06}$	$2.7^{+0.4}_{-0.4}$	$20.9^{+2.3}_{-2.0}$	$6.48^{+0.09}_{-0.09}$
163	17.00	$21.3^{+0.4}_{-0.4}$	$7.19^{+0.03}_{-0.04}$	$2.1^{+0.3}_{-0.2}$	$20.8^{+1.7}_{-1.5}$	$7.21^{+0.08}_{-0.08}$
165	23.00	$20.4^{+1.0}_{-1.0}$	$6.44^{+0.07}_{-0.07}$	$1.6^{+0.4}_{-0.4}$	$23.5^{+3.8}_{-3.1}$	$6.32^{+0.13}_{-0.13}$
167	23.00	$19.6^{+0.4}_{-0.4}$	$6.76^{+0.04}_{-0.04}$	$2.7^{+0.3}_{-0.3}$	$16.5^{+1.2}_{-1.1}$	$6.93^{+0.08}_{-0.08}$
168	23.00	$21.0^{+0.6}_{-0.6}$	$6.35^{+0.05}_{-0.05}$	$1.2^{+0.3}_{-0.3}$	$27.0^{+4.0}_{-3.1}$	$6.15^{+0.11}_{-0.11}$
169	24.30	$20.1^{+0.7}_{-0.7}$	$6.73^{+0.05}_{-0.05}$	$1.8^{+0.3}_{-0.3}$	$21.4^{+2.4}_{-2.0}$	$6.68^{+0.10}_{-0.10}$
170	17.00	$19.9^{+1.1}_{-1.2}$	$7.29^{+0.08}_{-0.08}$	$1.9^{+0.5}_{-0.5}$	$20.8^{+4.4}_{-3.3}$	$7.25^{+0.20}_{-0.20}$
171	23.00	$23.5^{+0.4}_{-0.4}$	$6.76^{+0.02}_{-0.02}$	$2.2^{+0.2}_{-0.2}$	$22.0^{+1.3}_{-1.2}$	$6.81^{+0.05}_{-0.05}$
172	17.00	$22.2^{+0.7}_{-0.7}$	$6.63^{+0.04}_{-0.04}$	$2.3^{+0.3}_{-0.3}$	$20.1^{+2.0}_{-1.7}$	$6.72^{+0.10}_{-0.09}$
173	17.00	$23.9^{+0.4}_{-0.4}$	$6.82^{+0.02}_{-0.02}$	$2.2^{+0.2}_{-0.2}$	$22.3^{+1.4}_{-1.3}$	$6.88^{+0.06}_{-0.06}$
174	17.00	$25.9^{+0.3}_{-0.3}$	$6.23^{+0.01}_{-0.01}$	-	-	-
176	23.00	$21.9^{+0.4}_{-0.4}$	$6.81^{+0.03}_{-0.03}$	$2.3^{+0.2}_{-0.2}$	$20.0^{+1.2}_{-1.1}$	$6.90^{+0.06}_{-0.06}$
177	17.00	$22.8^{+0.3}_{-0.3}$	$6.57^{+0.02}_{-0.02}$	$1.9^{+0.2}_{-0.2}$	$23.4^{+1.3}_{-1.1}$	$6.55^{+0.05}_{-0.05}$
180	17.00	$25.6^{+0.9}_{-0.9}$	$5.72^{+0.06}_{-0.07}$	$3.5^{+0.8}_{-0.7}$	$17.9^{+3.2}_{-2.5}$	$5.96^{+0.12}_{-0.13}$
182	17.00	$20.6^{+0.3}_{-0.3}$	$6.82^{+0.02}_{-0.02}$	$1.7^{+0.1}_{-0.1}$	$23.0^{+1.3}_{-1.2}$	$6.72^{+0.05}_{-0.05}$
184	17.00	$26.8^{+1.0}_{-0.9}$	$5.94^{+0.06}_{-0.06}$	$2.5^{+0.5}_{-0.5}$	$22.7^{+3.7}_{-2.9}$	$6.05^{+0.11}_{-0.12}$
185	17.00	$19.1^{+0.8}_{-0.8}$	$6.53^{+0.07}_{-0.06}$	$2.2^{+0.5}_{-0.5}$	$18.2^{+2.7}_{-2.3}$	$6.58^{+0.15}_{-0.14}$
188	17.00	$19.3^{+0.5}_{-0.5}$	$7.00^{+0.03}_{-0.03}$	$1.6^{+0.2}_{-0.2}$	$21.9^{+1.6}_{-1.4}$	$6.88^{+0.07}_{-0.07}$
189	17.00	$20.8^{+0.6}_{-0.6}$	$6.50^{+0.04}_{-0.04}$	$1.8^{+0.2}_{-0.2}$	$22.6^{+2.0}_{-1.8}$	$6.43^{+0.08}_{-0.08}$
190	17.00	$21.2^{+0.3}_{-0.3}$	$8.02^{+0.02}_{-0.02}$	$2.2^{+0.1}_{-0.1}$	$20.1^{+0.9}_{-0.8}$	$8.08^{+0.04}_{-0.04}$
191	17.00	$21.4^{+1.4}_{-1.5}$	$5.88^{+0.10}_{-0.10}$	$1.3^{+0.7}_{-0.6}$	$26.4^{+8.2}_{-5.3}$	$5.71^{+0.19}_{-0.21}$
192	17.00	$20.8^{+0.7}_{-0.6}$	$5.80^{+0.06}_{-0.06}$	$2.4^{+0.5}_{-0.5}$	$18.8^{+2.5}_{-2.1}$	$5.88^{+0.11}_{-0.11}$
193	17.00	$20.3^{+0.5}_{-0.5}$	$6.71^{+0.04}_{-0.04}$	$1.4^{+0.2}_{-0.2}$	$24.4^{+2.3}_{-2.0}$	$6.54^{+0.08}_{-0.08}$
194	17.00	-	-	$1.4^{+0.1}_{-0.1}$	$21.3^{+0.9}_{-0.8}$	$7.88^{+0.04}_{-0.04}$
196	17.00	$21.5^{+0.6}_{-0.6}$	$7.00^{+0.04}_{-0.04}$	$1.4^{+0.3}_{-0.2}$	$26.0^{+2.8}_{-2.3}$	$6.84^{+0.08}_{-0.08}$
197	17.00	$20.7^{+0.4}_{-0.4}$	$6.84^{+0.03}_{-0.03}$	$1.7^{+0.2}_{-0.2}$	$22.6^{+1.3}_{-1.2}$	$6.76^{+0.05}_{-0.05}$
198	16.77	$16.1^{+0.7}_{-0.7}$	$6.91^{+0.07}_{-0.07}$	$1.6^{+0.4}_{-0.3}$	$18.4^{+2.9}_{-2.7}$	$6.75^{+0.19}_{-0.16}$
199	17.00	$20.8^{+1.6}_{-1.5}$	$6.25^{+0.11}_{-0.12}$	$1.7^{+0.7}_{-0.6}$	$22.8^{+7.6}_{-5.1}$	$6.16^{+0.27}_{-0.26}$
200	17.00	-	-	$2.2^{+0.1}_{-0.1}$	$22.3^{+0.7}_{-0.6}$	$7.07^{+0.03}_{-0.03}$
201	17.00	$22.1^{+0.2}_{-0.2}$	$7.88^{+0.01}_{-0.01}$	$2.0^{+0.1}_{-0.1}$	$22.5^{+0.6}_{-0.6}$	$7.86^{+0.02}_{-0.02}$
203	17.00	-	-	$1.5^{+0.1}_{-0.1}$	$28.0^{+1.3}_{-1.2}$	$6.87^{+0.04}_{-0.04}$
204	17.00	$19.7^{+0.3}_{-0.3}$	$7.91^{+0.03}_{-0.03}$	$2.1^{+0.2}_{-0.2}$	$19.2^{+1.1}_{-1.0}$	$7.93^{+0.06}_{-0.06}$
205	17.00	-	-	$1.5^{+0.1}_{-0.1}$	$27.3^{+1.3}_{-1.2}$	$7.50^{+0.04}_{-0.04}$
206	17.00	$22.4^{+0.9}_{-0.9}$	$6.39^{+0.06}_{-0.05}$	$1.8^{+0.3}_{-0.3}$	$23.7^{+3.2}_{-2.6}$	$6.35^{+0.11}_{-0.11}$
207	17.00	$21.0^{+0.3}_{-0.3}$	$6.88^{+0.02}_{-0.02}$	$2.0^{+0.2}_{-0.2}$	$20.8^{+1.1}_{-1.0}$	$6.89^{+0.05}_{-0.05}$
208	17.00	$19.2^{+0.9}_{-0.9}$	$7.59^{+0.07}_{-0.06}$	$2.0^{+0.5}_{-0.4}$	$19.0^{+3.4}_{-2.8}$	$7.61^{+0.19}_{-0.18}$
212	20.14	-	-	$1.1^{+0.3}_{-0.3}$	$28.7^{+4.1}_{-3.3}$	$6.37^{+0.10}_{-0.10}$
213	17.61	-	-	$1.6^{+0.1}_{-0.1}$	$20.9^{+0.8}_{-0.8}$	$8.17^{+0.04}_{-0.04}$
217	17.00	$21.5^{+0.4}_{-0.4}$	$7.59^{+0.03}_{-0.03}$	$2.3^{+0.2}_{-0.2}$	$19.9^{+1.2}_{-1.1}$	$7.66^{+0.06}_{-0.06}$
220	17.00	$20.7^{+0.6}_{-0.6}$	$7.64^{+0.05}_{-0.05}$	$2.3^{+0.4}_{-0.3}$	$19.0^{+2.0}_{-1.7}$	$7.72^{+0.10}_{-0.10}$
221	17.00	$20.8^{+0.3}_{-0.3}$	$6.89^{+0.02}_{-0.02}$	$2.1^{+0.1}_{-0.1}$	$20.2^{+0.8}_{-0.8}$	$6.92^{+0.04}_{-0.04}$

Continued on the next page...

Table 3 – Continued.

HRS	D	β=2		β	β=free	
		T	log(M$_{dust}$)		T	log(M$_{dust}$)
	Mpc	K	M$_\odot$		K	M$_\odot$
222	17.00	$21.0^{+1.3}_{-1.3}$	$6.01^{+0.10}_{-0.09}$	$2.5^{+0.8}_{-0.7}$	$18.3^{+4.2}_{-3.2}$	$6.14^{+0.21}_{-0.20}$
223	17.00	$16.8^{+1.2}_{-1.2}$	$6.32^{+0.12}_{-0.11}$	$1.2^{+0.7}_{-0.6}$	$21.2^{+6.3}_{-4.4}$	$6.07^{+0.26}_{-0.25}$
224	17.00	$19.2^{+0.9}_{-0.9}$	$6.72^{+0.07}_{-0.07}$	$2.0^{+0.5}_{-0.5}$	$19.5^{+3.4}_{-2.8}$	$6.71^{+0.17}_{-0.16}$
226	17.00	$20.5^{+0.5}_{-0.6}$	$6.45^{+0.04}_{-0.04}$	$1.7^{+0.2}_{-0.2}$	$22.2^{+1.9}_{-1.7}$	$6.38^{+0.08}_{-0.08}$
227	15.27	-	-	$0.7^{+0.2}_{-0.2}$	$29.9^{+3.8}_{-3.1}$	$6.62^{+0.09}_{-0.10}$
230	17.00	$21.2^{+0.5}_{-0.5}$	$6.64^{+0.04}_{-0.04}$	$1.7^{+0.2}_{-0.2}$	$23.1^{+1.9}_{-1.7}$	$6.56^{+0.07}_{-0.07}$
231	17.00	$26.1^{+0.8}_{-0.8}$	$5.61^{+0.04}_{-0.04}$	$2.2^{+0.4}_{-0.4}$	$24.8^{+3.5}_{-2.9}$	$5.65^{+0.09}_{-0.09}$
232	17.00	$22.4^{+0.6}_{-0.6}$	$6.38^{+0.04}_{-0.04}$	$2.2^{+0.4}_{-0.3}$	$20.9^{+2.3}_{-2.0}$	$6.44^{+0.09}_{-0.10}$
233	17.00	$22.0^{+0.5}_{-0.5}$	$6.94^{+0.03}_{-0.03}$	$2.2^{+0.2}_{-0.2}$	$20.8^{+1.5}_{-1.3}$	$6.99^{+0.07}_{-0.07}$
237	17.00	$21.9^{+0.6}_{-0.6}$	$6.77^{+0.04}_{-0.04}$	$2.0^{+0.3}_{-0.3}$	$21.6^{+2.0}_{-1.8}$	$6.78^{+0.08}_{-0.08}$
238	15.94	$21.4^{+1.7}_{-1.8}$	$5.81^{+0.12}_{-0.12}$	$0.7^{+0.7}_{-0.7}$	$36.1^{+26.7}_{-10.3}$	$5.40^{+0.27}_{-0.37}$
239	17.00	$22.7^{+0.3}_{-0.3}$	$7.01^{+0.02}_{-0.02}$	$2.1^{+0.1}_{-0.1}$	$22.2^{+0.8}_{-0.8}$	$7.03^{+0.04}_{-0.04}$
242	17.00	$21.2^{+0.6}_{-0.6}$	$6.90^{+0.04}_{-0.04}$	$1.4^{+0.3}_{-0.3}$	$25.6^{+3.0}_{-2.5}$	$6.74^{+0.09}_{-0.09}$
243	17.00	$16.4^{+1.0}_{-0.9}$	$7.13^{+0.09}_{-0.08}$	$2.7^{+0.8}_{-0.6}$	$13.5^{+2.9}_{-2.6}$	$7.38^{+0.34}_{-0.26}$
244	17.00	-	-	$2.2^{+0.1}_{-0.1}$	$20.6^{+0.7}_{-0.7}$	$7.34^{+0.04}_{-0.04}$
246	17.00	$21.0^{+0.4}_{-0.4}$	$7.39^{+0.03}_{-0.03}$	$1.8^{+0.2}_{-0.2}$	$22.6^{+1.4}_{-1.3}$	$7.32^{+0.06}_{-0.06}$
247	17.00	-	-	$1.8^{+0.1}_{-0.1}$	$22.6^{+0.8}_{-0.8}$	$7.66^{+0.03}_{-0.03}$
252	23.13	$18.0^{+1.4}_{-1.4}$	$6.87^{+0.11}_{-0.10}$	$1.0^{+0.4}_{-0.3}$	$27.6^{+5.9}_{-4.5}$	$6.47^{+0.16}_{-0.16}$
254	17.00	$20.3^{+1.0}_{-1.0}$	$7.37^{+0.07}_{-0.07}$	$2.1^{+0.4}_{-0.4}$	$19.6^{+3.0}_{-2.5}$	$7.41^{+0.15}_{-0.14}$
255	17.00	$17.1^{+1.3}_{-1.2}$	$6.99^{+0.11}_{-0.11}$	$0.6^{+0.6}_{-0.5}$	$32.7^{+18.6}_{-9.2}$	$6.36^{+0.30}_{-0.33}$
257	17.00	$16.9^{+0.8}_{-0.8}$	$7.25^{+0.08}_{-0.08}$	$1.8^{+0.5}_{-0.5}$	$18.2^{+3.2}_{-2.7}$	$7.17^{+0.20}_{-0.18}$
258	17.73	$31.2^{+1.1}_{-1.1}$	$5.35^{+0.04}_{-0.04}$	$2.1^{+0.3}_{-0.3}$	$29.6^{+4.3}_{-3.4}$	$5.38^{+0.08}_{-0.09}$
259	17.00	-	-	$1.0^{+0.3}_{-0.3}$	$29.7^{+6.0}_{-4.5}$	$6.66^{+0.14}_{-0.14}$
260	17.00	$23.0^{+0.3}_{-0.3}$	$7.03^{+0.02}_{-0.02}$	$2.0^{+0.1}_{-0.1}$	$23.3^{+1.0}_{-0.9}$	$7.02^{+0.04}_{-0.04}$
261	16.54	$17.3^{+0.7}_{-0.7}$	$6.83^{+0.07}_{-0.06}$	$1.9^{+0.4}_{-0.4}$	$18.0^{+2.3}_{-2.0}$	$6.79^{+0.14}_{-0.13}$
262	17.00	$21.8^{+0.6}_{-0.6}$	$7.07^{+0.04}_{-0.04}$	$1.6^{+0.2}_{-0.2}$	$24.8^{+2.2}_{-1.9}$	$6.97^{+0.07}_{-0.07}$
263	17.27	$18.2^{+0.7}_{-0.7}$	$8.02^{+0.07}_{-0.07}$	$1.7^{+0.4}_{-0.4}$	$19.9^{+2.7}_{-2.3}$	$7.94^{+0.13}_{-0.13}$
264	18.17	$16.7^{+0.6}_{-0.6}$	$6.55^{+0.06}_{-0.06}$	$1.6^{+0.4}_{-0.3}$	$19.1^{+2.5}_{-2.1}$	$6.41^{+0.13}_{-0.13}$
265	21.49	$23.2^{+0.7}_{-0.7}$	$6.38^{+0.04}_{-0.04}$	$1.9^{+0.3}_{-0.3}$	$23.7^{+2.5}_{-2.1}$	$6.36^{+0.08}_{-0.08}$
266	21.30	$17.5^{+1.2}_{-1.2}$	$7.66^{+0.09}_{-0.09}$	$1.1^{+0.4}_{-0.4}$	$25.0^{+5.4}_{-4.1}$	$7.29^{+0.18}_{-0.18}$
267	16.84	$18.7^{+0.9}_{-0.9}$	$6.99^{+0.06}_{-0.06}$	$1.5^{+0.3}_{-0.3}$	$23.1^{+3.2}_{-2.8}$	$6.77^{+0.13}_{-0.12}$
268	17.00	-	-	$1.8^{+0.1}_{-0.1}$	$24.6^{+0.9}_{-0.8}$	$6.93^{+0.03}_{-0.03}$
270	17.70	$21.2^{+0.9}_{-0.9}$	$7.11^{+0.06}_{-0.06}$	$2.1^{+0.4}_{-0.4}$	$20.4^{+2.9}_{-2.4}$	$7.14^{+0.14}_{-0.14}$
271	17.00	-	-	$1.3^{+0.2}_{-0.2}$	$24.3^{+2.6}_{-2.2}$	$6.66^{+0.09}_{-0.09}$
273	17.00	$18.9^{+0.6}_{-0.6}$	$7.11^{+0.05}_{-0.05}$	$1.8^{+0.3}_{-0.3}$	$20.0^{+2.0}_{-1.8}$	$7.05^{+0.10}_{-0.09}$
274	17.00	$17.3^{+0.4}_{-0.4}$	$6.90^{+0.04}_{-0.04}$	$2.1^{+0.3}_{-0.3}$	$17.0^{+1.3}_{-1.2}$	$6.92^{+0.09}_{-0.09}$
275	22.37	-	-	$1.5^{+0.2}_{-0.2}$	$27.1^{+2.0}_{-1.7}$	$7.02^{+0.06}_{-0.06}$
276	17.00	$21.5^{+0.6}_{-0.6}$	$6.69^{+0.04}_{-0.04}$	$1.6^{+0.2}_{-0.2}$	$24.7^{+2.3}_{-2.0}$	$6.57^{+0.08}_{-0.08}$
277	17.00	$22.0^{+1.4}_{-1.3}$	$5.64^{+0.11}_{-0.11}$	$2.9^{+1.4}_{-1.1}$	$17.6^{+5.6}_{-3.9}$	$5.83^{+0.25}_{-0.25}$
279	17.00	$16.8^{+0.8}_{-0.8}$	$7.08^{+0.07}_{-0.07}$	$1.2^{+0.4}_{-0.3}$	$22.1^{+3.5}_{-2.9}$	$6.79^{+0.15}_{-0.14}$
280	17.00	$22.3^{+0.4}_{-0.4}$	$6.51^{+0.02}_{-0.02}$	$1.9^{+0.2}_{-0.2}$	$23.2^{+1.3}_{-1.2}$	$6.48^{+0.05}_{-0.05}$
281	17.00	$20.0^{+0.8}_{-0.8}$	$5.95^{+0.06}_{-0.06}$	$2.2^{+0.5}_{-0.4}$	$19.0^{+2.7}_{-2.3}$	$6.00^{+0.14}_{-0.13}$
285	17.00	$22.5^{+0.3}_{-0.3}$	$7.31^{+0.02}_{-0.02}$	$2.0^{+0.1}_{-0.1}$	$22.4^{+0.9}_{-0.9}$	$7.32^{+0.04}_{-0.04}$
286	17.00	$16.7^{+1.3}_{-1.2}$	$6.75^{+0.15}_{-0.16}$	$0.8^{+0.8}_{-0.7}$	$23.9^{+9.2}_{-5.6}$	$6.41^{+0.27}_{-0.28}$
287	17.00	$21.2^{+0.5}_{-0.5}$	$6.95^{+0.03}_{-0.03}$	$1.7^{+0.2}_{-0.2}$	$23.3^{+1.6}_{-1.5}$	$6.86^{+0.06}_{-0.06}$
288	15.91	$19.2^{+0.5}_{-0.5}$	$7.11^{+0.04}_{-0.04}$	$2.0^{+0.2}_{-0.2}$	$19.1^{+1.6}_{-1.4}$	$7.11^{+0.09}_{-0.09}$
289	23.97	$21.7^{+0.4}_{-0.4}$	$7.45^{+0.02}_{-0.02}$	$1.8^{+0.1}_{-0.1}$	$22.8^{+1.1}_{-1.0}$	$7.41^{+0.04}_{-0.04}$
290	16.23	$25.1^{+0.5}_{-0.5}$	$6.25^{+0.03}_{-0.03}$	$2.1^{+0.3}_{-0.2}$	$24.5^{+2.1}_{-1.8}$	$6.27^{+0.06}_{-0.06}$
292	17.50	$24.4^{+0.4}_{-0.4}$	$6.87^{+0.02}_{-0.02}$	$2.1^{+0.1}_{-0.1}$	$23.8^{+1.1}_{-1.1}$	$6.89^{+0.04}_{-0.04}$
293	15.60	-	-	$1.6^{+0.1}_{-0.1}$	$24.3^{+1.4}_{-1.3}$	$6.73^{+0.05}_{-0.05}$
294	22.97	$20.1^{+0.5}_{-0.5}$	$6.94^{+0.03}_{-0.03}$	$1.5^{+0.2}_{-0.2}$	$23.7^{+1.7}_{-1.5}$	$6.80^{+0.06}_{-0.06}$
295	16.46	$21.8^{+0.5}_{-0.5}$	$7.80^{+0.03}_{-0.03}$	$2.0^{+0.2}_{-0.2}$	$21.9^{+1.3}_{-1.2}$	$7.80^{+0.06}_{-0.06}$
296	15.20	$22.6^{+1.8}_{-1.7}$	$5.76^{+0.11}_{-0.11}$	$0.9^{+0.5}_{-0.5}$	$38.0^{+20.3}_{-10.0}$	$5.38^{+0.23}_{-0.28}$
297	21.54	-	-	$1.6^{+0.1}_{-0.1}$	$22.4^{+1.3}_{-1.2}$	$7.36^{+0.05}_{-0.05}$
298	20.27	$24.4^{+0.4}_{-0.4}$	$6.68^{+0.02}_{-0.02}$	$2.1^{+0.2}_{-0.1}$	$23.3^{+1.3}_{-1.2}$	$6.72^{+0.05}_{-0.05}$
299	16.73	$18.4^{+0.9}_{-0.9}$	$7.16^{+0.07}_{-0.07}$	$1.4^{+0.4}_{-0.3}$	$22.7^{+3.3}_{-2.7}$	$6.97^{+0.12}_{-0.12}$
300	19.34	$19.5^{+0.8}_{-0.8}$	$6.26^{+0.07}_{-0.07}$	$1.6^{+0.5}_{-0.5}$	$21.6^{+4.0}_{-3.0}$	$6.17^{+0.15}_{-0.16}$

Continued on the next page...

Table 3 – Continued.

HRS	D	β=2		β=free		
		T	log(M$_{dust}$)	β	T	log(M$_{dust}$)
	Mpc	K	M$_\odot$		K	M$_\odot$
301	19.71	$17.4^{+0.9}_{-1.0}$	$7.43^{+0.08}_{-0.07}$	$1.1^{+0.4}_{-0.3}$	$24.1^{+4.1}_{-3.2}$	$7.10^{+0.15}_{-0.15}$
302	20.61	$15.6^{+1.1}_{-1.0}$	$7.07^{+0.09}_{-0.09}$	$1.0^{+0.4}_{-0.3}$	$25.0^{+5.5}_{-4.4}$	$6.57^{+0.19}_{-0.17}$
303	24.53	$26.8^{+0.6}_{-0.6}$	$6.49^{+0.03}_{-0.03}$	$2.1^{+0.3}_{-0.2}$	$26.3^{+2.5}_{-2.1}$	$6.51^{+0.07}_{-0.07}$
304	19.57	$19.1^{+0.4}_{-0.4}$	$7.10^{+0.03}_{-0.03}$	$2.0^{+0.2}_{-0.2}$	$19.2^{+1.2}_{-1.2}$	$7.09^{+0.07}_{-0.07}$
305	16.73	$18.2^{+1.3}_{-1.3}$	$5.98^{+0.13}_{-0.13}$	$2.2^{+1.0}_{-0.8}$	$17.5^{+5.0}_{-3.7}$	$6.03^{+0.29}_{-0.27}$
306	16.23	$23.2^{+1.5}_{-1.5}$	$6.61^{+0.08}_{-0.08}$	$2.6^{+0.7}_{-0.6}$	$19.4^{+4.0}_{-3.1}$	$6.77^{+0.19}_{-0.18}$
307	17.74	$19.1^{+0.7}_{-0.7}$	$7.71^{+0.05}_{-0.05}$	$1.6^{+0.3}_{-0.3}$	$21.5^{+2.2}_{-2.0}$	$7.60^{+0.10}_{-0.09}$
309	19.76	-	-	$1.0^{+0.2}_{-0.2}$	$28.4^{+3.4}_{-2.8}$	$6.11^{+0.09}_{-0.09}$
310	24.54	$21.3^{+0.5}_{-0.5}$	$7.07^{+0.04}_{-0.04}$	$2.3^{+0.3}_{-0.3}$	$19.9^{+1.6}_{-1.5}$	$7.13^{+0.07}_{-0.07}$
311	21.31	$19.1^{+0.7}_{-0.7}$	$7.50^{+0.05}_{-0.05}$	$2.0^{+0.3}_{-0.3}$	$19.4^{+2.2}_{-2.0}$	$7.49^{+0.12}_{-0.11}$
313	21.29	$16.9^{+0.8}_{-0.8}$	$7.27^{+0.06}_{-0.06}$	$1.5^{+0.3}_{-0.3}$	$20.5^{+2.9}_{-2.7}$	$7.06^{+0.15}_{-0.13}$
314	19.84	-	-	$1.0^{+0.2}_{-0.2}$	$27.6^{+3.4}_{-2.8}$	$6.57^{+0.09}_{-0.09}$
315	20.57	$20.7^{+2.7}_{-2.8}$	$6.24^{+0.21}_{-0.19}$	-	-	-
317	24.51	$17.4^{+1.0}_{-0.9}$	$6.42^{+0.10}_{-0.10}$	$1.8^{+0.8}_{-0.7}$	$18.7^{+4.8}_{-3.6}$	$6.34^{+0.26}_{-0.23}$
318	19.57	-	-	$1.4^{+0.2}_{-0.2}$	$25.1^{+1.9}_{-1.7}$	$6.80^{+0.06}_{-0.06}$
319	19.54	-	-	$1.1^{+0.3}_{-0.3}$	$26.3^{+3.4}_{-2.8}$	$6.98^{+0.10}_{-0.11}$
320	22.61	-	-	$1.1^{+0.3}_{-0.3}$	$25.2^{+4.0}_{-3.4}$	$7.27^{+0.14}_{-0.13}$
321	22.59	$23.5^{+0.4}_{-0.4}$	$6.55^{+0.02}_{-0.02}$	$1.9^{+0.2}_{-0.2}$	$24.6^{+1.4}_{-1.3}$	$6.51^{+0.04}_{-0.05}$
322	21.50	$14.4^{+1.4}_{-1.3}$	$7.51^{+0.15}_{-0.15}$	$1.7^{+1.5}_{-0.9}$	$16.0^{+6.6}_{-5.8}$	$7.38^{+0.70}_{-0.39}$
323	23.43	-	-	$1.7^{+0.1}_{-0.1}$	$22.8^{+0.9}_{-0.9}$	$7.11^{+0.04}_{-0.04}$